Gabriela Valencia Guzmán

Eficiencia fotosintética en el complejo FMO: un estudio dinámico utilizando los marcos de Lindblad y funciones de Green fuera del equilibrio.

Photosynthetic Efficiency in FMO Complex: A Dynamical Study Using the Lindblad and Non-equilibrium Green's Functions Frameworks.

DEPARTAMENTO DE FÍSICA

FACULTAD DE CIENCIAS NATURALES Y EXACTAS

UNIVERSIDAD DEL VALLE

Santiago de Cali, 2024

Photosynthetic Efficiency in FMO Complex: A Dynamical Study Using the Lindblad and Non-equilibrium Green's Functions Frameworks.

Gabriela Valencia Guzmán

The thesis as a partial requirement for the qualification for the title of a physicist

Director:
Prof. Dr. Juan David Vasquez Jaramillo
Departamento de Ingeniería Eléctrica
Universidad Tecnológica de Pereira
Pereira

Co-director:
Prof. Dr. Karen Rodríguez Ramírez
Física Teórica del Estado Sólido
Departamento de Física
Universidad del Valle
Cali

Departamento de Física
Facultad de Ciencias Naturales y Exactas
Universidad del Valle
Sede Cali
Física - 3146
Santiago de Cali, 2024

Para mi mami, mi nene
y mi sol.

Gratitude

There are not enough words to thank my mother and brother, because they gave me their love and support throughout my academic process, especially in this last stage that was very challenging for me. This work was done thanks to the fact that they always believed in me. They are everything in my life.

I thank professors Juan David Jaramillo and Karen Rodríguez for their teachings and great patience, which allowed the completion of this work. To my colleagues of Fisteo, for giving me a space to share, learn, and develop new knowledge. And a special mention to Andrés Galindo and Pedro Artunduaga, for helping me implement the codes used in this work.

I would also like to thank the Universidad del Valle, because studying this bachelor has been one of the most wonderful things I have experienced. I am grateful for both the good and the not so good, in the end, each of those experiences has brought me here, and I am very proud that it has been like this.

To my colleagues Ana Maria Enriquez and Nicolle Tello, because they always gave me a helping hand every time I thought I was going to give up. To my cohort mates and my GRACA colleagues, because this process was much more fun and special with them. Also to all my family and friends, who never stopped encouraging me to continue fighting for my dreams.

Finally, I want to thank my sun, because she was the one who put her soul and her heart into each of these pages.

Abstract

This work aimed to study the efficiency of the photosynthetic complex Fenna-Matthews Olso (FMO). For this purpose, the behavior of the average efficiency in the reduced FMO system (FMO-123) was analyzed employing two formalisms: the Lindblad master equation, and the Green functions. First, the dynamics of the system were found with the Lindblad formalism, which allowed to establish the Dynamical Efficiency of the FMO-123, defined by the ratio between the output and input power, which presented a maximum peak for a value of 50 ps^{-1} of the dephasing rate (γ_{deph}). Second, through the retarded Green's function, the density of states, and the use of Parseval's theorem, an analogous expression for the Dynamical Efficiency was defined in this formalism. It has also a maximum for a value of 1.8 meV of the coupling of FMO with the reservoirs (Γ). From the two results obtained, it stands out how the calculation of the Dynamical Efficiency takes into account the dynamics reflected in the input power at site 1, different from how the efficiency of FMO has been treated in previous studies, providing a more complete understanding of the system behavior. On the other hand, the use of the Lindblad formalism indicated that the high efficiency of this complex is achieved by the environment-assisted quantum transport (ENAQT) regime. This could show that the efficiency can be maximum for a certain value of the dephasing rate, i.e. of the support from the environment, regardless of whether this support leads to the presence of long-lived coherences in the system. As a perspective, we plan to use both formalisms again to study the excitonic current of FMO.

Keywords— Photosynthetic complex, FMO, Efficiency, Lindblad Master Equation, Green's functions, Non-equilibrium Green's functions.

Resumen

Este trabajo tuvo como objetivo estudiar la eficiencia del complejo fotosintético FMO. Para ello, se analizó el comportamiento de la eficiencia media en el sistema reducido FMO-123 por medio de dos formalismos: la ecuación maestra de Lindblad y las funciones de Green. En primer lugar, se halló la dinámica del sistema con el formalismo de Lindblad, lo que permitió establecer la Eficiencia Dinámica del FMO-123, definida por el cociente entre la potencia de salida y entrada, la cual presentó un pico máximo para un valor de 50 ps^{-1} de la tasa de desfasamiento (γ_{deph}). En segundo lugar, a través de la función de Green retardada, la densidad de estados y el uso del teorema de Parseval, se definió una expresión análoga para la Eficiencia Dinámica en este formalismo. Se encontró que esta también presenta un máximo para un valor de 1.8 meV del acoplamiento del FMO con los reservorios (Γ). De los dos resultados obtenidos se destaca cómo el cálculo de la Eficiencia Dinámica toma en cuenta la dinámica reflejada en la potencia de entrada en el sitio 1, diferente a cómo se ha tratado la eficiencia del FMO en estudios anteriores, esto proporciona una comprensión más completa del comportamiento del sistema. Por otra parte, el uso del formalismo de Lindblad indicó que la alta eficiencia de este complejo se logra en el régimen ENAQT. Esto podría revelar que la eficiencia puede ser máxima para un valor específico de la tasa de desfase, es decir, de la asistencia del medio ambiente, independientemente de si esta asistencia conduce a la presencia de coherencias de larga duración en el sistema. Como una perspectiva, se planea emplear ambos formalismos nuevamente para estudiar la corriente excitónica del FMO.

Palabras clave— Complejo fotosintético, FMO, Eficiencia, Equación Maestra de Lindblad, Funciones de Green, Funciones de Green por fuera del equilibrio.

Contents

Chapter 1

Unraveling the photosynthesis efficiency

The most crucial aspect of our world today is energy. Our world relies on energy to function. It powers our vehicles and airplanes, illuminates our nights, constructs our buildings, and essentially allows us to thrive, progress, and exist. However, we are also aware that energy poses a significant problem. With over eight billion people on Earth, the demand for energy in our daily lives is immense. Furthermore, our economic growth hinges on energy consumption. Each day, we consume increasing amounts of energy, predominantly derived from fossil fuels, which harm our environment and ultimately affect us [23]. Even renewable energy sources have their own challenges, particularly related to storage capacity, and they also leave an ecological footprint during their production, disrupting ecosystems [28]. Additionally, they are insufficient to meet the growing demands of humanity. Given these circumstances, it becomes imperative to explore alternative solutions.

This is where the concept of photosynthesis becomes so important. We know that photosynthesis is the process through which plants and other organisms harness energy from sunlight. It is one of the most studied processes in quantum biology due to its vital importance since all life on Earth is sustained by the process of converting light energy into adenosine triphosphate (ATP) [7]. Taking into account the above, it is logical to think that during the thousands of years, this mechanism has been improved, evolution has opted for those features that provided a competitive advantage for it, regardless of whether the underlying process is modeled in a classical or quantum way [12]. Photosynthetic complexes such as Fenna-Matthews Olso (FMO), extracted from green sulfur bacteria, are examples of how certain organisms exposed to extreme conditions take advantage of quantum properties to scale their efficiency to levels high enough to ensure their survival [50].

In recent decades, there has been a remarkable increase in the study of quantum effects in photosynthetic complexes, since a thorough understanding of their operation could allow the development of technologies that could lead to the initiation of a new energy revolution [2, 6, 9, 20, 26, 58]. Just imagine if we could derive our own energy through a process like artificial photosynthesis. Or even, since biological photosynthesis provides a model for converting solar energy into energy-rich molecules such as H_2 and carbohydrates, one of the possible technologies could be Solar Fuel, which has enormous potential for storing high energy density in the form of chemical bonds. If technological advances are achieved to produce these fuels with viable efficiency and affordable cost, it can contribute to the patenting of other sustainable technologies [61].

Therefore, the study of photosynthetic complexes such as FMO has become a priority in scientific work, since we must first comprehend the workings of photosynthesis and its remarkable efficiency [26]. As a result of these investigations, the idea that excitation energy transfer (EET) was a coherent process within photosynthetic complexes [53] began to be discussed more than 70 years ago. However, its presence was not experimentally confirmed until about 10 years ago, when the technique of two-dimensional electron spectroscopy was developed to include frequencies in the visible region. This technique provides evidence for the existence of couplings between energy levels in a molecular system and how these affect the dynamics of the excited state of the system. Subsequently, the discovery of long-term quantum coherence in photosynthetic complexes places them in the category of open quantum systems. The framework and concepts of this theory, originally developed in a different context, have been used in the quantum information community to analyze these complexes from a new perspective [6]. Thus, quantum coherence emerges as a potential clue in this pursuit.

However, previous research suggests that the coherence phenomenon does not increase the quantum efficiency of photosynthesis. In particular, E. Z. Harush and Y. Dubi in Ref.[20] suggest that the answer to the question *Do photosynthetic complexes use quantum coherence to increase their efficiency?* is negative. Nevertheless, in this work, it is proposed that since the studied photosynthetic complexes (the FMO, the cryptophyte protein phycocyanin 645 (PC-645), and the light-harvesting 2 (LH2)) are in an intermediate coupling regime with the reservoir, the Lindblad formalism, at first glance, may not be the tool to tackle this problem since its application is limited to the weak coupling regime. Nevertheless, this formalism is a good tool for non-experts to approach the topic and better understand it in the Markovian limit [11]. Therefore, it is necessary to examine the problem from another perspective in order to provide more adequate observations focused on finding a definitive answer. In this order of ideas, non-equilibrium Green's functions could provide more conclusive results, considering that it is a technique that allows the analysis to be carried out in, what could be considered, an appropriate regime [14].

In conclusion, the study of how the persistence of quantum coherence enhances the efficiency of one of the most significant photosynthetic complexes, the FMO; is essential at a time when it is imperative to develop new energy technologies that offer the possibility of migrating towards highly efficient sustainable alternatives. Hence, the analysis of the efficiency in the quantum regime of the FMO complex first, in the Lindblad formalism, and second, in the non-equilibrium Green's functions (NEGF) could provide different perspectives that allow us to reconsider what is known about photosynthesis and the influence of quantum coherence on the efficiency of this process.

1.1 The Fenna–Matthews–Olson Complex

Photosynthesis begins with the absorption of light by a pigment, usually chlorophyll, resulting in the oxidation of an electron donor, which is then used in some way to produce ATP. While it may be thought that only plants carry out this process, many algae, for example, do it as well. Furthermore, not only eukaryotic organisms can be phototropic, but there are other prokaryotes, five specific groups of bacteria, that also carry out photosynthesis [50]. Among the bacteria mentioned above there are green sulfur bacteria (see figure 1.1), which can be found at great depths in the ocean, fueled by enormous thermal radiation emitted by hot springs on the seafloor. For this reason, they have adapted to survive in extremely low light intensities by developing antenna structures

known as chlorosomes, which allow for surprisingly effective absorption of radiation.

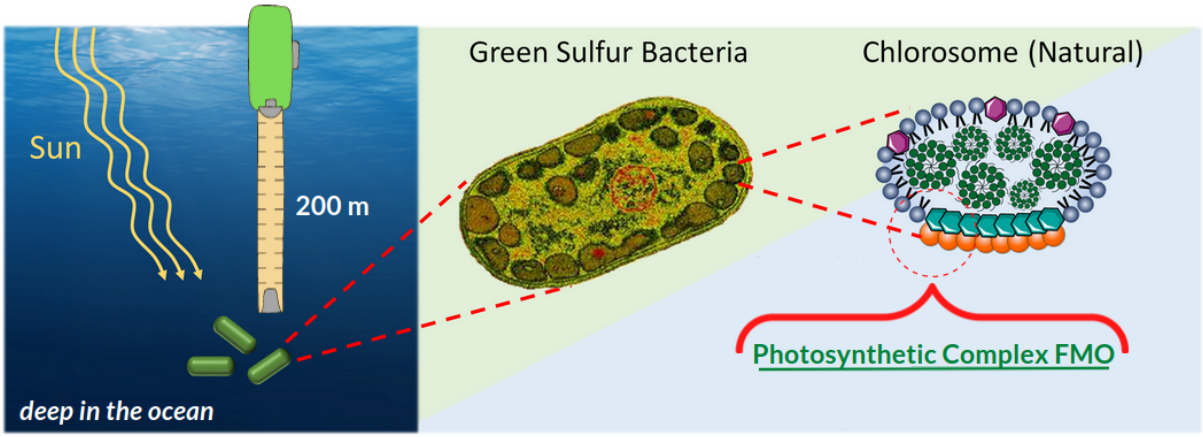

Figure 1.1: The green sulfur bacteria in their natural environment at 200 m depth in the ocean. In this case, obtaining photons from sunlight is complicated, forcing the bacteria to be extremely efficient. Inside the bacteria are chlorosomes that capture light and connect to the reaction center through the FMO complex [37].

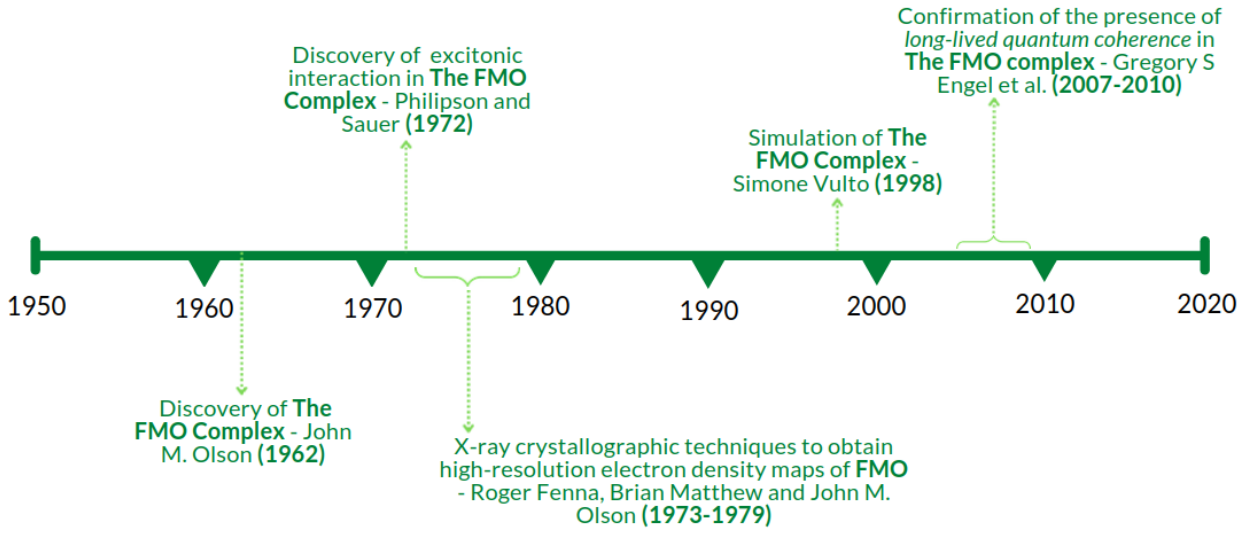

Figure 1.2: Chronology of the FMO complex, scanned from 1950 up today following the most highlighted events [17, 41].

In addition, chlorosomes are connected to a mechanism responsible for carrying out the chemical processes involved in photosynthesis (reaction center) through structures known as photosynthetic complexes, which are responsible for transporting the excitations to their destination; in the case of green sulfur bacteria, the complex is named Fenna-Matthews Olson. Due to its very special conditions, the FMO complex has managed to exhibit a high efficiency with which it has allowed these bacteria to survive in their natural habitat; for this reason, it constitutes an excellent starting point for the study of quantum effects, since this is where the advantages of quantum nature are expected to begin to be exploited [50].

The FMO was discovered by John M. Olson in 1962, followed by Philipson and Sauer in 1972, who uncovered the excitonic interaction within it, the FMO chronology is presented schematically in figure 1.2 [41]. Between 1973 and 1979, Roger Fenna, Brian Matthew, and John M. Olson utilized a new X-ray technique to generate electron density maps of the FMO, revealing its structure and giving rise to the name FMO itself [15]. In 1998, Simone Vulto created an outstanding simulation of the FMO [58]. Finally, from 2007 to 2012, the presence of long-lived quantum coherence in the FMO was definitively confirmed [52]. This raises the question of whether there is a correlation between the high efficiency of green sulfur bacteria, particularly in the FMO, and their quantum coherence.

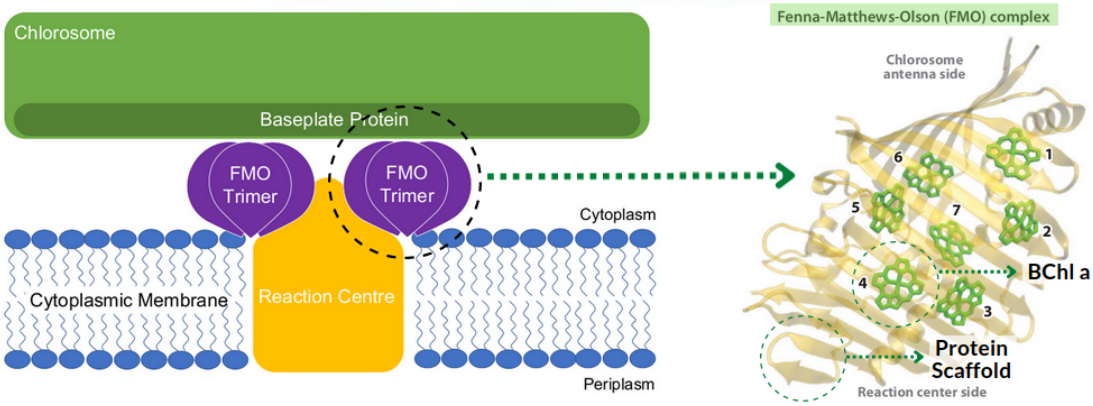

Figure 1.3: Structure inside the green sulfur bacteria and the FMO monomer. The FMO complex is observed within the structure of the green sulfur bacteria, and the presence of seven chromophores embedded in the protein scaffold [1, 26].

Looking at the structures that allow photosynthesis to take place in these organisms, a simple model for a large number of them consists of a configuration of three main parts: the antenna (chlorosome), the transfer network, and the reaction center. The chlorosome captures energy from sunlight and then excites the pigment electrons, combining afterward with holes to form excitons. The photons travel from the antenna to the intermediate protein exciton transfer complex (ETC), also known as the photosynthetic complex, through the baseplate protein [1]. In addition, the latter is connected to the reaction center, which is a pigment-protein complex (PPC) that contains a pair of special dimeric pigments that act as donors after electronic excitation; this triggers an electron transfer cascade that is coupled to the transfer of protons across a membrane, creating a proton gradient that is then used to drive ATP synthesis [11].

In previous research, the FMO complex is usually preferred because it is the simplest transfer network known and, most importantly, it is relatively easy to isolate and crystallize, then its structure has been known for a long time. Moreover, it was the first chlorophyll-containing protein whose structure was fully determined by x-ray crystallography [15]. It is worth mentioning that, the FMO has a trimeric structure, meaning it consists of three interconnected monomers that link to the reaction center. Each of its three subunits consists of a protein scaffold in which seven interconnected Bacteriochlorophyll a (BChl-a) molecules are attached, which are known as chromophores [50]. Besides, the FMO complex is enclosed by a protein scaffold, and the interaction between molecules and the surrounding protein scaffold significantly influences the transport process. Experimental evidence shows that energy transport through this complex is indeed highly efficient.

Recent studies of these systems have found traces of quantum energy transport, similar to a wave, in the FMO complex. Although the first of these experiments was performed at temperatures around 77 K, subsequent studies yielded similar results at temperatures of 277 K, which is about room temperature. At present, a further increase of this temperature is not possible due to experimental limitations in working with the FMO structures [50]. On the other hand, the excitation energies of the pigments, as well as the strength of the interactions between them, have been determined experimentally and theoretically [2]. The study of the FMO complex extends across various scientific disciplines, some directly linked to its investigation and others seemingly unrelated. However, it is evident that a comprehensive understanding of the FMO complex needs interdisciplinary collaboration as can be seen in Figure 1.4 where bast chemistry, biology, and physics fields interact for the same purpose.

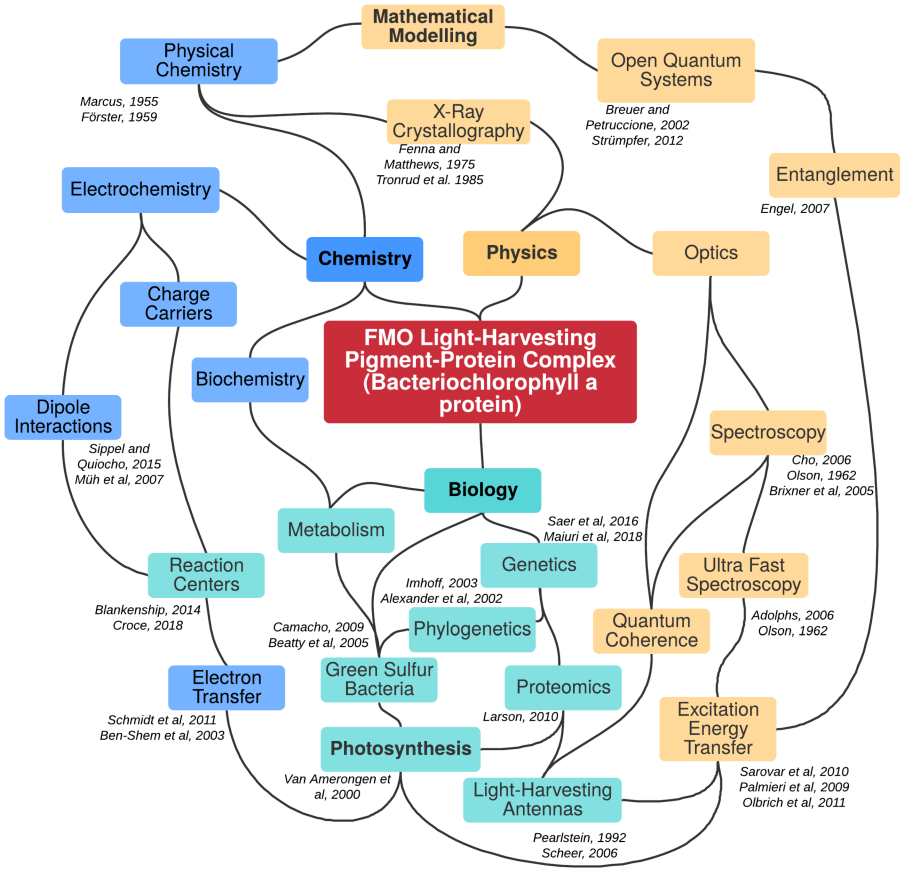

Figure 1.4: Schematic map of the multidisciplinary study surrounding the FMO research [17].

1.2 Dynamics in FMO Complex

1.2.1 Dynamics of Open Quantum Systems

In many realistic situations, the effects of an environment in contact with the quantum system under study must be taken into account to accurately model its dynamics, i.e. the quantum system must be modeled as an open quantum system. The evolution of an open quantum system is described by a total Hamiltonian of the form

$$\hat{H}_{tot} = \hat{H}_S \otimes \hat{1}_E + \hat{1}_S \otimes \hat{H}_E + \hat{H}_I, \tag{1.1}$$

where $\hat{H}_S$ is the system hamiltonian, $\hat{H}_E$ is the environment hamiltonian, and $\hat{H}_I$ describes the interaction between the system and the environment. It is important to note that in a multipartite quantum system, the environment can act globally as a common reservoir or locally in each subsystem [6].

1.2.2 Excitonic Transport in FMO Complex

When a pigment molecule interacts with light, the energy of the photon creates a quasiparticle. This is a combined state of an excited electron and a hole, called an exciton. The electron in the excited state and the hole in the ground state are bound together by the Coulomb force [35]. As mentioned above, in photosynthetic complexes, photons are absorbed by antenna molecules and then transmitted through a pigment lattice until the excitation reaches a reaction center where the photon energy is converted to chemical energy. In this kind of aggregate pigment-protein, where site interaction is weak, excitons localize to only one pigment at a time and move through the system in a hopping manner, resulting in incoherent EET. Thus, the overall efficiency of photosynthetic complexes depends, among many other things, on the efficiency with which an excitation can be transferred from the antenna molecules to the reaction center [6].

Pigments are organic molecules that absorb light in the visible spectrum, chlorophyll is the prevalent pigment type. Photoexcitation from the ground state to the excited state occurs within attoseconds. Configuration of the nuclei in the pigment molecule remains unchanged during photoexcitation, hence the molecule enters a non-equilibrium state after excitation. Due to environmental interaction, the pigment molecule relaxes to its vibrational ground state by converting to heat in the excited state. This process occurs over time scales of 100 femtoseconds to a few picoseconds, and the consequent released energy (energy reorganization) can cause a reconfiguration of the environment. On timescales ranging between picoseconds to nanoseconds, the pigment molecule relaxes to its electronic ground state either via fluorescence or non-radiative processes [6].

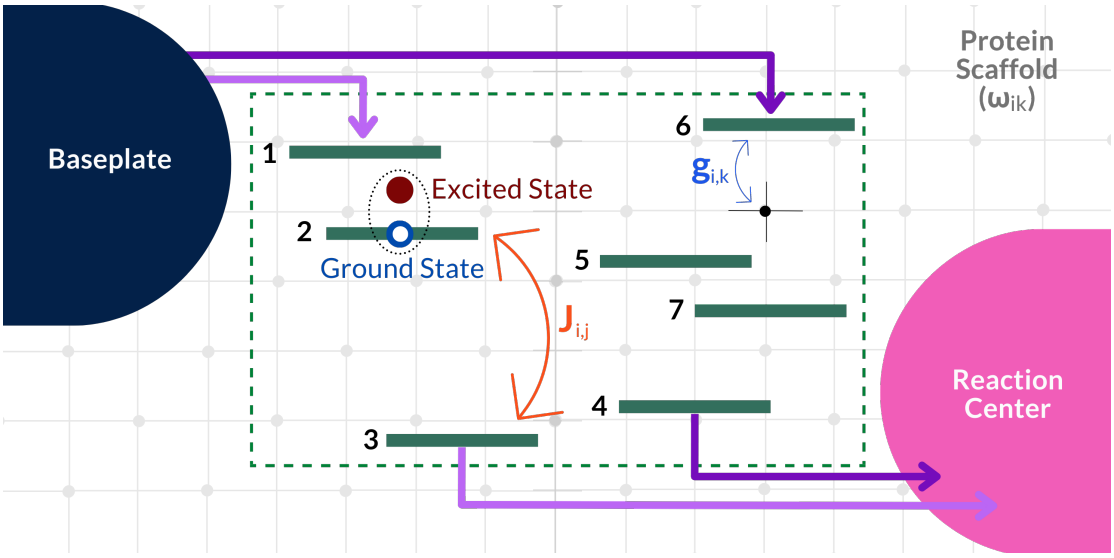

Figure 1.5: Structure of the FMO complex system. The baseplate, the reaction center, and the seven levels (chromophores) are shown in their energy distribution. The couplings between the elements of the system and the exciton within it are also schematized.

Furthermore, there exists a specific arrangement of the molecules within the FMO complex to facilitate efficient transport. Specifically, sites 1 and 6 are positioned at the top and are connected to the baseplate protein, while sites 2, 5, and 7 reside in the middle. Finally, sites 3 and 4 are located at the bottom and are connected to the reaction center. This is in concordance with experimental studies of lattice orientation using mass spectrometry [19]. This FMO distribution can be seen in figure 1.5.

In this order of ideas, the modeling of EET in photosynthetic complexes is usually done by defining the Frenkel exciton hamiltonian, which can be seen as a model for a two-level system. This is due to the very fast internal conversion of higher singlet states, which means that pigment molecules can be modeled as systems with a singlet ground state, S_0, and an excited state which happens to be singlet, S_1. Furthermore, a two-state system that describes a pair of donor-acceptor pigments in EET differs from a two-level system that corresponds to the electronic ground and excited states, this is because the donor and acceptor in a two-state system are coupled to individual phonon modes, whereas the electronic ground and excited states in a two-level system are coupled to the same phonon modes (see figure 1.6) [26]. If the ground state is denoted by $|\psi_g\rangle$ and the excited state by $|\psi_e\rangle$, the transition between them is characterized by the dipole moment, $\vec{\mu} = \langle\psi_g\,|q_e\vec{r}\,|\psi_e\rangle$, where q_e is the charge of the electron and $\vec{r}$ is its position [6, 63]. Then the model can be written as,

$$\hat{H}_{\mathrm{S}} = \sum_{i=1}^{n} \varepsilon_i |i\rangle\langle i| + \sum_{\substack{i\neq j \\ i,j=1}}^{n} J_{ij} |i\rangle\langle j|, \tag{1.2}$$

where the i-th state $|i\rangle = |\psi_{g,1}\rangle \ldots |\psi_{e,i}\rangle \ldots |\psi_{g,7}\rangle$ is the tensor product of the states of each of the seven levels, of which only one can be in the excited state $|\psi_e\rangle$, the rest must be in the ground state $|\psi_g\rangle$ [6].

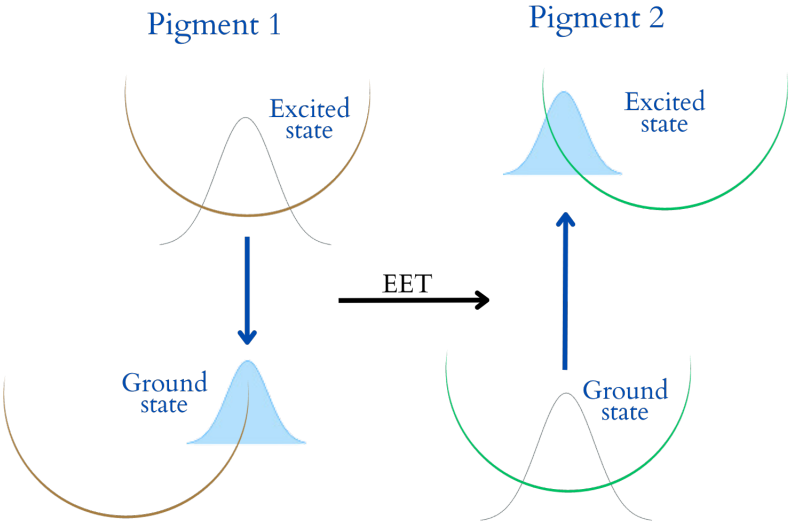

Figure 1.6: Schematic of EET mechanism from pigment 1 to pigment 2 through a two-level system that corresponds to the electronic ground and excited states [26].

Besides, ε_i is the energy associated with the i-th exciton, and J_{ij} is the coupling term between the i-th and j-th excitons, which is generally given by a dipole-dipole interaction of the form

$$J_{ij} = \frac{1}{4\pi\varepsilon_0 r_{ij}^3} \left[\vec{\mu}_i \cdot \vec{\mu}_j - 3\left(\vec{\mu}_i \cdot \hat{r}_{ij}\right)\left(\vec{\mu}_j \cdot \hat{r}_{ij}\right)\right], \tag{1.3}$$

such that, $\vec{r}_{ij} = r_{ij}\hat{r}_{ij}$ is defined as the displacement vector from i-th site to j-th, $\vec{\mu}_i$ is the transition dipole of i-th site, and ε_0 is the vacuum permittivity. For photosynthetic complexes with n chromophores, only exist n single excited states in the energy transfer process. Thus, only $log_2 n$ qubits are needed to perform the quantum simulation [63]. Furthermore, in this approximation the number of electronic excitations is not changed, so the $\hat{H}_{\mathrm{S}}$ commutes with the operator number of excitons in the system [32].

Note that the pigment system is coupled to a protein environment. In these structures, the environment can be described as a set of linearly coupled harmonic oscillator modes. In general, it can be assumed that anharmonic modes are irrelevant in the EET [6]. In pigment-protein molecular aggregates, each pigment is assumed to be influenced by its own local environment, which implies that each contribution can be written as,

$$\hat{H}_{\mathrm{E}} = \sum_{i,k} \hbar\omega_{ik}\hat{a}^{\dagger}_{ik}\hat{a}_{ik} = \sum_{i,k} \hbar\omega_{ik}\frac{(\hat{p}^2_{ik} + \hat{q}^2_{ik})}{2}, \tag{1.4}$$

where $\hat{a}^{\dagger}_{ik}$ and $\hat{a}_{ik}$ are the creation and annihilation operators, respectively, of the k-th phonon mode as an environment of each i-th molecule. On the other hand, q_{ik} is a dimensionless normal coordinate of the equilibrium configuration of pigment i, p_{ik} is the momentum of the atom in position q_{ik}, and ω_{ik} is the frequency of the corresponding normal mode [6]. Finally, it is assumed that the excited state of the i-th pigment is linearly coupled to its own set of harmonic oscillators, hence, the Hamiltonian for the system coupled to the reservoir is given by

$$\hat{H}_{\mathrm{I}} = \sum_{i,k} g_{ik}|i\rangle\langle i|\left(\hat{a}^{\dagger}_{ik} + \hat{a}_{ik}\right) = -\sum_{i,k} \hbar\omega_{ik}d_{ik}|i\rangle\langle i|q_{ik}, \tag{1.5}$$

where g_{ik} is the intensity of the coupling [6, 63]. Besides, the interaction Hamiltonian arises due to differences in the environmental Hamiltonian between the excited electronic state and the ground state,

$$\begin{aligned}\sum_{\xi} \hbar\omega_{i\xi}\frac{\left(p^2_{i\xi} + (q_{i\xi} - d_{i\xi})^2\right)}{2} &= \sum_{\xi} \hbar\omega_{i\xi}\frac{\left(p^2_{i\xi} + q^2_{i\xi} - 2q_{i\xi}d_{i\xi} + d^2_{i\xi}\right)}{2} \\ &= \hat{H}_{\mathrm{E}} + \sum_{\xi} \hbar\omega_{i\xi}\frac{d^2_{i\xi}}{2} - \sum_{\xi} \hbar\omega_{i\xi}d_{i\xi}q_{i\xi},\end{aligned} \tag{1.6}$$

where the last term is exactly the coupling term in equation 1.5 and the middle term is equal to the i-th reorganization energy λ_i [6], also known as The Franck-Condon transition energy [26],

$$\lambda_i = \sum_{\xi} \hbar\omega_{i\xi}\frac{d^2_{i\xi}}{2}. \tag{1.7}$$

After electronic excitation, reorganization occurs from the nuclear configuration to the actual equilibrium configuration in the excited state with reorganization energy dissipating [26].

1.3 Quantum Pathways in FMO Complex

Until now, the physical system under study has been presented as a huge set containing seven chromophores, in addition to adding the ground state as the one where there are no excitons in

the system. Starting from the beginning with this level of complexity can be a very challenging task both theoretically and numerically, it is for this reason that it is of great interest to explore arguments that allow us to consider reductions in this large system without sacrificing the physical reality; a perfect example of this strategy is presented in Ref.[3]. Given the above, the concept of quantum redundancy exhibited by the FMO complex becomes relevant [54]. This means that there is more than one unique way to perform efficient transport.

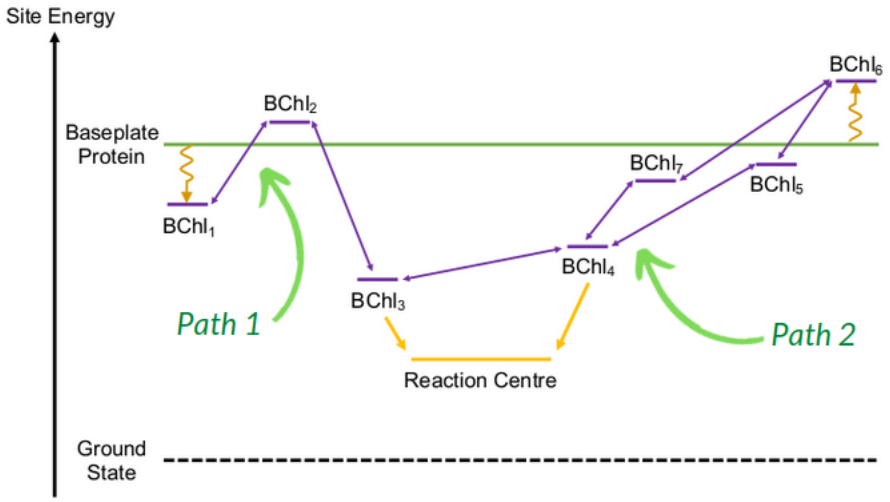

Figure 1.7: Quantum pathways present in the FMO complex [1].

As can be seen in figure 1.7, for the FMO we have two paths: $1 \to 2 \to 3$ and $6 \to (5,7) \to 4 \to 3$, where each number refers to an excitonic level with a very specific energy, as described in subsection 1.2.2 (see figure 1.5), besides, it has been found that the first one presents the strongest quantum coherence [15]. Therefore, there is a possibility that a subset of the original seven levels of the FMO (e.g., *123*) may have an efficiency close to, or even greater than, compared to the original system, in which all seven levels are considered [54].

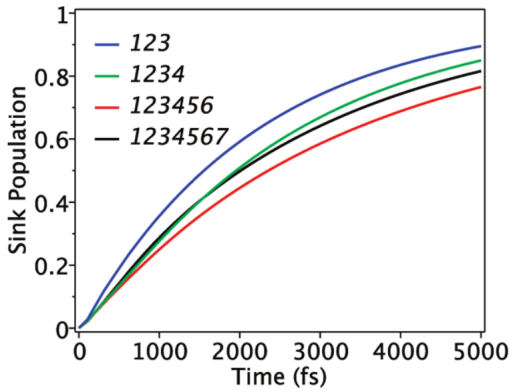

(a) Population in the sink site of the different quantum pathways.

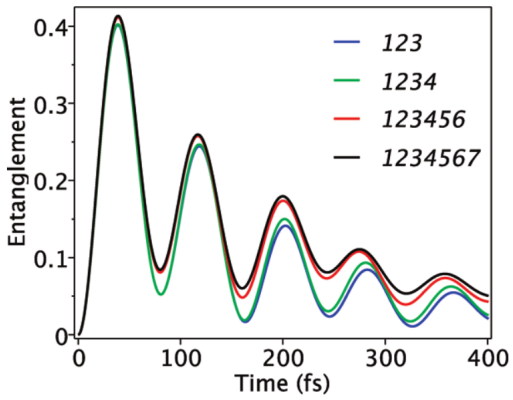

(b) Entanglement of the different quantum pathways.

Figure 1.8: Properties for different quantum pathways present in the FMO complex [54].

Making such considerations, it could be possible to study the dynamics of the FMO system through

a subsystem whose behavior is practically the same as the whole system, with the ease of being much smaller and, consequently, it is easier to apply the selected mathematical tools. The case we choose has been studied by N. Skochdopole and D. A. Mazziotti in Ref.[54], we have decided to consider only the transport that takes place between the first three chromophores of the system, this is called reduced FMO system (FMO-123).

According to this analysis (see figure 1.8a), energy transfer efficiency between different subgroups of the seven chromophores within the FMO complex is switched off and energy transfer occurs within a smaller set of chromophores. The efficiency of energy transfer from site 1 to the sink, i.e. the connection to the reaction center, is compared in figure 1.8a for different subsystems. We can see that the efficiency decreases when considering paths *456* and *123* (reduced system *123456*) since this increases the number of sites into which energy can enter and therefore decreases the population of each site.

The addition of site 7 improves the efficiency because 7 provides a new downward quantum path through 4, which has even less energy than site 5 (see figure 1.7). In fact, we observe that subsystems *123*, *1234*, and *12345* are more efficient than the whole system. In figure 1.8b we also observe the entanglement patterns in different subsystems, including the whole system. Interestingly, the exciton entanglement in the reduced systems shows similar behavior to that of the full system. These entanglement calculations demonstrate that the energy transfer in both the reduced and the complete systems occurs via the same quantum mechanism.

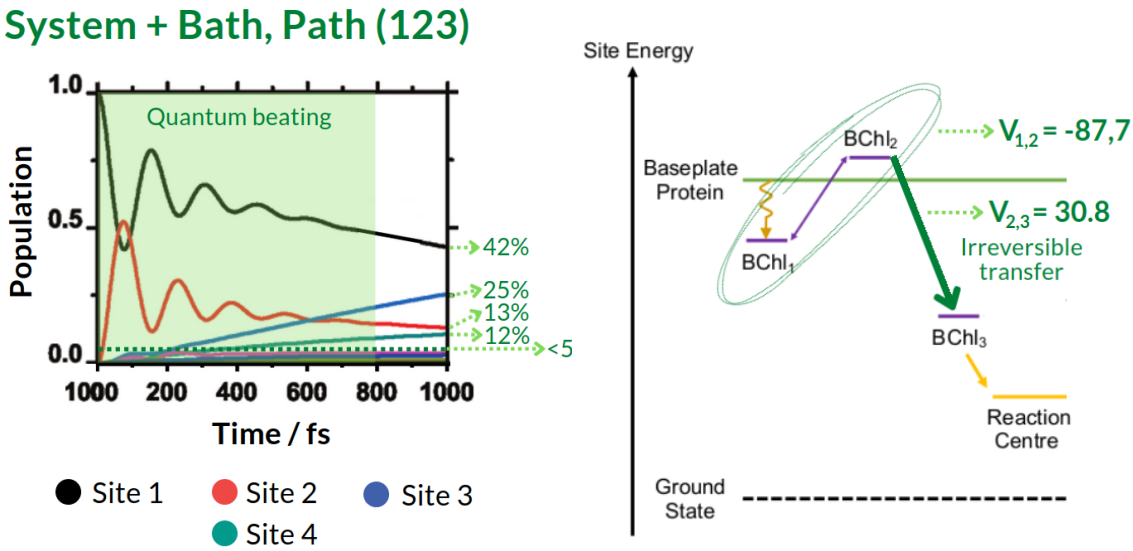

(a) Population initial excitation in site 1 and quantum pathway *123* in the FMO complex [1].

(b) Quantum pathway *123* present in the FMO complex [1].

Figure 1.9: Reduced system and initial excitation population *123* in the FMO complex.

On the other hand, according to J.W. Abbott in Ref.[1], considering the reduced system plus the environment with the initial excitation at site 1 get figure 1.9a. Where the black line represents site 1, the red one for site 2, the blue one for site 3, and the green one for site 4. This figure shows how the observed quantum beating, representing coherence, persists for up to 800 fs. This oscillation results from the ability of the exciton to tunnel between site 1 and site 2 with sufficient energy to

return to site 1, initiating a cyclic process. Simultaneously, there is an increase in the population at site 3, indicating ongoing transport. Initially, there is no population at site 3, but at the end, it reaches about 25%.

On the other side, figure 1.9b indicates a significant energy difference between sites 2 and 3, resulting in irreversible transport. In this case, excitons can only move forward and cannot return. Moreover, the influence of the other sites is negligible (see figure 1.9a). Sites 5, 6, and 7 consistently maintain a population below 5%, while site 4 reaches about 12% at the end. Although Site 4 may have an impact on system response, it is not considered in this study.

In light of these findings, we may identify several functional subsystems within the FMO light-harvesting complex that exhibit comparable efficiencies to the entire FMO complex. Surprisingly, many of these subsystems exceed the overall efficiency of transferring energy from either chromophore 1 to the reaction center. Remarkably, the *123* subsystem stands out as being even more efficient at transferring energy.

1.4 Quantum Coherence in FMO Complex

As previously noted in the section 1.1, the presence of long-lived coherences in the FMO complex has been experimentally measured, which leads us to wonder: How does coherence originate in the FMO? and Does it have any implications for its high efficiency? Chapter 6 in Ref.[6] serves as a foundational reference in answering these questions.

Fundamentally, the coherence of the FMO is often attributed to the strong coupling with vibrational modes. For instance, in Ref.[64] these discrete modes are coupled to the electronic degrees of freedom, existing on the same time scale as the EET. The analysis indicates that strong coupling between the modes and excitons results in the formation of polaritons that have weak coupling with the phonon background and, through this mechanism, the effective coupling between excitons and the environment is decreased, which may contribute to the long-lived coherence of electronic and excitonic states.

For the analysis of the relation between coherence and efficiency, an appropriate basis must be chosen to define incoherent states and operations; which largely depends on the specific process being studied. Within the FMO model's EET, two crucial basis are considered: the occupation basis (see section 1.2.2) and the excitation basis, defined by the Hamiltonian eigenbasis. The occupation base's coherence is a result of self-state delocalization, leading to potential dependence over time due to environmental interaction. This coherent delocalization on the pigments can be exemplified by comparison with multiple slits, since the maximum in the interference pattern depends on the number of slits. Interference increases the likelihood of arrival in specific spatial and temporal regions; in that order of ideas, constructive relocation has the potential to enhance the EET's efficiency, however, it can also be destructive (incoherent). To optimize EET's efficiency, a balanced interaction between both types of delocalization must be maintained. It is important to note that the relationship between the diagonal and non-diagonal elements of the state operator's matrix representation characterizes coherent delocalization.

Ref.[60] investigates the relation between the coherent delocalization of excitations and EET efficiency under different initial conditions. All pigments within the network possess the same excita-

tion energy, and electron-hole recombination, capture, and dephasing processes are incorporated to simulate EET dynamics. EET efficiency is defined as the probability of an excitation reaching the final site pigment, weighted by time. The EET mechanisms are found to be equivalent regardless of whether the initial condition is considered a coherent or incoherent state; meaning that coherently induced EET, such as by a laser pulse, can be used to investigate EET mechanisms in the same system when the initial excitation is induced incoherently, as is the case with sunlight.

On the other hand, in Ref.[4] FMO's robustness is examined via a study on the EET efficiency causal to initial conditions and the removal of pigments and pigment couplings. Results show a decrease in EET efficiency of only about 20% when up to three pigments, excluding the initially excited and sink pigments, are removed compared to the full network. However, the efficiency is more sensitive to random coupling removal. We confirm that pigment subsystem *123* works independently as a separate entity when pigment 1 is initially excited, justifying our decision to concentrate on this subsystem. They also analyze the optimization of the FMO by simulating the efficiency of FMO-like networks with different excitation energies and couplings. In those cases, although it is possible to build networks with greater efficiency for a given initial condition, the FMO is the network with the highest EET efficiency for all types of initial conditions.

The system environment can be a valuable resource for efficient EET. Specifically, environment-assisted quantum transport (ENAQT) could improve the efficiency of EET from the antenna molecules to the reaction center in a photosynthetic complex such as FMO. Efficient EET can be achieved with a combination of coherent EET and dephasing dynamics, but the nature of the environment's role varies based on different models, initial conditions, and EET efficiency definitions. The mechanism of ENAQT can be explained by two hypotheses, in one the environment suppresses pathways that do not increase the likelihood of finding excitation at the final site, on the other, the environment induces fluctuations in excitation energies, allowing two non-resonant pigments to become resonant at certain points in time. Ref.[44] investigates the effect of a complex network's spatial structure on its efficiency, this study uses a model with three pigments and examines both Markovian and non-Markovian environmental effects. Results show that EET efficiency remains robust despite environmental effects, while quantum coherence plays a role in EET. This coherence induces faster EET, causing it to occur before the ambient destruction of coherent oscillations.

Likewise, in Ref.[45], the information flow between the system and the environment is studied in the EET process of the FMO complex, the EET dynamics is modeled using the hierarchical equations of motion (HEOM) method. To determine the extent of non-Markovianity present in a dimer, optimized initial conditions and pairs of initial states are utilized. In addition, the environment undergoes a time scale variation between 50 and 150 fs, while the temperature remains fixed at 288 K. Non-Markovianity is heavily reliant on molecular coupling when the reorganization energy is set to 35 cm^{-1}. When the coupling is zero, non-Markovianity vanishes because the two states can be perfectly distinguished. The study also examines the relationship between non-Markovianity and the environmental time scale and reorganization energy, revealing that a longer environmental time scale results in a consistent increase in non-Markovianity. Weak coupling with the environment results in quasi-unitary dynamics without non-Markovian effects. Conversely, strong coupling leads to dynamics in the incoherent regime where non-Markovianity disappears.

Next, non-Markovianity in the FMO complex is investigated: first, the dependence of non-Markovianity on the environmental time scale is investigated while maintaining a reorganization energy of

35 cm^{-1}, noting that the result is very similar to the dimer case. Secondly, the dependence of the reorganization energy is analyzed when the environmental time scale is set at 150 fs. They found that non-Markovianity reaches its peak of 55 cm^{-1} with this setup. This indicates that non-Markovianity and EET efficiency both reach their maximum in the same environmental regime. Therefore, non-Markovianity may function to preserve coherence, which could prove critical for the pigment pathway $1 \rightarrow 2 \rightarrow 3$. This is particularly relevant since pigment 2 possesses higher excitation energy than pigment 1.

Finally, this study presents delocalization, the ENAQT mechanism, and non-Markovianity as connecting elements between quantum coherence and FMO efficiency. These findings emphasize the intricate and interconnected factors that impact the complex's overall efficiency, offering valuable insights into understanding its operation.

1.5 Efficiency in FMO Complex

The efficiency of the FMO complex refers to the ability of the complex to transfer absorbed light energy from one pigment molecule to another with minimal loss. The FMO complex exhibits high energy transfer efficiency, which is essential for efficient photosynthesis. The distribution of molecules in the complex is arranged to form a network of electronic interactions that allow efficient energy transfer, and energy is transferred from one pigment molecule to another through resonant dipole-dipole interactions. Due to the great importance of the efficiency of photosynthetic processes in the FMO within the survival of green sulfur bacteria, this work seeks to characterize this observable through different strategies that allow us to contribute more to the discussion about its possible relationship with the quantum coherence of the system. The efficiency of energy transfer in the FMO complex arises due to several factors, some of which are explored in depth by C. Bengtson in Ref.[6]:

1. **Structural organization:** The arrangement of the pigment molecules in the FMO complex is optimized to minimize energy losses. The specific geometry and spatial arrangement of the pigment molecules create a pathway for efficient energy transfer.

2. **Electronic coupling:** The pigment molecules in the FMO complex are electronically coupled, meaning that the energy levels of the pigment molecules are finely tuned to facilitate efficient energy transfer. This electronic coupling ensures that the energy transfer occurs rapidly and efficiently.

3. **Environmental protection:** The FMO complex is shielded from the surrounding environment, preventing external factors from interfering with energy transfer. The protein scaffold surrounding the pigment molecules helps to protect them from interactions that could cause energy losses.

4. **Coherent dynamics:** Energy transfer in the FMO complex exhibits coherence, meaning the excitation is simultaneously delocalized over multiple pigment molecules. This coherent behavior allows for the efficient transfer of energy without dissipative losses.

However, there is no consensus on the appropriate way to measure efficiency. Depending on the tool used, e.g. Lindblad or Green's functions, it might be more appropriate and functional to work with a certain expression for efficiency.

1.5.1 Lindblad Formalism

This approach defines the observables that allow us to calculate the population of excitons at each level, i.e. in the BChl-a molecules simultaneously. In the first definition, the excitonic current is a direct measure of the efficiency in the FMO, since this (even the quantum) is simply the ratio between the output power and the input power [20]. The input power is constant and the output power is essentially the exciton energy multiplied by the exciton current.

$$\text{Efficiency} = \frac{\text{Output Power}}{\text{Input Power}} \longrightarrow \eta = \frac{\varepsilon_e J_e}{c}, \text{ c is constant.} \tag{1.8}$$

Moreover, the populations allow evaluation of how quantum the system is. Through a connection between the exciton population, the dephasing rate, and the approach to the classical regime, through the mechanism ENAQT. This last is the situation in which the quantum transport dependence on the dephasing rate is not monotonic, but shows a maximum at some optimal dephasing rate, and has therefore been considered as a possible mechanism for the high efficiency of photosynthetic complexes [20].

It is worth mentioning that this description is not very functional, since it is necessary to define adequately the current and the energy of the exciton. Thus, similar but much more practical approaches can be used for the purpose of this work:

1. According to N. Renaud, et al. in Ref.[48] we can consider only output efficiency overall time,

$$\bar{\eta}_s(\gamma_{\text{deph}}) = \frac{1}{t_{max}} \int_0^{t_{max}} \rho_{3,3}(t)\ dt, \tag{1.9}$$

   The motivation for measuring the efficiency of exciton transfer lies in its ability to gauge the level of population in the target state during excitonic transport. Moreover, it provides an easy way to monitor the system's relaxation (relative to the dephasing rate) as its environmental interactions fluctuate [48].

   It is important to note that this study shows how different features of excitonic transfer efficiency are captured based on the maximum time value. If the maximum time is significantly greater than the relaxation time, the efficiency depends primarily on the maximum amplitude of the target state population. However, for shorter periods, efficiency is more strongly influenced by the rate of reaching this maximum population [48]. For our case, it is necessary to capture the initial exciton transfer events for most dephasing rates within a maximum time of 10 ps.

   The previous expression is motivated by P. Rebentrost, et al. in Ref.[46] who employed a simple measurement to explain energy transport. They defined the integrated probability of a specific excitonic state up to a maximum time τ, which is their only free parameter. No explicit introduction of capture sites or additional parameters is needed, according to their claim. The measure is provided by

$$\bar{P}_M = \frac{1}{\tau} \int_0^{\tau} dt \langle M|\rho(t)|M\rangle, \tag{1.10}$$

   where τ represents the maximum total integration time, and $|M\rangle$ is a specific exciton state as determined by the problem. They have opted for the exciton state $|M\rangle$ and concentrated

solely on the relaxation dynamics at the base of the exciton [46]. The state to be measured within the FMO complex is the exciton located in site 3, which possesses the lowest energy.

Finally, according to P. Rebentrost, et al. in Ref.[47] the efficiency of the FMO in terms of the probability of successfully capturing the exciton at a designated target site within a fixed time interval. This probability can be determined by the following equation:

$$2\kappa_m \langle m|\rho(t)|m\rangle \mathrm{d}t.$$

Therefore, efficiency can be defined as the integrated probability of capture at multiple sites:

$$\bar{\eta} = 2\sum_m \kappa_m \int_0^\infty \mathrm{d}t \ \langle m|\rho(t)|m\rangle, \tag{1.11}$$

being that in our case of interest, the only target site is the extraction site, that is, site 3. In this scenario, $2\kappa_3$ would be connected to the maximum relaxation time of the system. This would result in the definite integral being truncated.

The decision to use an integral on the probability of a successful capture in chromophore 3 for a maximum time to elucidate the behavior of the average efficiency of the reduced FMO system is justified because, if we start from a zero instant where there is no population at site 3 and, after a certain time, that population increases because transportation is being favored in the complex through the appropriate value of the dephasing rate. This is related to the regime in which the system is found, favoring magnitudes of this rate related to an intermediate regime between the purely classical or quantum regime (the so-called ENAQT), it is because the average efficiency of this transport has a direct relationship with the behavior of the populations during that time.

The equation 1.9 for the average efficiency is the one used in the most of references consulted [46–48] since it does not take into account the variations over time of the population at site 1, it will be called from now on **Statical Efficiency**.

2. As mentioned above, and after a significant number of tests, we noticed that although the functional form of the efficiency given by equation 1.9 presented an important maximum for a specific value of dephasing rate, the efficiency scale is very low, being below 30% at its maximum value. Although this result makes sense if we compare it with the results given by the populations, we conclude that it could be useful to apply the same expression but follow the model of the average efficiency seen as output power over input power. For this case, the output power would be the equation 1.9, and the input power would be

$$\bar{P}_I = \frac{1}{t_{max}} \int_0^{t_{max}} \rho_{1,1}(t) \ dt. \tag{1.12}$$

Therefore, in the form of the average efficiency seen from the previous point, the input power would be equal to unity. But, in this case, it would be defined by the equation 1.12 which is related to the probability of eviction of the excitons in chromophore 1 for a maximum time. Even if the results are more or less accurate concerning what was expected, it opens another possibility for us to compare with what was obtained using another tool. In summary, it is an extra perspective that we desire to explore for the analysis of the average transportation

efficiency in the FMO complex. Since this does consider the variations over time of the population at site 1, we will call it **Dynamical Efficiency** and its final expression would be

$$\bar{\eta}_d(\gamma_{\text{deph}}) = \frac{\int_0^{t_{max}} \rho_{3,3}(t)\ dt}{\int_0^{t_{max}} \rho_{1,1}(t)\ dt}. \tag{1.13}$$

1.5.2 Green's Functions Formalism

An alternative approach to evaluate the performance of a molecular junction is through the macroscopic efficiency of the junction. This efficiency is akin to the traditional thermodynamic efficiency of a heat engine, quantifying the fraction of average power output extracted from the heat derived from the hot source. While it remains well-defined far from equilibrium, it is also upper-bounded by the Carnot efficiency. However, when considering the nanoscale, non-equilibrium aspects of the molecular junction are not the sole characteristics to be considered. Given the small size of the system, thermal fluctuations assume a much more significant role than in bulk samples. Consequently, the junction's performance exhibits substantial variability. To account for this variability and characterize the energy conversion statistically, stochastic thermodynamics methods must come into play [13].

However, we aim to establish a direct link between Green's functions and Lindblad formalisms by deriving an expression for the average efficiency comparable to the Dynamical Efficiency (see equation 1.13) for Green's functions. To achieve this, we have chosen to utilize Parseval's theorem. This theorem asserts that when a Fourier transform is applied, the integral of the squared magnitude of a function in the time domain equals the sum of its coefficients squares in the frequency domain.

$$\int_{-\infty}^{\infty} |y(t)|^2 dt = \frac{1}{2\pi} \int_{-\infty}^{\infty} |A(\omega)|^2 d\omega. \tag{1.14}$$

A slightly modified version of Parseval's theorem for Fourier integrals has applicability in quantum mechanics. For this case, it deals with the representation of wave functions using sets of orthogonal functions. When wavefunctions are normalized, the theorem postulates that the squared norm in Hilbert space of a wavefunction equals the sum of the squares of its coefficients in the expansion using functions from an orthogonal basis. The equation is defined by

$$\int_{-\infty}^{\infty} \Psi^*(x,t)\Psi(x,t)\ dx = \int_{-\infty}^{\infty} A^*(p)A(p)dp, \tag{1.15}$$

where $\Psi(x,t)$ represents the wavefunction in real space and $A(p)$ represents the wavefunction in momentum space. The left-hand side of equation 1.15 is the probability of locating a particle in the range of $x = -\infty$ to $x = \infty$, i.e., the wavefunction $\Psi(x,t)$ is normalized. Since the particle must exist somewhere, this probability equals one. The right-hand side indicates the probability that the particle has a momentum p in the range of $p = -\infty$ to $p = \infty$. When $A(p)$ is normalized, this probability is equal to one [25].

Starting from the above, the density operator of the system $\rho(t)$ obtained with the Lindblad formalism can be related to the spectral function $A(E)$, calculated using Green's functions. The sum of the probabilities of measuring the population at sites 1, 2, and 3 during the maximum time must equal one. Similarly, the sum of the probabilities amplitudes for the creation or annihilation of particles at each site for the maximum energy range must also be equal to 2π, this is called the

sum rule [43, 51]. Besides, the spectral function is related to the density of states because the last one is the trace of this spectral function.

$$A(E) = Tr\{\boldsymbol{A}(E)\} = -\frac{1}{\pi}\Im m\left\{ Tr\left\{G^R_{ii}(\omega)\right\}\right\}. \tag{1.16}$$

Recall that the density of states indicates the number of quantum states per unit energy range in a system. If the density of states represents the probability density of finding a quantum state with energy E, then integrating it over the entire energy range yields a value of one. This is because the total probability of finding the particle in some state must be one, meaning the particle must be in some state within the system [43]. The statement above leads to an equivalent formulation of the Parseval theorem for our specific scenario,

$$\int_{t_{min}}^{t_{max}} \mathrm{Tr}[\mathscr{P}(t)]\ dt = \int_{E_{min}}^{E_{max}} \mathrm{Tr}[\boldsymbol{A}(E)]\ dE, \tag{1.17}$$

where $\mathrm{Tr}[\mathscr{P}(t)]$ is the trace of the matrix representation of the density operator of the system in the occupation base, while $\mathrm{Tr}[\boldsymbol{A}(E)]$ is the trace of the spectral function matrix in the same basis, in other words, the density of states.

By establishing a connection between the density of states and the state operator, it is possible to establish an equation for the Dynamical Efficiency based on the density of states of the system, since this contains the same information; this development will be expanded in the section 3.6. Using Green's functions, we can propose a practical expression for this efficiency, analogous to the approach utilized with the Lindblad formalism, given by

$$\bar{\eta}_d(\Gamma) = \frac{\int_{E_{min}}^{E_{max}} A_3(E)\ dE}{\int_{E_{min}}^{E_{max}} A_1(E)\ dE}. \tag{1.18}$$

Starting from the equation 1.18 we have an expression of the Dynamical Efficiency that we can use to compare the two formalisms that we have at hand to analyze the problem.

Chapter 2

FMO Dynamics: Lindblad Framework

The Lindblad master equation is a mathematical framework that has been widely used to describe the dynamics of open quantum systems. This formalism effectively captures the time evolution of a quantum system, taking into account both coherent dynamics and dissipative processes such as relaxation and decoherence. This equation is derived from the Markov approximation, which assumes negligible effects of memory on system-environment interaction. Moreover, it is frequently obtained utilizing a perturbative approach, assuming weak coupling between the system and the environment. Therefore, this assumption may not hold on very short time scales, where non-perturbative effects become significant. When discussing time scales, the Lindblad equation proves useful when there is a clear difference in energy scales between the system and the environment. However, in cases where energy scales are comparable, it may be necessary to include additional terms to accurately depict the dynamics [8, 59].

In the specific case of the FMO complex, the Lindblad master equation incorporates several mechanisms that affect the efficiency of energy transfer. These mechanisms include electronic couplings between the BChl-a molecules, relaxation processes resulting from interactions with the environment (such as vibrations and protein scaffold fluctuations), and dephasing processes. Using the Lindblad master equation formalism, researchers have been simulating and analyzing the dynamic behavior of the FMO complex under realistic conditions. Studying, for example, the efficiency of energy transfer within the complex [11, 24, 62].

As mentioned before, the Lindblad master equation has certain limitations when applied to condensed matter systems. For that reason, alternative methods such as non-equilibrium Green's functions have emerged to provide a more accurate representation of physical observables under mentioned conditions, which is of fundamental importance in condensed matter physics [30, 42]. Nevertheless, the quantum master equation still allows for the straightforward extraction of population and coherence information. This facilitates the analysis of whether a system remains in a quantum coherent state at a given time or transition.

2.1 Lindblad Master Equation

In the development of open quantum systems, a Markovian method is approached through the Lindblad quantum master equation. This was developed by Vittorio Gorini, Andrzej Kossakowski, George Sudarshan [18] and Göran Lindblad [36] in 1976 and is a consistent theory that allows modeling non-unitary dynamics. This means, it allows modeling the dynamics of the system when influenced by the reservoirs only in terms of the degrees of freedom of the system itself, making not necessary to know the degrees of freedom of the reservoirs, hence, influence on the system can be represented by the spectral density [1, 59].

The Lindblad quantum master equation, which talks about the change of the state operator with respect to time is given by,

$$\frac{d}{dt}\rho = -\frac{i}{\hbar}[H,\rho] + \sum_k \Gamma_k \left(L_k \rho L_k^\dagger - \frac{1}{2}\left\{ L_k L_k^\dagger, \rho \right\} \right) \equiv \mathcal{L}\rho, \tag{2.1}$$

the first term of equation 2.1 is related to the closed system, i.e. the system without an environment around. The second term contains the Lindbladian operators and the interaction rates, which take into account the non-unitary processes between the system and the environment, in particular, the interaction rates show how strong is the coupling with the bath [39, 49]. In figure 2.1 we can see a diagram that exemplifies the hierarchies within the physical system: the total system contains the environment and, within it, is the subset of the system.

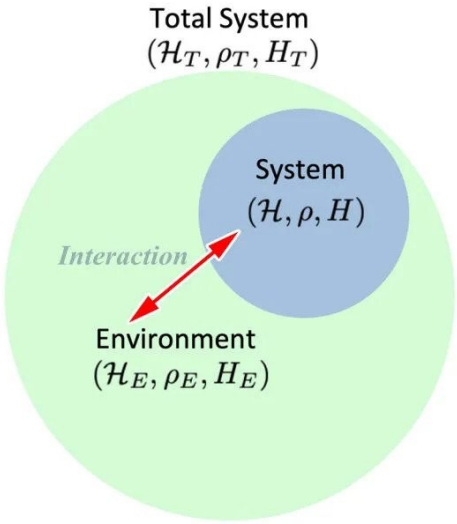

Figure 2.1: Scheme representing the total system divided into the system of interest and the environment [39].

2.1.1 FMO Complex Master Equation

Coming back to the FMO context, in this work we follow Ref.[11] for the construction of the FMO master equation. It is known that the system energy is continuously injected into the ETC from the antenna and extracted from the reaction center at fixed rates of γ_{inj} and γ_{ext}, respectively. Both the injection and extraction processes are incoherent and continuous, but it is not only the interaction

with the source and sink that causes the exciton to lose its coherence, hence the coherence at each site is represented by a dephasing rate γ_{deph}.

Following Ref.[11], all the information about the action of the environment is completely determined by the interaction rates for injection, γ_{inj}; for extraction, γ_{ext}; and, for dephasing, γ_{deph}. The conventional unitary quantum dynamics is modified so that the reservoirs extract information from the physical system. The quantum dynamics of the state operator is thus separated into unitary and non-unitary contributions related to the reservoirs, and this is given by the Lindblad master equation:

$$\frac{d\rho}{dt} = -\frac{i}{\hbar}[H_S,\rho] + L_{\text{inj}}[\rho] + L_{\text{ext}}[\rho] + L_{\text{deph}}[\rho], \tag{2.2}$$

$$\begin{aligned}
L_{\text{inj}}[\rho] &= \gamma_{\text{inj}}\left[\rho_{0,0}|1\rangle\langle 1| - \frac{1}{2}\left(\sum_{m=0}^{n}\rho_{0,m}|0\rangle\langle m| + \sum_{m=0}^{n}\rho_{m,0}|m\rangle\langle 0|\right)\right], \\
L_{\text{ext}}[\rho] &= \gamma_{\text{ext}}\left[\rho_{3,3}|0\rangle\langle 0| - \frac{1}{2}\left(\sum_{m=0}^{n}\rho_{3,m}|3\rangle\langle m| + \sum_{m=0}^{n}\rho_{m,3}|m\rangle\langle 3|\right)\right], \\
L_{\text{deph}}[\rho] &= \gamma_{\text{deph}}\sum_{i}\left[\rho_{i,i}|i\rangle\langle i| - \frac{1}{2}\left(\sum_{m=0}^{n}\rho_{i,m}|i\rangle\langle m| + \sum_{m=0}^{n}\rho_{m,i}|m\rangle\langle i|\right)\right],
\end{aligned} \tag{2.3}$$

hence $L_{\text{inj}}[\rho]$, $L_{\text{ext}}[\rho]$ and $L_{\text{deph}}[\rho]$ are the Lindbladians of injection, extraction, and dephasing, respectively; where the first refers to the injection of excitons that takes place in chromophore 1, the second has to do with the extraction in chromophore 3 and the third talks about the dephasing that occurs in each of the 7 chromophores; these Lindbladians represent the non-unitary dynamics of the system. Moreover, there are the corresponding Lindblad operators $V_{\text{inj}} = \sqrt{\gamma_{\text{inj}}}a^{\dagger}_{\text{inj}}, V_{\text{ext}} = \sqrt{\gamma_{\text{ext}}}a_{\text{ext}}$, which describe the creation and annihilation of an exciton at the injection and extraction sites, as well as the dephasing operator given by $V_{\text{deph}} = \sqrt{\gamma_{\text{deph}}}\sum_i a^{\dagger}_i a_i$; so that these operators are related to Lindbladians by $L[\rho] = -\frac{1}{2}\left\{V^{\dagger}V,\rho\right\} + V\rho V^{\dagger}$.

2.1.2 Coupling Matrix of the FMO Complex

One of the first important steps in this work is to define the parameters of the system, in other words, it is necessary to determine the energies of each of the levels within the FMO and the couplings between them. To start with, we analyze three different references that show the matrix form of the Hamiltonian of the system in the occupation base $|i\rangle = |\psi_{g,1}\rangle\ldots|\psi_{e,i}\rangle\ldots|\psi_{g,7}\rangle$ (see section 1.2.2):

1. From E. Z. Harush and Y. Dubi in Ref.[20], units cm^{-1}:

$$\boldsymbol{H}_{FMO} = \begin{pmatrix}
12335 & -106 & 8 & -5 & 6 & -8 & -4 \\
-106 & 12475 & 28 & 6 & 2 & 13 & 1 \\
8 & 28 & 12055 & -62 & -1 & -9 & 17 \\
-5 & 6 & -62 & 12230 & -70 & -19 & -57 \\
6 & 2 & -1 & -70 & 12375 & 40 & -2 \\
-8 & 13 & -9 & -19 & 40 & 12415 & 32 \\
-4 & 1 & 17 & -57 & -2 & 32 & 12315
\end{pmatrix}, \tag{2.4}$$

2. From D. Hayes and G. S. Engel in Ref.[22], units cm^{-1}:

$$\boldsymbol{H}_{FMO} = \begin{pmatrix} 12468 & -53 & 5 & -4 & 4 & -6 & -5 \\ -53 & 12466 & 17 & 6 & 1 & 6 & 5 \\ 5 & 17 & 12129 & -38 & -3 & -7 & 25 \\ -4 & 6 & -38 & 12410 & -60 & -8 & -48 \\ 4 & 1 & -3 & -60 & 12320 & 33 & -8 \\ -6 & 6 & -7 & -8 & 33 & 12593 & 38 \\ -5 & 5 & 25 & -48 & -8 & 38 & 12353 \end{pmatrix}, \tag{2.5}$$

found with the functional form,

$$V_{j\neq k} = s\left(R_{jk}\right) \frac{1}{R_{jk}^2} \left[\vec{\mu}_j \cdot \vec{\mu}_k - 3\left(\vec{\mu}_j \cdot \hat{\mathrm{e}}_{jk}\right)\left(\vec{\mu}_k \cdot \hat{\mathrm{e}}_{jk}\right)\right]. \tag{2.6}$$

3. From J. Adolphs and T. Renger in Ref.[2], units cm^{-1}:

$$\boldsymbol{H}_{FMO} = \begin{pmatrix} 12410 & -87.7 & 5.5 & -5.9 & 6.7 & -13.7 & -9.9 \\ -87.7 & 12530 & 30.8 & 8.2 & 0.7 & 11.8 & 4.3 \\ 5.5 & 30.8 & 12210 & -53.5 & -2.2 & -9.6 & 6.0 \\ -5.9 & 8.2 & -53.5 & 12320 & -70.7 & -17.0 & -63.3 \\ 6.7 & 0.7 & -2.2 & -70.7 & 12480 & 81.1 & -1.3 \\ -13.7 & 11.8 & -9.6 & -17.0 & 81.1 & 12630 & 39.7 \\ -9.9 & 4.3 & 6.0 & -63.3 & -1.3 & 39.7 & 12440 \end{pmatrix}, \tag{2.7}$$

found with the functional form,

$$V_{mn} = f \frac{\mu_{\text{vac}}^2}{R_{mn}^3} \left[\vec{e}_m \cdot \vec{e}_n - 3\left(\vec{e}_m \cdot \vec{e}_{mn}\right)\left(\vec{e}_n \cdot \vec{e}_{mn}\right)\right]. \tag{2.8}$$

Here we can analyze that the different matrices have the same structure with the maximum and minimum values with the same order of magnitude, and the positive and negative magnitudes stand for the same couplings (blue and red numbers, respectively). In this work, we follow Ref.[2] where the authors argue that the point dipole approximation works well and that the main effect on the couplings is due to the dielectric environment.

The matrix has 49 elements, being symmetric, only 28 of them are independent. However, we can take the submatrix only for sites 1, 2, and 3, and make the coupling between levels 1 and 3 approximately equal to zero because it is an order of magnitude smaller compared to the other couplings. This decision is motivated by the quantum redundancy present in the FMO complex (see section 1.3).

$$\boldsymbol{H}_{FMO-123} = 1\ cm^{-1} \times \begin{pmatrix} 12410 & -87.7 & 5.5 \\ -87.7 & 12530 & 30.8 \\ 5.5 & 30.8 & 12210 \end{pmatrix} \approx 1\ cm^{-1} \times \begin{pmatrix} 12410 & -87.7 & 0 \\ -87.7 & 12530 & 30.8 \\ 0 & 30.8 & 12210 \end{pmatrix}. \tag{2.9}$$

Henceforth, the matrix representation of our sub-system *123* under consideration is given by equation 2.9 and it is labeled from now on as "the system", where additionally the site 0 is introduced as the vacuum of the system as an absence of excitons in the FMO complex. In the next section, the Lindblad formalism is settled down for this subsystem composed of 4 sites or states $\{0, 1, 2, 3\}$.

2.2 Population of the Sites with Lindblad Formalism

2.2.1 Matrix Form of the Lindblad Equation for FMO-123

Once the system matrix has been decided and the functional forms of the Lindbladians have been taken into account (see equation 2.4), the Lindblad master equation can be determined in the matrix representation of the occupation basis as,

$$\begin{aligned} \frac{d\rho}{dt} &= \underbrace{-\frac{i}{\hbar}[H_{FMO-123},\rho]}_{\mathbb{M}_1} + \underbrace{\mathcal{L}_{\text{inj}}[\rho]}_{\mathbb{M}_2} + \underbrace{\mathcal{L}_{\text{ext}}[\rho]}_{\mathbb{M}_3} + \underbrace{\mathcal{L}_{\text{deph}}[\rho]}_{\mathbb{M}_4}, \\ \longrightarrow \quad \dot{\mathscr{P}} &= (\mathbb{M}_1 + \mathbb{M}_2 + \mathbb{M}_3 + \mathbb{M}_4)\,. \end{aligned} \tag{2.10}$$

To define the matrix $\mathbb{M}_1$ it is necessary to expand the term $-\frac{i}{\hbar}[H_{\text{FMO}},\rho]$ [11], as follows,

$$\begin{aligned} -\frac{i}{\hbar}[H_{FMO-123},\rho] = -\frac{i}{\hbar}\Bigg(&\sum_{i=1}^{n}\epsilon_i\left(\rho_{i,0}\left|\psi_i\right\rangle\left\langle\psi_0\right|-\rho_{0,i}\left|\psi_0\right\rangle\left\langle\psi_i\right|\right) + \sum_{m,l=1}^{n}\left(\epsilon_m-\epsilon_l\right)\rho_{m,l}\left|\psi_m\right\rangle\left\langle\psi_l\right| \\ &+\sum_{m,l,i}^{n} J_{i,m}\ \rho_{m,l}\left|\psi_i\right\rangle\left\langle\psi_l\right| - \sum_{m,l,i}^{n} t_{l,j}\rho_{m,l}\left|\psi_m\right\rangle\left\langle\psi_j\right|\Bigg)\,, \end{aligned} \tag{2.11}$$

where the FMO Hamiltonian matrix (in ps^{-1}) is:

$$\boldsymbol{H}_{FMO-123} = 0.188\times\begin{bmatrix} 0 & 0 & 0 & 0 \\ 0 & \varepsilon_1 & t_{1,2} & 0 \\ 0 & t_{1,2} & \varepsilon_2 & t_{2,3} \\ 0 & 0 & t_{2,3} & \varepsilon_3 \end{bmatrix} = 0.188\times\begin{bmatrix} 0 & 0 & 0 & 0 \\ 0 & 12410 & -87.7 & 0 \\ 0 & -87.7 & 12530 & 30.8 \\ 0 & 0 & 30.8 & 12210 \end{bmatrix}, \tag{2.12}$$

where the raw and column for the vacuum state in equation 2.12 has been introduced. Also, the scale factor 0.188 $(cm^{-1})^{-1}\ ps^{-1}$ incorporates the constant $\hbar$ and allows going from energy units to inverse time units, making the expression dimensionally meaningful; the calculation of this factor is presented in appendix A. Since the Hamiltonian is the generator of time translations, its parameters must define the time scale. By using this factor, we change the units of the system's parameters and from them define a new scale. Since the injection, extraction, and dephasing parameters are not known in an absolute way, we create a temporary rescaling factor that allows us to adapt to the characteristic energy scale, which is of the order of 12000 cm^{-1}. In the end, the goal is to find the appropriate parameters set to recover the dynamical behavior observed in previous references. It is also useful to express the state operator in matrix form

$$\mathscr{P} = \begin{bmatrix} \rho_{0,0} & \rho_{0,1} & \rho_{0,2} & \rho_{0,3} \\ \rho_{1,0} & \rho_{1,1} & \rho_{1,2} & \rho_{1,3} \\ \rho_{2,0} & \rho_{2,1} & \rho_{2,2} & \rho_{2,3} \\ \rho_{3,0} & \rho_{3,1} & \rho_{3,2} & \rho_{3,3} \end{bmatrix}. \tag{2.13}$$

Taking all of the above into account, it is possible to define $\mathbb{M}_1$ such that, in this case, exists a parameter α running over two values: $\alpha = 1$ or $\alpha = 0$, this is related with the decision of taking the matrix form of the equation 2.11, i.e., $\alpha = 0$ or taking the commutator explicitly by multiplying matrices 2.12 and 2.13, i.e., $\alpha = 1$. This is explicitly explored in appendix B, and for the calculations

of this section, we consider $\alpha = 1$, hence $\mathbb{M}_1$ is given by,

$$\mathbb{M}_1 = -0.188i\cdot\begin{bmatrix} 0 & -\varepsilon_1\cdot\rho_{0,1} - \alpha\,(t_{1,2}\cdot\rho_{0,2}) \\ \varepsilon_1\cdot\rho_{1,0} + \alpha\,(t_{1,2}\cdot\rho_{2,0}) & t_{1,2}\cdot(\rho_{2,1}-\rho_{1,2}) \\ \varepsilon_2\cdot\rho_{2,0} + \alpha\,(t_{1,2}\cdot\rho_{1,0} + t_{2,3}\cdot\rho_{3,0}) & (\varepsilon_2-\varepsilon_1)\cdot\rho_{2,1} + t_{1,2}\cdot(\rho_{1,1}-\rho_{2,2}) + t_{2,3}\cdot\rho_{3,1} \\ \varepsilon_3\cdot\rho_{3,0} + \alpha\,(t_{2,3}\cdot\rho_{2,0}) & (\varepsilon_3-\varepsilon_1)\cdot\rho_{3,1} - t_{1,2}\cdot\rho_{3,2} + t_{2,3}\cdot\rho_{2,1} \end{bmatrix} \tag{2.14}$$

$$\begin{bmatrix} -\varepsilon_2\cdot\rho_{0,2} - \alpha\,(t_{1,2}\cdot\rho_{0,1} + t_{2,3}\cdot\rho_{0,3}) & -\varepsilon_3\cdot\rho_{0,3} - \alpha\,(t_{2,3}\cdot\rho_{0,2}) \\ (\varepsilon_1-\varepsilon_2)\cdot\rho_{1,2} + t_{1,2}\cdot(\rho_{2,2}-\rho_{1,1}) - t_{2,3}\cdot\rho_{1,3} & (\varepsilon_1-\varepsilon_3)\cdot\rho_{1,3} + t_{1,2}\cdot\rho_{2,3} - t_{2,3}\cdot\rho_{1,2} \\ t_{1,2}\cdot(\rho_{1,2}-\rho_{2,1}) + t_{2,3}\cdot(\rho_{3,2}-\rho_{2,3}) & (\varepsilon_2-\varepsilon_3)\cdot\rho_{2,3} + t_{1,2}\cdot\rho_{1,3} + t_{2,3}\cdot(\rho_{3,3}-\rho_{2,2}) \\ (\varepsilon_3-\varepsilon_2)\cdot\rho_{3,2} - t_{1,2}\cdot\rho_{3,1} + t_{2,3}\cdot(\rho_{2,2}-\rho_{3,3}) & t_{2,3}\cdot(\rho_{2,3}-\rho_{3,2}) \end{bmatrix},$$

the next step is to find the matrices $\mathbb{M}_2$, $\mathbb{M}_3$ and $\mathbb{M}_4$ relative to the Lindbladian for injection, extraction, and dephasing, respectively.

Injection Lindbladian: Matrix $\mathbb{M}_2$, i.e., $\mathcal{L}_{\text{inj}}[\rho]$:

$$\mathbb{M}_2 = -\frac{1}{2}\gamma_{\text{inj}}\begin{bmatrix} 2\rho_{0,0} & \rho_{0,1} & \rho_{0,2} & \rho_{0,3} \\ \rho_{1,0} & -2\rho_{0,0} & 0 & 0 \\ \rho_{2,0} & 0 & 0 & 0 \\ \rho_{3,0} & 0 & 0 & 0 \end{bmatrix}, \tag{2.15}$$

Extraction Lindbladian: Matrix $\mathbb{M}_3$, i.e., $\mathcal{L}_{\text{ext}}[\rho]$:

$$\mathbb{M}_3 = -\frac{1}{2}\gamma_{\text{ext}}\begin{bmatrix} -2\rho_{3,3} & 0 & 0 & \rho_{0,3} \\ 0 & 0 & 0 & \rho_{1,3} \\ 0 & 0 & 0 & \rho_{2,3} \\ \rho_{3,0} & \rho_{3,1} & \rho_{3,2} & 2\rho_{3,3} \end{bmatrix}, \tag{2.16}$$

Dephasing Lindbladian: Matrix $\mathbb{M}_4$, i.e., $\mathcal{L}_{\text{deph}}[\rho]$:

$$\mathbb{M}_4 = -\gamma_{\text{deph}}\begin{bmatrix} 0 & \rho_{0,1} & \rho_{0,2} & \rho_{0,3} \\ \rho_{1,0} & 0 & \rho_{1,2} & \rho_{1,3} \\ \rho_{2,0} & \rho_{2,1} & 0 & \rho_{2,3} \\ \rho_{3,0} & \rho_{3,1} & \rho_{3,2} & 0 \end{bmatrix}. \tag{2.17}$$

2.2.2 Numerical Solution of the State Operator ρ

Numerical simulations have been implemented to solve the Lindblad master equation 2.10 through the Runge-Kutta method of the 4th order (see appendix C), where the temporal dependence of each matrix element ρ_{nm} is written in terms of the interaction rates shown above. To determine these functions, it is necessary to define the set of parameters consistently, in particular, the injection, and extraction rates remain constant, while the dephasing rate is varied. For this study, interaction rates similar to those given by E. Z. Harush and Y. Dubi in Ref.[20] were used.

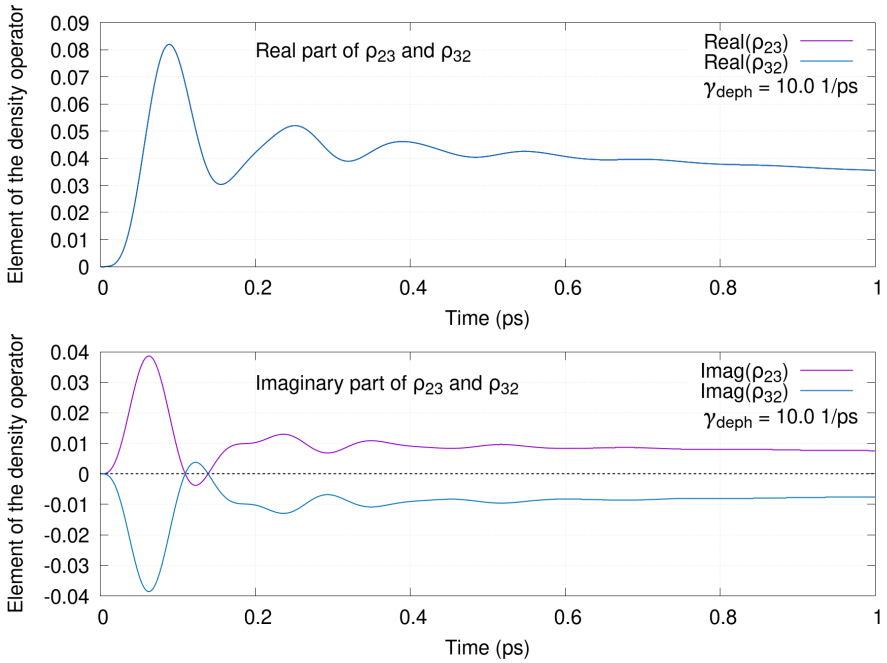

Figure 2.2: Comparison of the real and imaginary parts of the matrix elements of the density operator ρ_{23} and ρ_{32} of the FMO-123 system. We set the parameters $\gamma_{\text{deph}} = 10.0\ ps^{-1}$, $\gamma_{\text{inj}} = 400\ \text{ps}^{-1}$ and $\gamma_{\text{ext}} = 0.1\ \text{ps}^{-1}$.

Before proceeding with the analysis of the system dynamics, it is important to characterize the matrix of the state operator in order to find relationships between its elements that facilitate the interpretation of results. With this in mind, we set the parameters $\gamma_{\text{inj}} = 400\ \text{ps}^{-1}$, $\gamma_{\text{ext}} = 0.1\ \text{ps}^{-1}$, and $\gamma_{\text{deph}} = 10.0\ \text{ps}^{-1}$ to evolve the system for 10 picoseconds (see subsection 2.2.3), given by the energy scale of the system. The first thing to test is if the matrix is symmetric, to do this it is enough to compare the real and imaginary parts of two symmetric elements of the matrix, in this case, ρ_{23} and ρ_{32}, knowing that if they are indeed symmetric, their real parts must be identical and their imaginary parts opposite with respect to the x-axis. This information is presented in figure 2.2. As can be seen in figure 2.2, in fact, the expected behavior of the elements outside the diagonal of the density operator was obtained. In this case, it can be affirmed that the matrix is symmetric as expected due to the intrinsic symmetry of the treated system.

In addition, it is essential to emphasize that the elements outside the diagonal have values different from zero, which represent the *coherences* of the system, related to the quantum coherence of the FMO complex, already discussed in detail in the section 1.4. Next, we could ask about the behavior of a specific population, the most important one for the system, on site 3. We expect it to start from zero and, over time, the population reaches a maximum value that can be maintained well over time; in this case, we would speak of reaching a stationary regime. To observe this, the derivative of the population at site 3 with respect to time is analyzed, as shown in figure 2.3. It can be seen how during the first picosecond, there is a persistence of oscillations (quantum beating) with two critical values, that is, two relative peaks. After that, it begins a monotonically decreasing behavior between 1.0 and 10.0 picoseconds eventually reaching zero, suggesting that it is approaching a steady state when the derivative vanishes. This also suggests that the population at site 3 grows to a maximum value and then remains constant, which is exactly the behavior we wanted to recover from the system in question.

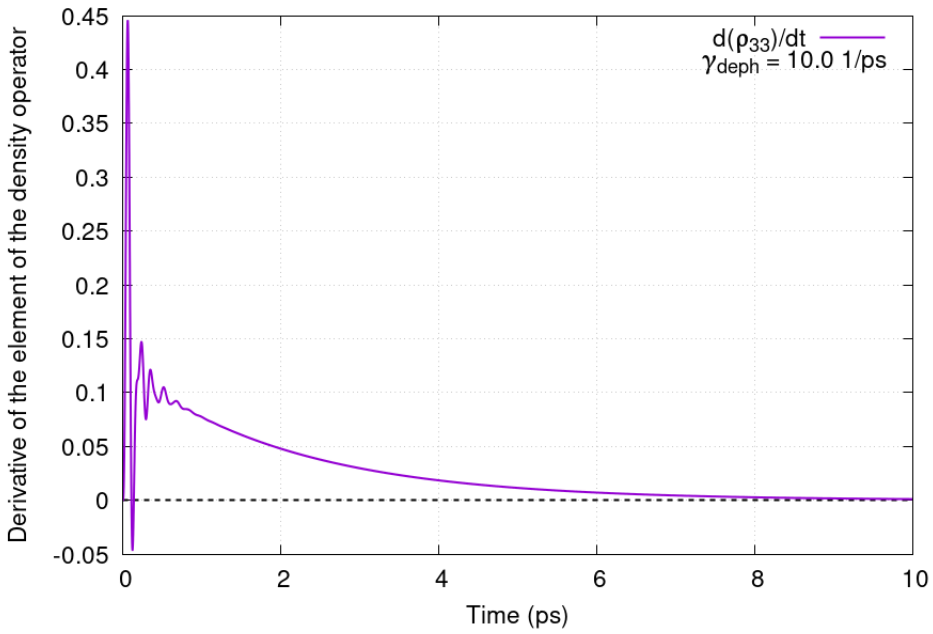

Figure 2.3: Derivative of the population at site 3 for the FMO-123 system, with respect of time. We set the parameters $\gamma_{\text{deph}} = 10.0\ ps^{-1}$, $\gamma_{\text{inj}} = 400\ \text{ps}^{-1}$ and $\gamma_{\text{ext}} = 0.1\ \text{ps}^{-1}$.

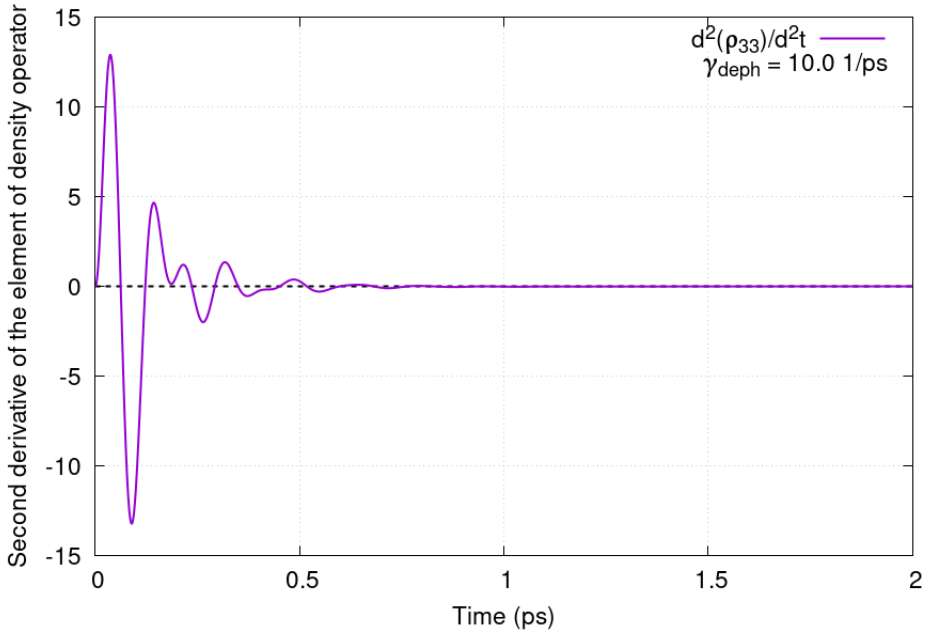

Figure 2.4: Second derivative of the population at site 3 for the FMO-123 system, with respect of time. We set the parameters $\gamma_{\text{deph}} = 10.0\ ps^{-1}$, $\gamma_{\text{inj}} = 400\ \text{ps}^{-1}$ and $\gamma_{\text{ext}} = 0.1\ \text{ps}^{-1}$.

Finally, the behavior of the second derivative of the population at site 3 as a function of time can be analyzed in figure 2.4. Note that in the first 0.5 picoseconds, the same oscillations can be observed as in its first derivative, corresponding to the inflection points typical oscillatory behavior. For the

remaining time, the second derivative approaches zero, again confirming the presence of a steady state for long periods. In this sense, there is a time when the transport reaches a stable maximum that it can maintain over time and, furthermore, it is expected to find a behavior of this type in most cases, at least while the coupling continues to be weak.

2.2.3 Populations of the Levels for FMO-123

The extraction rate can be estimated by considering the time scales of different transport processes that take place in the FMO complex. We set the extraction rate to an average of $\gamma_{\text{ext}} = 0.1$ ps^{-1}. However, a range of extraction rates were tested in [20], and the conclusions are essentially insensitive to its value, as long as it is much larger than the injection rate. On another side, the injection rate is limited by the absorption cross-section, which is estimated by an amount of $\sigma \sim 14$ excitons/s for the biological intensity of $I \sim 18$ $\frac{\text{W}}{\text{m}^2}$. The sunlight intensity can be as high as $I_{\text{max}} \sim 1300$ $\frac{\text{W}}{\text{m}^2}$, which is absorbed by $N \approx 400$ complexes in one vesicle. The resulting upper limit for the injection rate is then $\gamma_{\text{inj}} \sim 400$ ps^{-1} [20]. We note that, despite this estimate, FMO probably does not absorb energy directly from the sun. However, we considered the maximum injection rate that can be obtained from the baseplate, this ensures that our results are appropriate even in extreme conditions. Table 2.1 shows all the considered parameters.

γ_{ext} $(1/ps)$	γ_{inj} $(1/ps)$	γ_{deph} $(1/ps)$
0.1	400	$0.5, 1, 2$ and 5, $[10, 100]$ with $\Delta\gamma = 10$, $[200, 1000]$ with $\Delta\gamma = 100$, 2000 and 2500.

Table 2.1: Dephasing rates with fixed injection and extraction rates for evaluating the dynamics in reduced FMO complex *123* with Lindblad formalism.

Considering the parameters of Table 2.1, we find the diagonal elements of the state operator corresponding to the populations at sites 1, 2, and 3. As can be seen in figure 2.5, the system exhibits a quantum beating between the population at site 1 and site 2. This is observed especially in figure 2.5a, where beating survives throughout all evolved time; and in figure 2.5b, where the beating has a much shorter lifetime, disappearing even before the first picosecond. As the dephasing rate increases, the quantum beating is lost until it vanishes for rates greater than 30.0 ps^{-1}. Figure 2.5c shows how the quantum beating dies before reaching half a picosecond, in the remaining figures there is no trace of quantum beating.

On the other hand, the population at site 3 stabilizes at a value close to 30% and remains constant for the rest of the time, as shown in figures 2.5c, 2.5d, and 2.5e. This behavior was already anticipated in the previous analysis of the state operator (see subsection 2.2.2). Beyond a rate of 100.0 ps^{-1}, the system loses stability and, although the population at site 3 grows monotonically, its maximum population decreases as the dephasing shift rate increases. It is also interesting to emphasize that the vacuum (ground) state population never increases, suggesting that the system is continuously populated with excitons. Regarding the steady state, the system maintains it between 30.0 ps^{-1} and 100.0 ps^{-1}, for higher or lower values of the dephasing shift rate the system requires more time to stabilize. It should be noted that for values around 3000.0 ps^{-1} the simulation explodes, thus it is assumed that for this value the coupling is no longer considered weak. Refer to the population graphs for the whole set of dephasing rate values in appendix D.

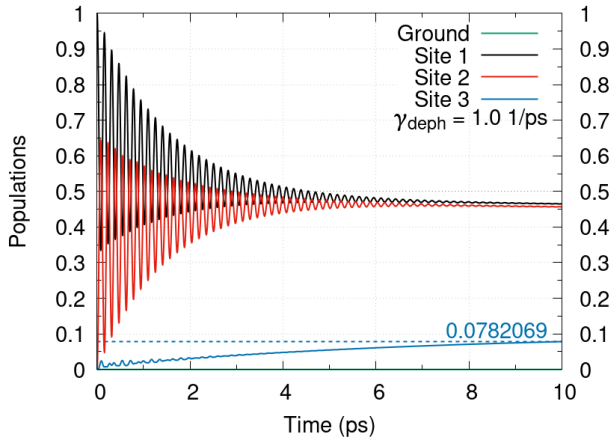

(a) The parameters are $\gamma_{\text{deph}} = 1.0\ ps^{-1}$, $\gamma_{\text{inj}} = 400\ \text{ps}^{-1}$ and $\gamma_{\text{ext}} = 0.1\ \text{ps}^{-1}$.

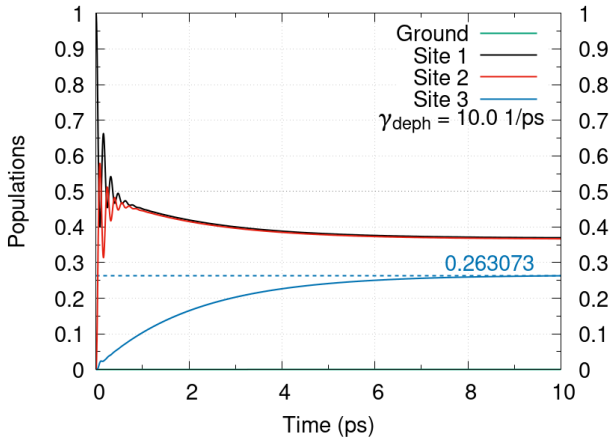

(b) The parameters are $\gamma_{\text{deph}} = 10.0\ ps^{-1}$, $\gamma_{\text{inj}} = 400\ \text{ps}^{-1}$ and $\gamma_{\text{ext}} = 0.1\ \text{ps}^{-1}$.

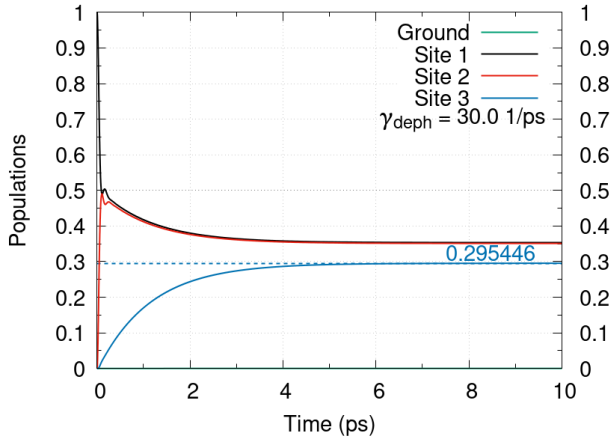

(c) The parameters are $\gamma_{\text{deph}} = 30.0\ ps^{-1}$, $\gamma_{\text{inj}} = 400\ \text{ps}^{-1}$ and $\gamma_{\text{ext}} = 0.1\ \text{ps}^{-1}$.

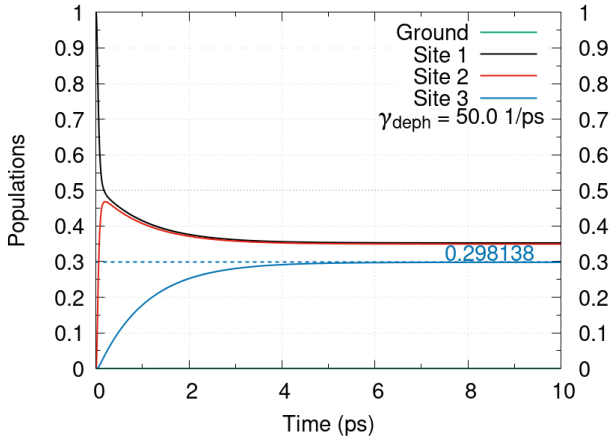

(d) The parameters are $\gamma_{\text{deph}} = 50.0\ ps^{-1}$, $\gamma_{\text{inj}} = 400\ \text{ps}^{-1}$ and $\gamma_{\text{ext}} = 0.1\ \text{ps}^{-1}$.

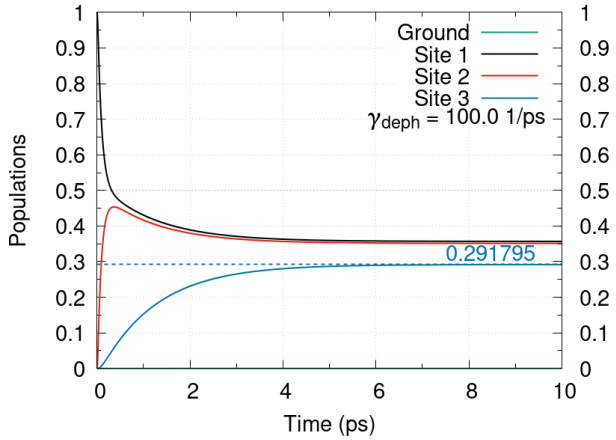

(e) The parameters are $\gamma_{\text{deph}} = 100.0\ ps^{-1}$, $\gamma_{\text{inj}} = 400\ \text{ps}^{-1}$ and $\gamma_{\text{ext}} = 0.1\ \text{ps}^{-1}$.

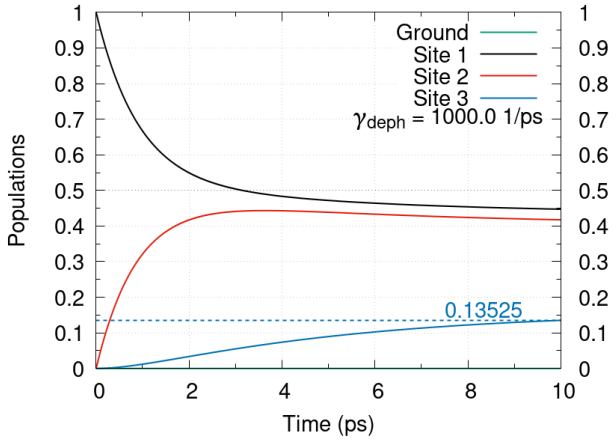

(f) The parameters are $\gamma_{\text{deph}} = 1000.0\ ps^{-1}$, $\gamma_{\text{inj}} = 400\ \text{ps}^{-1}$ and $\gamma_{\text{ext}} = 0.1\ \text{ps}^{-1}$.

Figure 2.5: Population in the reduced FMO-123 system with (a) $\gamma_{\text{deph}} = 1.0\ ps^{-1}$, (b) $\gamma_{\text{deph}} = 10.0\ ps^{-1}$, (c) $\gamma_{\text{deph}} = 30.0\ ps^{-1}$, (d) $\gamma_{\text{deph}} = 50.0\ ps^{-1}$, (e) $\gamma_{\text{deph}} = 100.0\ ps^{-1}$, and (f) $\gamma_{\text{deph}} = 1000.0\ ps^{-1}$.

By isolating the values of the maximum population at site 3, a collection of data can be generated that allows us to find essential relationships between this property and the dephasing rate. The information has been compiled in table E.1 (see appendix E), and plotted in figure 2.6, it displays a maximum value for the population at site 3 as a function of the dephasing rate.

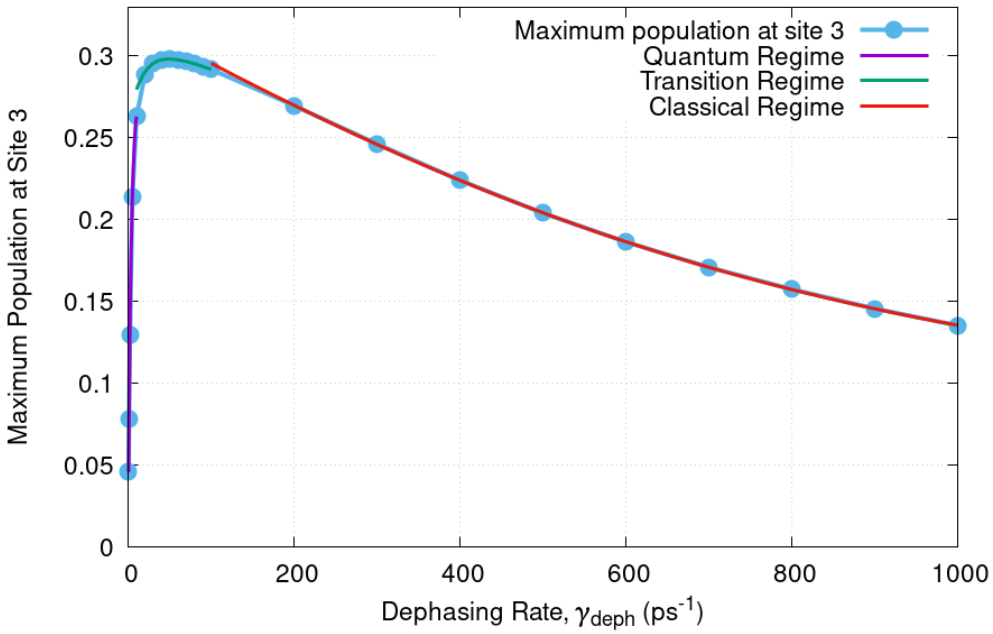

Figure 2.6: Maximum population at site 3 for the FMO-123 system versus the dephasing rate for quantum, transition, and classical regimes, respectively. We set the parameters $\gamma_{\text{inj}} = 400$ ps^{-1} and $\gamma_{\text{ext}} = 0.1$ ps^{-1}.

Three regimes can be identified:

1. The first regime ranges, between values of 0.5 ps^{-1} and 20.0 ps^{-1} in the dephasing rate, it is characterized by the presence of beating, meaning this regime exhibits coherence. Thus, it refers to the quantum regime. Here, as the dephasing increases, hence does the maximum stable value of the population at site 3. By performing a fit on this data set, we find the expression

   $$F_1(\gamma_{\text{deph}}) \approx 2 \times 10^{-6}\gamma_{\text{deph}}^5 - 8 \times 10^{-5}\gamma_{\text{deph}}^4 + 10^{-3}\gamma_{\text{deph}}^3 - 10^{-2}\gamma_{\text{deph}}^2 + 0.08\gamma_{\text{deph}} + 0.007,$$

   which displays a polynomial behavior. However, it is noticeable that a more linear behavior predominates for this first studied regime.

2. The second, given between values from 20.0 ps^{-1} to 100.0 ps^{-1} in the dephasing rate, no longer shows the quantum beat. However, it can be seen as a transition to the next regime, it could even be the ENAQT regime previously mentioned in this work in the sections 1.4 and 1.5. This is a regime in which the dependence of the quantum transport on the dephasing rate is not monotonic, since it shows a maximum for an optimal rate, as in our case [20]. Similarly, fitting the data yields the expression

   $$F_2(\gamma_{\text{deph}}) \approx 10^{-11}\gamma_{\text{deph}}^5 - 5 \times 10^{-9}\gamma_{\text{deph}}^4 + 7 \times 10^{-7}\gamma_{\text{deph}}^3 - 6 \times 10^{-5}\gamma_{\text{deph}}^2 + 0.002\gamma_{\text{deph}} + 0.3,$$

in this case, it also can be modeled as a fifth-order polynomial. But the most important characteristic of this regime is the presence of a maximum for a value of 50.0 ps^{-1} of dephasing rate. That is, the highest population reached at site 3, which in this case remains constant over time (see figure 2.5d), is maximum when this value is adjusted to this rate.

3. The third, between values from 100.0 ps^{-1} to 1000.0 ps^{-1} in the dephasing rate, is the most classical regime. By performing the fitting, we obtain

$$F_3(\gamma_{\text{deph}}) \approx 9\times10^{-18}\gamma_{\text{deph}}^5 - 5\times10^{-14}\gamma_{\text{deph}}^4 + 8\times10^{-11}\gamma_{\text{deph}}^3 + 5\times10^{-8}\gamma_{\text{deph}}^2 - 0.0003\gamma_{\text{deph}} + 0.3,$$

in this case, the polynomial behavior is much more appreciated than in the first regime, in addition to noticing how as the dephasing rate increases the maximum reached by the population at site 3 decreases, so it can be said that this regime does not favor excitonic transport towards site 3.

In general, it can be observed that there is a value of the dephasing rate at which the population at site 3 exhibits a maximum stable population value, i.e. there is successful transport from the first site to the extraction site. In addition, this maximum leads the system into a stable regime so that the transport is sustained over time. All of the above suggests that the system must have a robust efficiency value for a given dephasing rate projected in the second regime, more specifically for the value 50.0 ps^{-1}.

2.3 Efficiency in the Lindblad Formalism

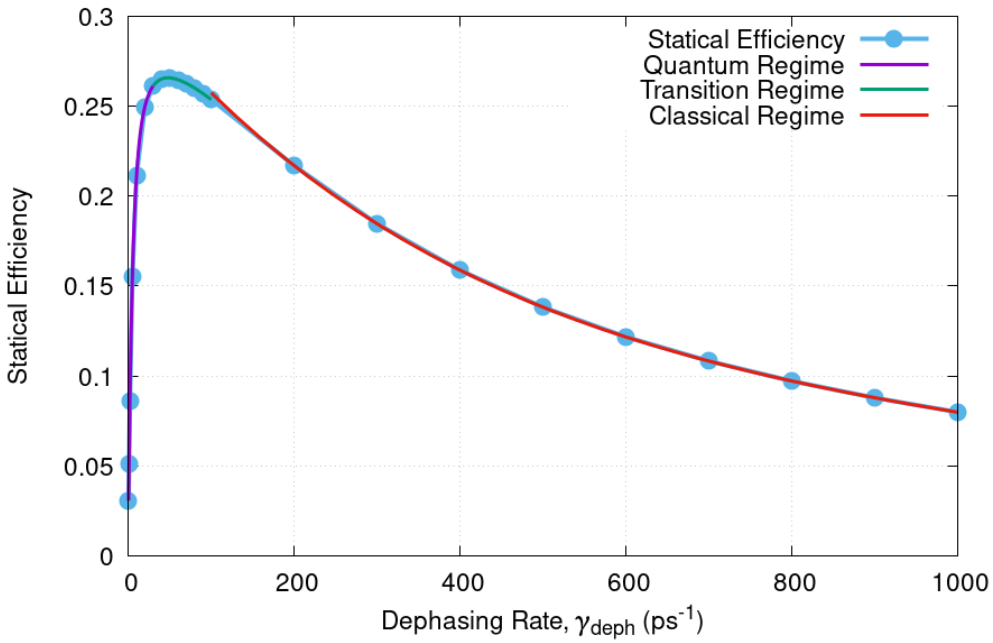

Figure 2.7: Statical Efficiency for reduced FMO-123 system regarding the dephasing rate for quantum, transition, and classical regimes, respectively. We set the parameters $\gamma_{\text{inj}} = 400$ ps^{-1} and $\gamma_{\text{ext}} = 0.1$ ps^{-1}.

As already mentioned in the introduction (see subsection 1.5.1) two possible approaches to treat efficiency inside the Lindblad formalism are considered, the Statical and Dynamical Efficiency. For the first one, the equation 1.9 is solved for the different values of the dephasing rate given in table 2.1, considering that the maximum time is 10 ps. Recalling that, this efficiency depends only on the dephasing rate parameter.

2.3.1 Statical Efficiency

Figure 2.7 shows the three previously mentioned regimes in subsection 2.2.3 with a functional form very similar to that found in figure 2.6. This implies that the maximum value of the population for each value of the dephasing rate is decisive for the definition of efficiency. For the same reason, there is a maximum associated with an optimal dephasing rate belonging to the transition regime; this value is found to be $\gamma_{\text{deph}} = 50.0\ ps^{-1}$. It is also possible to retrieve functional forms for the Statical Efficiency in terms of the dephasing rate that governs each of the regimes:

1. The quantum regime: by performing a fit on this data set we find the following fitting expression,
$$\bar{\eta}_{s,1}(\gamma_{\text{deph}}) \approx -4.3 \cdot \left(\frac{\gamma_{\text{deph}}}{8.2} + 2.3\right)^{-3.4} + 0.3,$$
which describes a different behavior the one that seen in the first regime of the figure 2.6, which was polynomial. Here it is an algebraic function with a negative exponent, however, it is observed how the value of the function increases as the dephasing rate increases.

2. The transition regime, as before, is modeled as a fifth-order polynomial. Fitting the data yields to,
$$\bar{\eta}_{s,2}(\gamma_{\text{deph}}) \approx 2 \times 10^{-11}\gamma_{\text{deph}}^5 - 8 \times 10^{-9}\gamma_{\text{deph}}^4 + 10^{-6}\gamma_{\text{deph}}^3 - 10^{-4}\gamma_{\text{deph}}^2 + 0.004\gamma_{\text{deph}} + 0.2,$$
as expected, in this regime we find the maximum efficiency of the reduced system FMO-123, which correctly agrees with what was observed in the previous section.

3. The classical regime is also polynomial behavior, such that,
$$\bar{\eta}_{s,3}(\gamma_{\text{deph}}) \approx -10^{-17}\gamma_{\text{deph}}^5 + 10^{-13}\gamma_{\text{deph}}^4 - 4 \times 10^{-10}\gamma_{\text{deph}}^3 + 6 \times 10^{-7}\gamma_{\text{deph}}^2 - 6 \times 10^{-4}\gamma_{\text{deph}} + 0.3,$$
once again, it can be seen how in this regime efficiency decreases with the growth of the dephasing rate.

2.3.2 Dynamical Efficiency

Note that the previous representation does not consider the change in the system input (site 1), which could be affecting efficiency performance since, even at its maximum value, efficiency does not exceed 30%. This motivates us to take this factor into account in the following definition of efficiency. Figure 2.8 was generated using equation 1.13 for the Dynamical Efficiency. For this analysis, we considered the dynamics at site 1 as the entry point. This new graph is nearly identical to the previous one, but it achieves higher efficiency values, with a maximum yield of approximately 75%. Again, the functional forms per regime have been calculated.

1. The quantum regime, we recover the polynomial behavior for this regime,
$$\bar{\eta}_{d,1}(\gamma_{\text{deph}}) \approx -4 \times 10^{-7}\gamma_{\text{deph}}^5 + 10^{-5}\gamma_{\text{deph}}^4 + 9 \times 10^{-5}\gamma_{\text{deph}}^3 - 0.006\gamma_{\text{deph}}^2 + 0.1\gamma_{\text{deph}} + 0.01.$$

2. The transition regime, the maximum efficiency is found for the same value of 50.0 ps^{-1} of the dephasing rate,

$$\bar{\eta}_{d,2}(\gamma_{\text{deph}}) \approx 8\times10^{-11}\gamma_{\text{deph}}^5 - 3\times10^{-8}\gamma_{\text{deph}}^4 + 5\times10^{-6}\gamma_{\text{deph}}^3 - 4\times10^{-4}\gamma_{\text{deph}}^2 + 0.02\gamma_{\text{deph}} + 0.5.$$

3. The classical regime, the decreasing behavior typical of this regime continues,

$$\bar{\eta}_{d,3}(\gamma_{\text{deph}}) \approx -8\times10^{-17}\gamma_{\text{deph}}^5 + 6\times10^{-13}\gamma_{\text{deph}}^4 - 2\times10^{-9}\gamma_{\text{deph}}^3 + 3\times10^{-6}\gamma_{\text{deph}}^2 - 0.002\gamma_{\text{deph}} + 0.8.$$

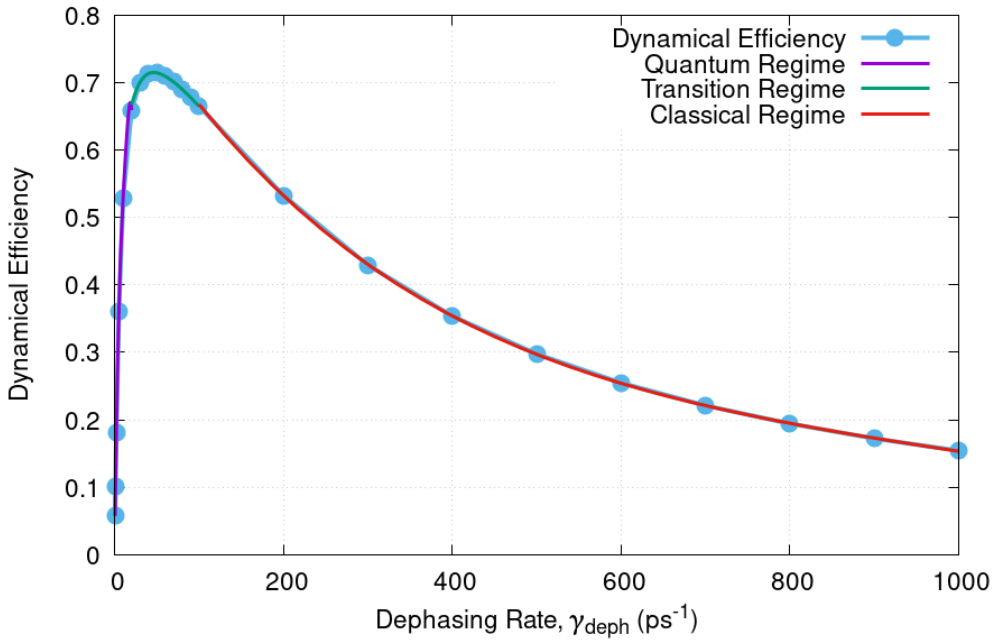

Figure 2.8: Dynamical Efficiency for reduced FMO-123 system regarding the dephasing rate for quantum, transition, and classical regimes, respectively. We set the parameters $\gamma_{\text{inj}} = 400$ ps^{-1} and $\gamma_{\text{ext}} = 0.1$ ps^{-1}.

One of the most important aspects of this analysis is the transition regime of the FMO-123 system, which records the greatest increase in efficiency. Based on the results presented in figures 2.7 and 2.8, it can be concluded that the maximum efficiency achieved for the given parameters and time scale is found in a dephasing rate equal to 50.0 ps^{-1}. This value falls within the transition regime previously referred to as the ENAQT regime (see sections 1.4 and 1.5). Furthermore, it is evident from figure 2.8 that there is a difference between considering the input power as unity, as in the Statical Efficiency (see equation 1.9), and considering this power as the probability of eviction of the excitons in chromophore 1 for a maximum time, as in the Dynamical Efficiency (see equation 1.13). The latter accounts for the system's dynamics by considering both its input and output. This generates a more complete understanding of its behavior, allowing us to establish a more accurate maximum efficiency value while maintaining the same functional behavior as in the first case. Therefore, it is one of the most important results of this work.

According to Lewis A. Baker and Scott Habershon in Ref.[4], for the complete FMO system, an increase in the population at site 3 is reported in the first 3 ps, in which case the quantum

beat is maintained only during the first 0.5 *ps*. This initial similarity allows us to relate the results obtained to previous information, even if we consider the reduced system since the initial excitation is in the first chromophore. Specifically, in terms of efficiency, which in this case is more consistent with the form exposed in the equation 1.9, it is shown that for a complete system of 7 chromophores and an initial excitation at site 1, maximum efficiency is obtained in the transition regime. This is a common denominator that is also mentioned by Patrick Rebentrost, et al. in Ref.[46] and by Elinor Zerah-Harush and Yonatan Dubi in Ref.[62]. The latter analyzes how the shape of the efficiency changes depending on the organization of the chromophores. Therefore, they conclude that symmetry is a very important phenomenon to take into account in terms of maximum efficiency since when evaluating asymmetric systems they are those that show maximum efficiency, which is consistent with our results.

However, despite all the favorable results obtained by this formalism and the fact that they are consistent with what has been reported in various references, the important limitations of the Lindblad master equation must be recognized, such as its Markovian approach and its action, which reduces only to the weak coupling limit. These two generalities are not completely fulfilled in the FMO complex, since it has been previously observed how the system has memory and how its dynamics are not separable [34]. In this sense, what we want is to use a tool that allows us to cover these new conditions to find a behavior that is more faithful to that of the FMO complex in green sulfur bacteria. This is where Green's functions come into play, a formalism that accepts larger couplings [56]. Everything related to this tool will be discussed in chapter 3. In the meantime, let us discuss the excitonic current within the Lindblad formalism since this is also very useful information to study how is the excitonic transport in the FMO-123 system.

2.4 Excitonic Current with Lindblad Formalism

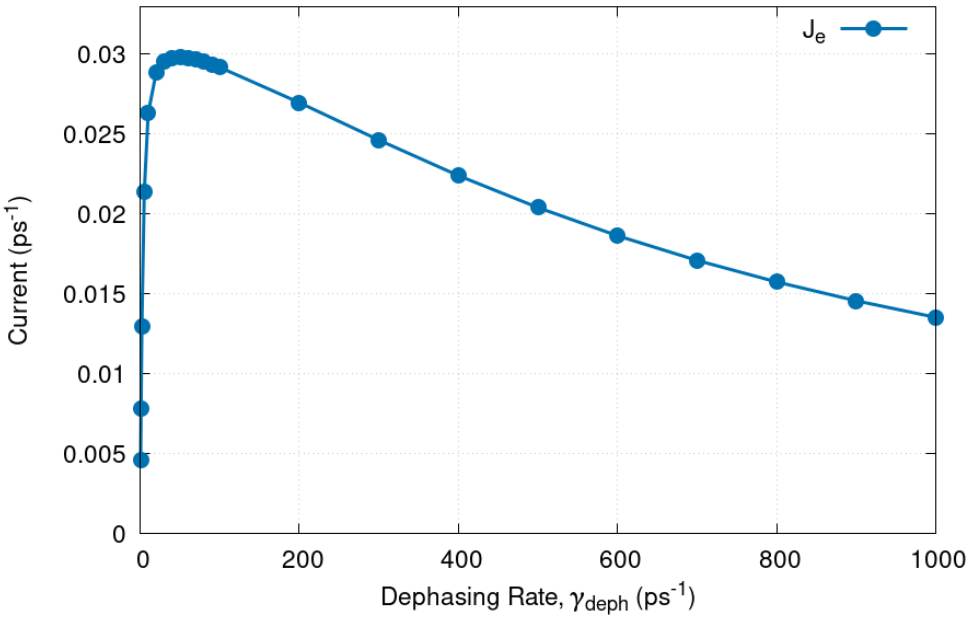

Figure 2.9: Excitonic current 1 for reduced FMO complex *123* versus the dephasing rate. We set the parameters $\gamma_{\text{inj}} = 400$ ps^{-1} and $\gamma_{\text{ext}} = 0.1$ ps^{-1}.

Another observable that is of great importance when exploring transport is the current, in this case, the excitonic current. This refers to the transfer of excitons, their collective and ordered movement through the molecules of the FMO complex. As already discussed, excitonic energy transfer is fundamental to the efficiency of the system, since it allows the energy absorbed in a region of the light spectrum to be efficiently transported to the photosynthetic reaction center, where the conversion of light energy into chemical energy takes place [1]. In Ref.[62], the concept of exciton current in the Lindblad framework is extended to demonstrate an universal origin for ENAQT in quantum networks with a phase-lag environment, based on a relationship between exciton current and occupancy. An expression is formulated for this current, which is proportional to the occupancy of the extraction site multiplied by the extraction rate,

$$J_e = \gamma_{\text{ext}} \cdot \rho_{3,3}. \tag{2.18}$$

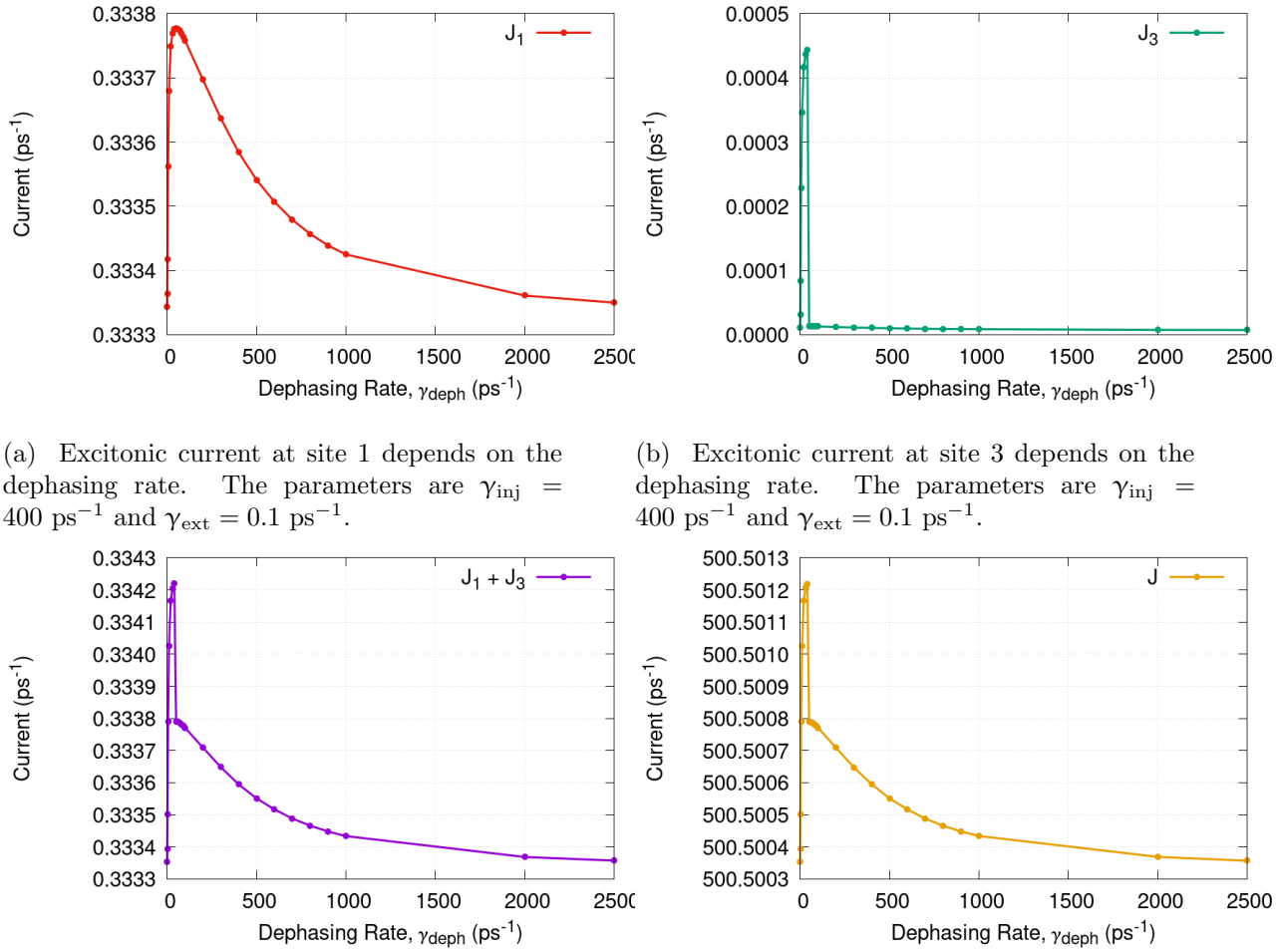

(a) Excitonic current at site 1 depends on the dephasing rate. The parameters are $\gamma_{\text{inj}} = 400\ \text{ps}^{-1}$ and $\gamma_{\text{ext}} = 0.1\ \text{ps}^{-1}$.

(b) Excitonic current at site 3 depends on the dephasing rate. The parameters are $\gamma_{\text{inj}} = 400\ \text{ps}^{-1}$ and $\gamma_{\text{ext}} = 0.1\ \text{ps}^{-1}$.

(c) Excitonic current at sites 1 and 3 depends on the dephasing rate. The parameters are $\gamma_{\text{inj}} = 400\ \text{ps}^{-1}$ and $\gamma_{\text{ext}} = 0.1\ \text{ps}^{-1}$.

(d) Excitonic current at sites 1, 2, and 3 depends on the dephasing rate. The parameters are $\gamma_{\text{inj}} = 400\ \text{ps}^{-1}$ and $\gamma_{\text{ext}} = 0.1\ \text{ps}^{-1}$.

Figure 2.10: Excitonic current 2 for reduced FMO complex *123* in sites (a) 1, (b) 3, (c) 1 and 3, (d) 1, 2, and 3.

When plotted against the dephasing rate for different molecule configurations, a strong dependence of this current on the chromophore distribution is discovered; it is also observed that it depends on

the choice of the extraction site. In a linear chain, where the extraction site is not at the end of the chain, the excitonic current is characterized by presenting a maximum in ENAQT, but it should be mentioned that all this analysis is carried out in a steady state. Considering that whatever the dephasing rate, the population at site 3 reaches a maximum value where it remains stationary, it is possible to take this value as a constant and use it to describe the current, this would be reflected in the figure 2.9, which is identical to the graph in figure 2.6 but scaled by the dephasing rate. In this case, we find an agreement between what is described by Ref.[62] and what is found in our results, since the maximum of the current is also in the intermediate regime. Regarding the values reached with the current, we can see that they are similar to those described for asymmetric distributions. Furthermore, in these examples, the maximum is also reached at values of the dephasing rate close to 50 ps^{-1}.

Beyond the equation 2.18, another way to quantify an excitonic current could be considered that does not start from taking the system in a steady state but also includes its fluctuations in time. To do this, we decided to define the excitonic current as the time average of the expected value of the derivative of the state operator divided by the maximum time,

$$J = \frac{\overline{\langle \dot{\rho}(t) \rangle}}{t_{max}} = \frac{\overline{\mathrm{Tr}[\dot{\mathscr{P}}(t)\mathscr{P}(t)]}}{t_{max}} \approx \frac{\overline{\sum_{i=0}^{3} \rho_{i,i}(t)\ \dot{\rho}_{i,i}(t)}}{t_{max}},$$

$$J \approx \sum_{i=0}^{3} J_i = \frac{1}{(t_{max})^2} \sum_{i=0}^{3} \int_0^{t_{max}} \rho_{i,i}(t)\ \dot{\rho}_{i,i}(t)\ dt \tag{2.19}$$

to obtain a weighted change in the population over time. This can be defined this way since the off-diagonal elements of the state operator matrix tend to stabilize over time, and their magnitude is appreciably smaller than the elements on the diagonal, around two orders of magnitude smaller (see figure 2.2). From this functional form, it is possible to define the current at each site of the system FMO-123, as well as sums of these currents and the total current,

$$J_{1,3} = J_1 + J_3, \tag{2.20}$$

$$J = J_1 + J_2 + J_3. \tag{2.21}$$

In this case, the excitonic current at site 2, J_2 has a constant value of 500.167 ps^{-1}, thus plotting it does not add much difference. However, observing the behavior of the currents at the entry and exit sites is extremely relevant to this study; these can be seen in figure 2.10.

On the one hand, in figure 2.10a we can see the current at the entry site, we notice again a maximum that is positioned exactly at 50 ps^{-1} of the dephasing rate, the same as the total current above and the two efficiencies presented in the section 2.3. In this sense, its behavior is as expected, it has its transport peak in the intermediate regime and then slowly decreases to end up fading at a very high dephasing rate. Figure 2.10b also shows a current maximum, but unlike the previous case, this maximum occurs before reaching 50 ps^{-1}, specifically 40 ps^{-1} of the dephasing rate; that is, just before this limit, the current increases and then suddenly decreases for the higher values, showing how the current practically disappears when the optimal value of the dephasing rate is exceeded.

Regarding the figures 2.10c and 2.10d, they are described by the equations 2.20 and 2.21, respectively; their only difference is the addition of the constant current at site 2 2.10d. This being the case, they retain the attribute of the current at site 3 since its maximum is also found at 40 ps^{-1}, but the current does not disappear but continues to manifest itself thanks to the fact that,

at the global level of the system, the input site continues to present the current even if it has faded at the output site.

Returning to both figures, both 2.9 and 2.10, we can conclude that the system is clearly establishing an ideal value of 50 ps^{-1} for the dephasing rate in the intermediate regime, being that for both cases represents a before and after in the dynamics of the system FMO-123, whether it is analyzed in its entirety (see figures 2.9, 2.10c and 2.10d) or that its behavior is separated for each chromophore (see figures 2.10a and 2.10b). This is in absolute agreement with all the previous results of this chapter, as well as with the main works cited throughout it. With all this, we are allowed to specify the value of 50 ps^{-1} of the dephasing rate of the reduced FMO-123 system, present in the ENAQT. It is expected that an analogous result can be described by Green functions, starting from a simple approach, being this the matter of chapter 3.

Chapter 3

FMO Dynamics: Green's Function Framework

Green's function formalism is an elegant and well-structured method to describe quantum dynamics during transitions between single-particle or many-particle states, for instance, with particular applications to quantum scattering and transport. Green's functions applied to condensed matter systems can describe dynamics at zero temperature, at finite temperature (equilibrium), and at non-thermal (non-equilibrium) regimes. In the context of equilibrium, it provides a complete theoretical framework for understanding how open quantum systems behave [56]. Atomic scale systems are described by discrete-level models, based on molecular orbitals, as is the case of the FMO complex. From discrete-level representations, matrix representations of Green's functions are the primary theoretical tool at the nanoscale. On the side of quantum transport problems, non-equilibrium Green's functions have been useful in describing the motion of charge, particles, spin, energy, and heat across quantum systems coupled to reservoirs, which due to their size, can be modeled in the continuum limit [27, 51].

On the other hand, about sixty years ago, the non-equilibrium Green's function (NEGF) [21, 29, 31] formalism was introduced. It can handle a wide range of physical aspects regarding quantum transport. The NEGF formalism has the advantage of treating the dynamics of quantum systems far from an equilibrium state, and though not for every quantum system non-equilibrium Green's functions yield an analytical solution, smart approximations can be derived for a given time and energy scale considered. By extending the traditional Green's function formalism to the Schwinger-Keldysh contour [31], it can handle non-equilibrium circumstances and can also systematically incorporate interaction effects like electron-electron or electron-vibron. However, the computation of these Green's functions is by no means an easy task.

3.1 Green's functions

Green's functions serve as a valuable instrument for characterizing events occurring within a system at a specific moment. To achieve this, precise knowledge of both the timing of these events and their sequence is essential. The domains in which Green's functions can effectively describe matter including:

- Green's functions at zero temperature.

- Green's functions at finite temperature.
- Non-equilibrium Green's functions.

To start, we examine the Hamiltonian that characterizes a monatomic linear chain. Second quantization provides a method for formulating the Hamiltonian concerning the events happening in the system [55]. This Hamiltonian governs the temporal behavior employing the the operators $\hat{\mathbf{d}}$ and $\hat{\mathbf{d}}^{\dagger}$:

$$\hat{H}_s = \sum_{i=1}^{N} \varepsilon_i \ \hat{\mathbf{d}}_i^{\dagger} \hat{\mathbf{d}}_i + \sum_{\substack{i \neq j \\ i,j=1}}^{N} J_{i,j} \ \hat{\mathbf{d}}_i^{\dagger} \hat{\mathbf{d}}_j. \tag{3.1}$$

3.1.1 Green's functions at zero temperature

When a Green's function is evaluated at absolute zero temperature, it is expressed in real-time and captures a comprehensive set of statical and dynamical details concerning the motion of particles within the many-body system. The Green's function at $T = 0$ is determined as follows:

$$G_{ij}\left(t, t'\right) = -\frac{i}{\hbar} \left\langle \mathcal{T} \ \hat{\mathbf{d}}_i(t) \hat{\mathbf{d}}_j^{\dagger}\left(t'\right) \right\rangle, \tag{3.2}$$

where $\mathcal{T}$ refers to the temporal ordering operator. It is important to note that Green's function described in the above example is both propagator and expectation value, which is a fundamental property of Green's functions of quantum mechanics. The behavior of the Green's function is also dependent on the Fermi function, since the temperature tends towards zero, and the value of $f(\varepsilon)$ tends to the function $\theta\left(\varepsilon_f - \varepsilon\right)$, being that ε_f denotes the Fermi energy [38].

3.1.2 Green's functions at finite temperature

Let's consider a canonical system, in contact with a reservoir at temperature T. The partition function is defined as $\mathcal{Z} = \mathrm{Tr}\left(e^{-\beta \hat{H}}\right)$, with $\beta = 1/(k_B T)$, where k_B represents the Boltzmann constant [38]. Starting from $(-i/\hbar)t = -\beta$, it comes to $t = -i\hbar\beta = -i\tau$, where τ is defined as an imaginary time associated with thermal properties [33]. Building upon this insight, Matsubara develops a theory of finite temperature Green's functions for many-body systems, often referred to as imaginary time Green's functions [40],

$$G_{ij}\left(\tau, \tau'\right) = -\frac{1}{\hbar} \left\langle \mathcal{T}_{\tau} \ \hat{\mathbf{d}}_i(\tau) \hat{\mathbf{d}}_j^{\dagger}\left(\tau'\right) \right\rangle, \tag{3.3}$$

the operators $\hat{\mathbf{d}}_i(\tau)$ and $\hat{\mathbf{d}}_j^{\dagger}(\tau')$ are Grassmann operators evaluated at imaginary time [33]. It is important to note that the periodicity of Green's functions at finite temperature is related to the statistics of the number of particles to which they pertain,

$$G(\tau \pm \hbar\beta) = \pm G(\tau), \tag{3.4}$$

where the symbol (+) corresponds to bosonic statistics, while the symbol (-) with fermionic statistics. The thermodynamic states of the physical system are visually represented on the Matsubara contour, which is an imaginary time path with a period of $\hbar\beta$.

3.1.3 Nonequilibrium Green's functions

Schwinger introduced nonequilibrium Green's functions, which Kadanoff, Baym, and Keldysh further developed in parallel. This formalism has been widely used to study the dynamics of nonequilibrium systems and to derive quantum transport models, amongst other applications. Nonequilibrium Green's functions are an extension of Green's at finite temperature formalism by Matsubara, and their utility extends to equilibrium models as well [5]. Specifically, this approach relies on two key theories for constructing out-of-equilibrium Green's functions: the Kadanoff-Baym and the Keldysh-Schwinger formalism.

The Kadanoff-Baym theory employs an imaginary time contour that commences at $\tau = 0$ and concludes at $\tau = -i\hbar\beta$. Within this contour, the Kadanoff-Baym branches denoted as γ_+ and γ_-, correspond to the forward and backward trajectories in time, respectively [51]. In contrast, according to Keldysh and Schwinger's theory, real-time contours are used. Events within γ_+ refer to ordered occurrences along the real-time curve, while events within γ_- refer to the irreversibility of disordered events along the regressive contour. Since the operator dynamics evaluation is done in real-time, as shown in the above equation 3.5, we can define a nonequilibrium Green's function as follows:

$$G_{ij}^{\alpha\beta}\left(t,t'\right) = -\frac{i}{\hbar}\left\langle \mathcal{T}_\tau\ \hat{\mathbf{d}}_i\left(t_\alpha\right)\hat{\mathbf{d}}_j^\dagger\left(t'_\beta\right)\right\rangle, \tag{3.5}$$

where α and β denote the specific contour in which events take place. $G^{\alpha\beta}\left(t,t'\right)$ represents a matrix within the Keldysh contour [31].

When particle creation and destruction events occur within the progressive contour, the organized Green's function within the contour takes the following structure:

$$G_{ij}^{C}\left(t,t'\right) = -\frac{i}{\hbar}\left\langle \mathcal{T}_\tau\ \hat{\mathbf{d}}_i\left(t_+\right)\hat{\mathbf{d}}_j^\dagger\left(t'_+\right)\right\rangle. \tag{3.6}$$

However, if the events are situated within the regressive contour, the anti-ordered Green's function within the contour is:

$$G_{ij}^{\bar{C}}\left(t,t'\right) = -\frac{i}{\hbar}\left\langle \overline{\mathcal{T}}_\tau\ \hat{\mathbf{d}}_i\left(t_-\right)\hat{\mathbf{d}}_j^\dagger\left(t'_-\right)\right\rangle, \tag{3.7}$$

where $\overline{\mathcal{T}}_\tau$ represents the anti-time-ordered operator. In the $\gamma+$ and $\gamma-$ contours, events occurring at later time points are positioned near $+\infty$ and $-\infty$, respectively [31].

In a specific scenario, such as when the creation event occurs in the regressive contour and the destruction event occurs in the progressive contour, the Green's function takes on the following form:

$$G_{ij}^{>}\left(t,t'\right) = -\frac{i}{\hbar}\left\langle \hat{\mathbf{d}}_i\left(t_+\right)\hat{\mathbf{d}}_j^\dagger\left(t'_-\right)\right\rangle. \tag{3.8}$$

If we consider the opposite case, we have:

$$G_{ij}^{<}\left(t,t'\right) = \frac{i}{\hbar}\left\langle \hat{\mathbf{d}}_j^\dagger\left(t'_-\right)\hat{\mathbf{d}}_i\left(t_+\right)\right\rangle, \tag{3.9}$$

where the Green's functions defined in equations 3.8 and 3.9 can be seen as correlations between the two contours [31]. Then, the nonequilibrium Green's function on the Keldysh contour is given by:

$$G\left(t,t'\right) = \begin{pmatrix} G_{ij}^{C}\left(t_+,t'_+\right) & G_{ij}^{>}\left(t_+,t'_-\right) \\ G_{ij}^{<}\left(t_-,t'_+\right) & G_{ij}^{\bar{C}}\left(t_-,t'_-\right) \end{pmatrix}. \tag{3.10}$$

3.2 Retarded and Advanced Green's Functions

Green's functions are well-known to be a useful tool for solving linear differential equations, such as Schrödinger's equation in the context of quantum mechanics. Furthermore, the formalism of Green's function is well-accepted for molecular-level discrete systems, and can easily be extended to cover many-body effects. Let's begin with the formal general definition of Green's functions retarded and advanced guiding us with chapter 4 of Ref.[56].

3.2.1 Green's Functions in Classical Regime

In the classical regime, in the context of electrodynamics, the problem of linear non-homogeneous differential equations becomes a vectorial wave equation (or a scalar wave equation if we consider it in component form) given by:

$$\nabla^2\Psi(\mathbf{r},t) - \frac{1}{c^2}\frac{\partial^2\Psi(\mathbf{r},t)}{\partial t^2} = F(\mathbf{r},t), \tag{3.11}$$

we can write the solution of the wave equation $\Psi(\mathbf{r},t)$ as a convolution integral,

$$\Psi(\mathbf{r},t) = \int dt' \int d^3\mathbf{r}'\ G(\mathbf{r}-\mathbf{r}', t-t')\ F(\mathbf{r},t), \tag{3.12}$$

where $G(\mathbf{r}-\mathbf{r}', t-t')$ is known as the Green's function.

In the Fourier domain, we can derive the spectral representation of the Green's function which turns out as,

$$G(\mathbf{k},\omega) = \frac{c^2}{(\omega-ck)(\omega+ck)}, \quad \omega_1 = ck, \quad \omega_2 = -ck, \tag{3.13}$$

with poles ω_1 and ω_2. To write the solution for the wave equation as a convolution integral, we require the Green's function in the real spatio-temporal domain. Then, we derive the inverse Fourier transform of the above expression,

$$G(\mathbf{r},\tau) = \oint_\gamma \frac{d\omega}{2\pi} e^{i\omega\tau} \int \frac{d^3\mathbf{k}}{(2\pi)^3}\ G(\mathbf{k},\omega) e^{-i\mathbf{k}\cdot\mathbf{r}}. \tag{3.14}$$

As a requirement for a causal response, the poles must lie on the semi-lower complex plane, and for an anti-causal response, the poles must lie on the semi-upper complex plane. Therefore, we perform analytical continuation as follows to guarantee causal and anti-causal responses:

$$G(\mathbf{k},\omega\to\omega\pm i\eta) = \frac{c^2}{(\omega-ck\pm i\eta)(\omega+ck\pm i\eta)} = G^{\mp}(\mathbf{k},\omega) = G^{R/A}(\mathbf{k},\omega), \tag{3.15}$$

hence, the Retarded and Advanced Green's functions are given by:

$$G^R(\mathbf{k},\omega) = \frac{c^2}{(\omega-ck+i\eta)(\omega+ck+i\eta)}, \quad \bar\omega_1 = ck-i\eta, \quad \bar\omega_2 = -ck-i\eta, \tag{3.16}$$

$$G^A(\mathbf{k},\omega) = \frac{c^2}{(\omega-ck-i\eta)(\omega+ck-i\eta)}, \quad \bar\omega_1 = ck+i\eta, \quad \bar\omega_2 = -ck+i\eta, \tag{3.17}$$

where the new poles after analytical continuation are $\bar\omega_1$ and $\bar\omega_2$. For the specific interest that underlies the present work, we consider only the Retarded propagator:

$$G^R(\mathbf{R},\tau) = c^2 \int \frac{d^3\mathbf{k}}{(2\pi)^3} e^{-i\mathbf{k}\cdot\mathbf{R}} \oint_{\gamma_-} \frac{d\omega}{2\pi} e^{i\omega\tau} \frac{1}{(\omega-ck+i\eta)(\omega+ck+i\eta)}. \tag{3.18}$$

3.2.2 Green's Functions in Quantum Regime

An important question regarding quantum evolution is, does the formal structure of quantum dynamics support the use of Green's functions? Is there any counterpart to the retarded Green's function for quantum evolution? Is there any way to capture the essence of an observable from the knowledge of retarded Green's functions in the quantum realm? These questions will guide our discussion for the next paragraphs. Now, let's consider the arbitrary state of a physical system $|\psi\rangle$:

$$|\psi\rangle = \hat{I}\ |\psi\rangle = \int d^3\mathbf{r}'|\mathbf{r}'\rangle\langle\mathbf{r}'|\psi\rangle, \tag{3.19}$$

now, let's consider the time evolution of a quantum state,

$$|\psi, t\rangle = \mathcal{U}(t, t')|\psi, t'\rangle, \tag{3.20}$$

here, we will project this state onto the eigenbasis of the position operator,

$$\langle\mathbf{r}|\psi, t\rangle = \langle\mathbf{r}|\mathcal{U}(t, t')|\psi, t'\rangle = \langle\mathbf{r}|\hat{I}\ \mathcal{U}(t, t')|\psi, t'\rangle = \int d^3\mathbf{r}'\langle\mathbf{r}|\mathcal{U}(t, t')|\mathbf{r}'\rangle\langle\mathbf{r}'|\psi, t'\rangle. \tag{3.21}$$

If there exists a function $G(\mathbf{r}, t; \mathbf{r}', t')$ such that,

$$\langle\mathbf{r}|\mathcal{U}(t, t')|\mathbf{r}'\rangle = \int dt' G(\mathbf{r}, t; \mathbf{r}', t'), \tag{3.22}$$

Thus:

$$\psi(\mathbf{r}, t) = \int d^3\mathbf{r}' \int dt' G(\mathbf{r}, t; \mathbf{r}', t')\psi(\mathbf{r}', t'). \tag{3.23}$$

In quantum theory, the retarded and advanced Green's functions for fermions are given by:

$$G^R_{mn}(t, t') = -\frac{i}{\hbar}\theta(t - t')\langle\Big\{\mathbf{c}_m(t), \mathbf{c}^\dagger_n(t')\Big\}\rangle, \quad G^A_{mn}(t, t') = +\frac{i}{\hbar}\theta(t' - t)\langle\Big\{\mathbf{c}_m(t), \mathbf{c}^\dagger_n(t')\Big\}\rangle, \tag{3.24}$$

and for bosons:

$$G^R_{mn}(t, t') = -\frac{i}{\hbar}\theta(t - t')\langle\Big[\mathbf{a}_m(t), \mathbf{a}^\dagger_n(t')\Big]\rangle, \quad G^A_{mn}(t, t') = +\frac{i}{\hbar}\theta(t' - t)\langle\Big[\mathbf{a}_m(t), \mathbf{a}^\dagger_n(t')\Big]\rangle. \tag{3.25}$$

On the other hand, the step function can be represented as follows,

$$\theta(t - t') = -\frac{1}{2\pi i}\oint d\omega \frac{e^{-i\omega(t-t')}}{\omega + i\eta}, \tag{3.26}$$

by knowing that,

$$\mathbf{A}(t) = e^{\frac{i}{\hbar}\hat{H}(t-t')}\mathbf{A}(t')e^{-\frac{i}{\hbar}\hat{H}(t-t')}, \tag{3.27}$$

we can rewrite the retarded Green's function,

$$\begin{aligned} G^R_{ij}(t, t') &= -\frac{i}{\hbar}\theta(t - t')\langle\Big[\mathbf{d}_i(t), \mathbf{d}^\dagger_j(t')\Big]_\pm\rangle = -\frac{i}{\hbar}\theta(t - t')\langle\mathbf{d}_i(t)\mathbf{d}^\dagger_j(t') \pm \mathbf{d}^\dagger_j(t')\mathbf{d}_i(t)\rangle, \\ &= -\frac{i}{\hbar}\theta(t - t')\langle e^{\frac{i}{\hbar}\hat{H}(t-t')}\mathbf{d}_i(t')e^{-\frac{i}{\hbar}\hat{H}(t-t')}\mathbf{d}^\dagger_j(t') \pm \mathbf{d}^\dagger_j(t')e^{\frac{i}{\hbar}\hat{H}(t-t')}\mathbf{d}_i(t')e^{-\frac{i}{\hbar}\hat{H}(t-t')}\rangle. \end{aligned} \tag{3.28}$$

3.2.3 Density of States

The density of states (DOS) refers to the number of states per unit frequency range of a system and it can be represented mathematically as a continuous distribution using a probability density function. It is usually an average of the number of states occupied by a system over its space and time domains. It is directly associated with the dispersion relationships of the system's properties. A high DOS at a given energy level indicates that a large number of states are available to be occupied. In other words, the DOS of the quantum system quantifies how densely the particles in the quantum mechanical system are packed in terms of energy levels. It can be as low as zero, meaning that the particles do not occupy the energy level, and as high as a defined occupation value, at a specific energy level that is accessible to the particles [10]. Now, let's derive a generalization of the concept of density of states from the perspective of the Retarded Green's Function of a many-particle state, assuming that diagonalization is possible.

$$\int_{-\infty}^{+\infty} A(\omega)\frac{d\omega}{2\pi} = 1, \quad \text{where} \quad A(\omega) = -\frac{1}{\pi}\Im m\left[G^R(\omega)\right], \tag{3.29}$$

we are interested in Green's function at finite temperatures and real times, then we use the thermal expectation value:

$$\langle \mathbf{A}(t)\rangle = \frac{1}{\mathcal{Z}(\beta)} Tr\left[e^{-\beta\hat{H}}\mathbf{A}\right] = \frac{1}{\mathcal{Z}(\beta)}\sum_m \langle m|e^{-\beta\hat{H}}\mathbf{A}|m\rangle, \tag{3.30}$$

and, if $|m\rangle$ is an eigenstate of the Hamiltonian $\hat{H}$, then:

$$\mathbf{H}|m\rangle = \mathcal{E}_m|m\rangle, \tag{3.31}$$

and considering the resolution of identity in the fock space,

$$\hat{I} = \sum_m |m\rangle\langle m|, \tag{3.32}$$

we can elaborate furthermore:

$$\begin{aligned}
G^R_{mn}(t,t') &= -\frac{i}{\hbar\mathcal{Z}(\beta)}\theta(t-t')\sum_m e^{-\beta\mathcal{E}_m}\langle m|\left(e^{\frac{i}{\hbar}\mathbf{H}(t-t')}\mathbf{d}_i(t')\sum_n |n\rangle\langle n|e^{-\frac{i}{\hbar}\mathbf{H}(t-t')}\mathbf{d}^\dagger_j(t')\pm\right.\\
&\left.\mathbf{d}^\dagger_j(t')\sum_n |n\rangle\langle n|e^{\frac{i}{\hbar}\mathbf{H}(t-t')}\mathbf{d}_i(t')e^{-\frac{i}{\hbar}\mathbf{H}(t-t')}\right)|m\rangle\\
&= -\frac{i}{\hbar\mathcal{Z}(\beta)}\theta(t-t')\sum_m\sum_n e^{-\beta\mathcal{E}_m}\langle m|\left(e^{\frac{i}{\hbar}\mathcal{E}_m(t-t')}\mathbf{d}_i(t')|n\rangle\langle n|e^{-\frac{i}{\hbar}\mathcal{E}_n(t-t')}\mathbf{d}^\dagger_j(t')\pm\right.\\
&\left.\mathbf{d}^\dagger_j(t')|n\rangle\langle n|e^{\frac{i}{\hbar}\mathcal{E}_n(t-t')}\mathbf{d}_i(t')e^{-\frac{i}{\hbar}\mathcal{E}_m(t-t')}\right)|m\rangle\\
&= -\frac{i}{\hbar\mathcal{Z}(\beta)}\theta(t-t')\left(\sum_{mn} e^{\frac{i}{\hbar}(\mathcal{E}_m-\mathcal{E}_n)(t-t')}\langle m|\mathbf{d}_i(t')|n\rangle\langle n|\mathbf{d}^\dagger_j(t')|m\rangle e^{-\beta\mathcal{E}_m}\pm\right.\\
&\left.\sum_{mn} e^{-\beta\mathcal{E}_m}\langle m|\mathbf{d}^\dagger_j(t')|n\rangle\langle n|\mathbf{d}_i(t')|m\rangle e^{-\frac{i}{\hbar}(\mathcal{E}_m-\mathcal{E}_n)(t-t')}\right).
\end{aligned}$$

In the previous equation, in the second summation we can permute indices m and n as they are dummy indices, therefore, we may write the retarded Green's function as follows:

$$\begin{aligned}
G^R_{mn}(t,t') &= -\frac{i}{\hbar\mathcal{Z}(\beta)}\theta(t-t')\left(\sum_{mn} e^{\frac{i}{\hbar}(\mathcal{E}_m-\mathcal{E}_n)(t-t')}\langle m|\mathbf{d}_i(t')|n\rangle\langle n|\mathbf{d}^\dagger_j(t')|m\rangle e^{-\beta\mathcal{E}_m}\pm\right.\\
&\left.\sum_{mn} e^{-\beta\mathcal{E}_n}\langle n|\mathbf{d}^\dagger_j(t')|m\rangle\langle m|\mathbf{d}_i(t')|n\rangle e^{\frac{i}{\hbar}(\mathcal{E}_m-\mathcal{E}_n)(t-t')}\right)\\
&= -\frac{i}{\hbar\mathcal{Z}(\beta)}\theta(t-t')\sum_{mn} e^{\frac{i}{\hbar}(\mathcal{E}_m-\mathcal{E}_n)(t-t')}\left(e^{-\beta\mathcal{E}_m}\pm e^{-\beta\mathcal{E}_n}\right)\langle m|\mathbf{d}_i(t')|n\rangle\langle n|\mathbf{d}^\dagger_j(t')|m\rangle\\
&= -\frac{i}{\hbar}\theta(t-t')\sum_{mn} e^{\frac{i}{\hbar}(\mathcal{E}_m-\mathcal{E}_n)(t-t')}\left(\frac{e^{-\beta\mathcal{E}_m}}{\mathcal{Z}(\beta)}\pm\frac{e^{-\beta\mathcal{E}_n}}{\mathcal{Z}(\beta)}\right)\langle m|\mathbf{d}_i(t')|n\rangle\langle n|\mathbf{d}^\dagger_j(t')|m\rangle\\
&= -\frac{i}{\hbar}\theta(t-t')\sum_{mn} e^{\frac{i}{\hbar}(\mathcal{E}_m-\mathcal{E}_n)(t-t')}\left(\rho_m\pm\rho_n\right)\langle m|\mathbf{d}_i(t')|n\rangle\langle n|\mathbf{d}^\dagger_j(t')|m\rangle,
\end{aligned}$$

where ρ_m and ρ_n are the thermal ocuppations of states with eigenenergies $\mathcal{E}_m$ and $\mathcal{E}_n$ respectively. Now, let's consider the spectral representation of the step function:

$$\theta(t-t') = -\frac{1}{2\pi i}\lim_{\eta\to 0}\oint_\gamma \frac{e^{-i\omega(t-t')}}{\omega+i\eta}d\omega, \tag{3.33}$$

and the retarded Green's function now reads:

$$\begin{aligned}
G^R_{mn}(t,t') &= -\frac{i}{\hbar}\left(-\frac{1}{2\pi i}\right)\lim_{\eta\to 0}\oint_\gamma \frac{e^{-i\omega(t-t')}}{\omega+i\eta}d\omega\sum_{mn} e^{\frac{i}{\hbar}(\mathcal{E}_m-\mathcal{E}_n)(t-t')}\left(\rho_m\pm\rho_n\right)\langle m|\mathbf{d}_i(t')|n\rangle\langle n|\mathbf{d}^\dagger_j(t')|m\rangle\\
&= \lim_{\eta\to 0}\oint_\gamma \frac{e^{-i\omega(t-t')}}{\hbar\omega+i\eta}\frac{d\omega}{2\pi}\sum_{mn} e^{\frac{i}{\hbar}(\mathcal{E}_m-\mathcal{E}_n)(t-t')}\left(\rho_m\pm\rho_n\right)\langle m|\mathbf{d}_i(t')|n\rangle\langle n|\mathbf{d}^\dagger_j(t')|m\rangle\\
&= \lim_{\eta\to 0}\oint_\gamma \sum_{mn}\frac{e^{-i\omega(t-t')}e^{\frac{i}{\hbar}(\mathcal{E}_m-\mathcal{E}_n)(t-t')}\left(\rho_m\pm\rho_n\right)\langle m|\mathbf{d}_i(t')|n\rangle\langle n|\mathbf{d}^\dagger_j(t')|m\rangle}{\hbar\omega+i\eta}\frac{d\omega}{2\pi}\\
&= \lim_{\eta\to 0}\oint_\gamma \sum_{mn}\frac{e^{-\frac{i}{\hbar}(\hbar\omega-\mathcal{E}_m+\mathcal{E}_n)(t-t')}\left(\rho_m\pm\rho_n\right)\langle m|\mathbf{d}_i(t')|n\rangle\langle n|\mathbf{d}^\dagger_j(t')|m\rangle}{\hbar\omega+i\eta}\frac{d\omega}{2\pi}.
\end{aligned}$$

Now, if we perform the following change of variable $\hbar\omega-\mathcal{E}_m+\mathcal{E}_n\to\hbar\omega$, the retarded Green's function reads $G^R_{mn}(t,t')$:

$$G^R_{mn}(t,t') = \lim_{\eta\to 0}\oint_\gamma \sum_{mn}\frac{\left(\rho_m\pm\rho_n\right)\langle m|\mathbf{d}_i(t')|n\rangle\langle n|\mathbf{d}^\dagger_j(t')|m\rangle}{\hbar\omega+\mathcal{E}_m-\mathcal{E}_n+i\eta}e^{-i\omega(t-t')}\frac{d\omega}{2\pi}, \tag{3.34}$$

do note from the previous expression that the only way in which we can guarantee the translational invariance on the Retarded Green's function is by making $t'=0$, hence, the operators $\mathbf{d}_i$ and $\mathbf{d}^\dagger_j$, become time-invariant, then:

$$G^R_{mn}(t,t') = \lim_{\eta\to 0}\oint_\gamma \sum_{mn}\frac{\left(\rho_m\pm\rho_n\right)\langle m|\mathbf{d}_i|n\rangle\langle n|\mathbf{d}^\dagger_j|m\rangle}{\hbar\omega+\mathcal{E}_m-\mathcal{E}_n+i\eta}e^{-i\omega(t-t')}\frac{d\omega}{2\pi} = \oint_\gamma G^R_{ij}(\omega)e^{-i\omega(t-t')}\frac{d\omega}{2\pi}, \tag{3.35}$$

from where we obtain the following representation of $G^R_{ij}(\omega)$

$$G^R_{ij}(\omega) = \sum_{mn} \frac{(\rho_m \pm \rho_n)\,\langle m|\mathbf{d}_i|n\rangle\langle n|\mathbf{d}_j^\dagger|m\rangle}{\hbar\omega + \mathcal{E}_m - \mathcal{E}_n + i\eta}. \tag{3.36}$$

From now on, do note that the diagonal matrix elements of $\mathbf{G}^R(\omega)$ are then given by:

$$G^R_{ii}(\omega) = \sum_{mn} \frac{(\rho_m \pm \rho_n)\,\langle m|\mathbf{d}_i|n\rangle\langle n|\mathbf{d}_i^\dagger|m\rangle}{\hbar\omega + \mathcal{E}_m - \mathcal{E}_n + i\eta} = \sum_{mn} \frac{(\rho_m \pm \rho_n)\,|\langle m|\mathbf{d}_i|n\rangle|^2}{\hbar\omega + \mathcal{E}_m - \mathcal{E}_n + i\eta}, \tag{3.37}$$

the previous representation for $G^R_{ii}(\omega)$ can be regarded as the generalization of Fermi's Golden Rule. Then, let's consider the imaginary part of the previous expression, using Cauchy's principal value:

$$\begin{aligned} \Im m\left\{G^R_{ii}(\omega)\right\} &= \sum_{mn} \Im m\left\{\frac{1}{\hbar\omega + \mathcal{E}_m - \mathcal{E}_n + i\eta}\right\}(\rho_m \pm \rho_n)\,|\langle m|\mathbf{d}_i|n\rangle|^2 \\ &= \sum_{mn} \left[-\pi\delta(\hbar\omega + \mathcal{E}_m - \mathcal{E}_n)\right](\rho_m \pm \rho_n)\,|\langle m|\mathbf{d}_i|n\rangle|^2, \end{aligned} \tag{3.38}$$

we may define a quantity $A_i(\omega)$, such that:

$$A_i(\omega) = -\frac{1}{\pi}\Im m\left\{G^R_{ii}(\omega)\right\} = \sum_{mn}(\rho_m \pm \rho_n)\,|\langle m|\mathbf{d}_i|n\rangle|^2\delta(\hbar\omega + \mathcal{E}_m - \mathcal{E}_n), \tag{3.39}$$

and we call $A(\omega) = \sum_i A_i(\omega)$ the density of states:

$$A(\omega) = -\frac{1}{\pi}\Im m\left\{\,Tr\left\{G^R_{ii}(\omega)\right\}\right\} = \sum_i\sum_{mn}(\rho_m \pm \rho_n)\,|\langle m|\mathbf{d}_i|n\rangle|^2\delta(\hbar\omega + \mathcal{E}_m - \mathcal{E}_n), \tag{3.40}$$

which is a positive definite quantity.

3.2.4 Matrix Elements for the Density Operator in Equilibrium

The normalization property of the density of states can be written as follows:

$$\int_{-\infty}^{+\infty} A(\omega)d\omega = 1, \tag{3.41}$$

therefore, as the trace of the state operator is unity, the trace of the matrix $-\frac{1}{\pi}\Im m\left\{G^R(\omega)\right\}$ is unity. Here, we define the matrix elements of the density operator as:

$$\rho_{ij} = -\frac{1}{\pi}\Im m\left\{G^R(\omega)\right\} = -\frac{1}{\pi}\sum_{mn}\frac{(\rho_m \pm \rho_n)\,\langle m|\mathbf{d}_i|n\rangle\langle n|\mathbf{d}_j^\dagger|m\rangle}{\hbar\omega + \mathcal{E}_m - \mathcal{E}_n + i\eta}. \tag{3.42}$$

It is also possible to define the matrix elements of the density operator in terms of the non-equilibrium Green's functions $G^>(\omega)$ and $G^<(\omega)$.

3.3 Self-energy

The solution of quantum system problems, formulated by a matrix Hamiltonian, can be solved along the standard path of finding wavefunctions on a lattice and solving Schrödinger's equation. However, matrix Green's functions were found to be more suitable for transport calculations, particularly when interactions are involved [51]. The retarded matrix Green's function is:

$$\boldsymbol{G}^R(E) = \begin{pmatrix} G_{11} & G_{12} & \cdots & G_{1N} \\ G_{21} & G_{22} & \cdots & G_{2N} \\ \vdots & \vdots & \ddots & \vdots \\ G_{N1} & G_{N2} & \cdots & G_{NN} \end{pmatrix}, \tag{3.43}$$

when each element is determined by the equation 3.43. All general properties of Green's functions, discussed above, are also applicable to the matrix Green's function [51].

The retarded Green's function in the energy domain of a system coupled to the leads is determined by,

$$\boldsymbol{G}^R(E) = \left[\boldsymbol{E} - \boldsymbol{H}_s - \boldsymbol{\Sigma}^R(E)\right]^{-1}, \tag{3.44}$$

here the effects of the contacts are included by the self-energy [51]. This can be determined just by the coupling Hamiltonians $\boldsymbol{V}_{\alpha s},\ \alpha = L, R$ and the retarded Green's functions of the isolated contacts $G^R_\alpha,\ \alpha = L, R$ [51]. If the coupling Hamiltonians are real the self-energy takes the form,

$$\Sigma^R_{ij}(E) = \sum_\alpha \frac{V_{\alpha i}V_{\alpha j}}{E - \varepsilon_\alpha + i\eta} \rightarrow \mathrm{Im}\left\{\Sigma^R_{ij}(E)\right\} = \sum_\alpha V_{\alpha i}V_{\alpha j}\,\mathrm{Im}\left\{\frac{1}{E - \varepsilon_\alpha + i\eta}\right\}, \tag{3.45}$$

using the relation $\frac{1}{x \pm i\eta} = P\left(\frac{1}{x}\right) \mp i\pi\delta(x)$, where P stands for the principal value in the case of integration, we find:

$$\mathrm{Im}\left\{\Sigma^R_{ij}(E)\right\} = \sum_\alpha V_{\alpha i}V_{\alpha j}\,\mathrm{Im}\left\{P\left(\frac{1}{E - \varepsilon_\alpha}\right) - i\pi\delta(E - \varepsilon_\alpha)\right\} = \frac{-1}{2}\underbrace{\left(2\pi\sum_\alpha V_{\alpha i}V_{\alpha j}\delta(E - \varepsilon_\alpha)\right)}_{\Gamma_{ij}(E)},$$

such that,

$$\Sigma^R_{ij}(E) = \Lambda_{ij}(E) - i\frac{\Gamma_{ij}(E)}{2}, \tag{3.46}$$

where $\boldsymbol{\Lambda}(E)$, induces a shift of the energy levels and $\boldsymbol{\Gamma}(E)$ causes a broadening [57]. Both can be in principle complex, but we consider only the cases with real ones; we also assume that $\boldsymbol{\Gamma}(E)$ is a symmetric matrix $\Gamma_{nm} = \Gamma_{mn}$. If the couplings $V_{\alpha k}$ between the system and the reservoirs are weak $\boldsymbol{\Lambda}(E)$, and $\boldsymbol{\Gamma}(E)$ are small and the dominant contribution comes from a region around ε_n [55]. Then, we can use the wide-band limit (WBL) for both reservoirs [27].

In this limit, the coupling to the leads is energy-independent, meaning that the eigenspace of the Green's function is independent of energy as well. Hence, it is also possible to neglect the real part of the self-energy. Thus, for our system, the level-width functions are energy-independent constant couplings of the form,

$$\Sigma_{ij}^{R}(E) = -i\frac{\Gamma_{ij}}{2}. \tag{3.47}$$

3.4 Keldysh-Kadanoff Approximation

For this approximation the calculation of the lesser and greater Green's functions, $\boldsymbol{G}^{<}$ and $\boldsymbol{G}^{>}$, become relevant. To fulfill this task, it is important to keep in mind the retarded and advanced Green's functions. Although the calculation represents an important challenge from the theoretical and computational perspective, this could be addressed by Keldysh-Kadanoff approximation using $\boldsymbol{G}^{R}$ and $\boldsymbol{G}^{A}$, and the lesser and greater self-energy. Thus, the 3.2 section is a fundamental step on the path towards non-equilibrium calculations in our system. Through the Keldysh-Kadanoff approach, we aim to define the lesser and greater Green's functions, which allow calculating key observables such as the excitonic current [27].

Within the Keldysh-Kadanoff approximations the lesser and greater Green's functions are:

$$\boldsymbol{G}^{<}\left(t,t'\right) = \int d\tau \int d\tau' \boldsymbol{G}^{R}(t,\tau)\boldsymbol{\Sigma}^{<}\left(\tau,\tau'\right)\boldsymbol{G}^{A}\left(\tau',t'\right), \tag{3.48}$$

$$\boldsymbol{G}^{>}\left(t,t'\right) = \int d\tau \int d\tau' \boldsymbol{G}^{R}(t,\tau)\boldsymbol{\Sigma}^{>}\left(\tau,\tau'\right)\boldsymbol{G}^{A}\left(\tau',t'\right), \tag{3.49}$$

where $\boldsymbol{\Sigma}^{</>}\left(t,t'\right)$ denotes the self-energy, lesser or greater, which describes the relationship between the investigated system and its environment [51]. As a result, the characteristic scale of this self-energization is closely associated with the time scales of coherence and correlation involved with the irreversible loss of information between the quantum system and the reservoirs [56]. As we said before, the retarded and advanced Green's functions, $\boldsymbol{G}^{R}\left(t,t'\right)$ and $\boldsymbol{G}^{A}\left(t,t'\right)$ respectively, describe the causal and anti-causal processes in the quantum system, including the effects of the reservoirs. When a molecular system is subjected to external stimuli that take it out of a state of stationary equilibrium, both Green's functions and the self-energies depend on the time difference and can be expressed in the time domain as functions of the form $f\left(t-t'\right)$ [51]. This allows us to rewrite equations 3.48 and 3.49 in a stationary domain as,

$$\begin{aligned}\boldsymbol{G}^{>}(\omega) &= \boldsymbol{G}^{R}(\omega)\boldsymbol{\Sigma}^{<}(\omega)\boldsymbol{G}^{A}(\omega),\\ \boldsymbol{G}^{<}(\omega) &= \boldsymbol{G}^{R}(\omega)\boldsymbol{\Sigma}^{<}(\omega)\boldsymbol{G}^{A}(\omega).\end{aligned} \tag{3.50}$$

3.5 Retarded Green's Function for FMO-123

With all the above information, we can begin to analyze the FMO-123 system under the formalism of Green's functions. It is necessary to define the delayed Green's function of the system, employing the density of states calculated for a series of level-width Γ values. Which, in this case, quantifies the strength of the coupling between the system and the left and right reservoirs. It should be noted that, for both contacts, the coupling value is the same, but while the left reservoir is connected to site 1, the right reservoir is connected to site 3, thus forming a circuit in which the excitons move from left to right. This is schematized in figure 3.1.

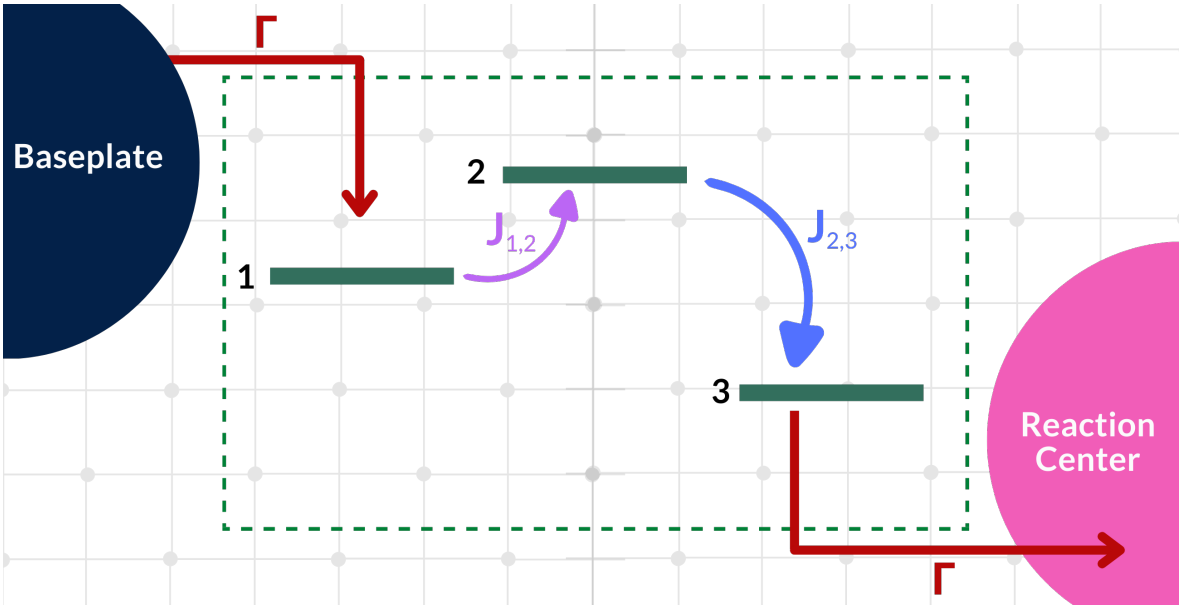

Figure 3.1: Structure of the FMO-123 system. The baseplate, the reaction center, and the three levels (chromophores) are shown in their energy distribution. The couplings between the elements of the system and the coupling with the reservoirs are also schematized.

Returning to the equation 3.44, we can express the delayed green's function for the FMO-123 as,

$$\boldsymbol{G}^R(E) = \left[\boldsymbol{E} - \boldsymbol{H}_{FMO-123} - \boldsymbol{\Sigma}^R\right]^{-1}, \tag{3.51}$$

where the energy matrix $\boldsymbol{E}$, the Hamiltonian of the system $\boldsymbol{H}_{FMO-123}$, and the retarded self-energy matrix $\boldsymbol{\Sigma}^R = \boldsymbol{\Sigma}^{R,(L)} + \boldsymbol{\Sigma}^{R,(R)}$, the sum of the left and right retarded self-energies; are given by respectively:

$$\boldsymbol{E} = \begin{pmatrix} E+i\eta & 0.0 & 0.0 \\ 0.0 & E+i\eta & 0.0 \\ 0.0 & 0.0 & E+i\eta \end{pmatrix}, \ \eta \to 0; \ \boldsymbol{H}_{FMO-123} = \begin{pmatrix} 25.0 & -10.9 & 0.0 \\ -10.9 & 40.0 & 3.8 \\ 0.0 & 3.8 & 0.0 \end{pmatrix},$$

$$\boldsymbol{\Sigma}^{R,(L)} = \frac{-i}{2}\begin{pmatrix} \Gamma & 0.0 & 0.0 \\ 0.0 & 0.0 & 0.0 \\ 0.0 & 0.0 & 0.0 \end{pmatrix}, \ \boldsymbol{\Sigma}^{R,(R)} = \frac{-i}{2}\begin{pmatrix} 0.0 & 0.0 & 0.0 \\ 0.0 & 0.0 & 0.0 \\ 0.0 & 0.0 & \Gamma \end{pmatrix} \to \boldsymbol{\Sigma}^R = \frac{-i}{2}\begin{pmatrix} \Gamma & 0.0 & 0.0 \\ 0.0 & 0.0 & 0.0 \\ 0.0 & 0.0 & \Gamma \end{pmatrix}.$$

If we remember from the equation 2.9, originally units of the Hamiltonian were cm^{-1}, however, to use it in Lindblad's formulation, a scale factor was used to perform the calculation in units of ps^{-1}. In this case, the units of all values, both constants and variables, are millielectronvolts meV. Hence, the equation 2.9 is used again but with the values in meV. On the other hand, the energy parameter E goes from $-20\ meV$ to $60\ meV$, in steps of $0.2\ meV$, and the coupling Γ varies between $0.45\ meV$ to $40\ meV$ in steps of $0.45\ meV$. Then, the equation 3.51 is rewritten,

$$\tilde{\boldsymbol{G}}^R(E) = \left[\begin{pmatrix} E+i\eta & 0.0 & 0.0 \\ 0.0 & E+i\eta & 0.0 \\ 0.0 & 0.0 & E+i\eta \end{pmatrix} - \begin{pmatrix} 25.0 & -10.9 & 0.0 \\ -10.9 & 40.0 & 3.8 \\ 0.0 & 3.8 & 0.0 \end{pmatrix} + \frac{i}{2}\begin{pmatrix} \Gamma & 0.0 & 0.0 \\ 0.0 & 0.0 & 0.0 \\ 0.0 & 0.0 & \Gamma \end{pmatrix}\right]^{-1}. \tag{3.52}$$

This is our unnormalized retarded Green's function and, for the code, the parameter η is neglected, since its value approaches zero. The matrix 3.52 is calculated for each value of the coupling Γ and each magnitude of the energy E. Thus, for each Γ there is an array of matrix Green's functions for each considered energy point.

3.6 Efficiency in the Green's Function Formalism

For each Γ and each point of E, the density of states of the system is calculated through the equation 3.42, given by:

$$A(E) = -\frac{1}{\pi} \operatorname{Im}\left\{ \operatorname{Tr}\left[\tilde{\boldsymbol{G}}^R(E) \right] \right\}, \tag{3.53}$$

then, to normalize the retarded Green's function, we define the mean value of the density of states function,

$$A = \int_{E_{min}}^{E_{max}} A(E)\ dE, \tag{3.54}$$

hence, using the equation 3.52, the normalized matrix representation of the retarded Green's function is:

$$\boldsymbol{G}^R(E) = \frac{\tilde{\boldsymbol{G}}^R(E)}{A}. \tag{3.55}$$

With this definition, we can move on to consider the mean values of the density of states for each state, from equation 3.39 using the normalized form 3.55,

$$A_i = \int_{E_{min}}^{E_{max}} A_i(E)\ dE, \tag{3.56}$$

being that, through the value ρ_1 and ρ_3 for each Γ the Dynamical Efficiency is defined in the Green's function formalism,

$$\bar{\eta}_d(\Gamma) = \frac{A_3(\Gamma)}{A_1(\Gamma)}. \tag{3.57}$$

In figure 3.2, the Dynamical Efficiency given by the equation 3.57 is plotted. As in the results presented in figure 2.8 of subsection 2.3.2, the efficiency has a clear maximum peak. In this case, the maximum efficiency achieved is found at a coupling value Γ equal to 1.8 meV. Unlike the Static Efficiency (see equation 1.9), in this Dynamic Efficiency the variability of the system input is taken into account, through the density of states of site 1.

One of the main differences concerning Lindblad's formalism is that in previous references, such as Ref.[20], there had been talk about the different regimes of the system, quantum, transition, and classical; for the value presented by the dephasing rate. However, for the level-width function Γ, it has not been established clear ranges for this parameter that can be associated with the aforementioned regimes. This can complicate the possibility of comparing both formalisms since it is difficult to make a direct connection between the dephasing rate and the magnitude of the level-width function.

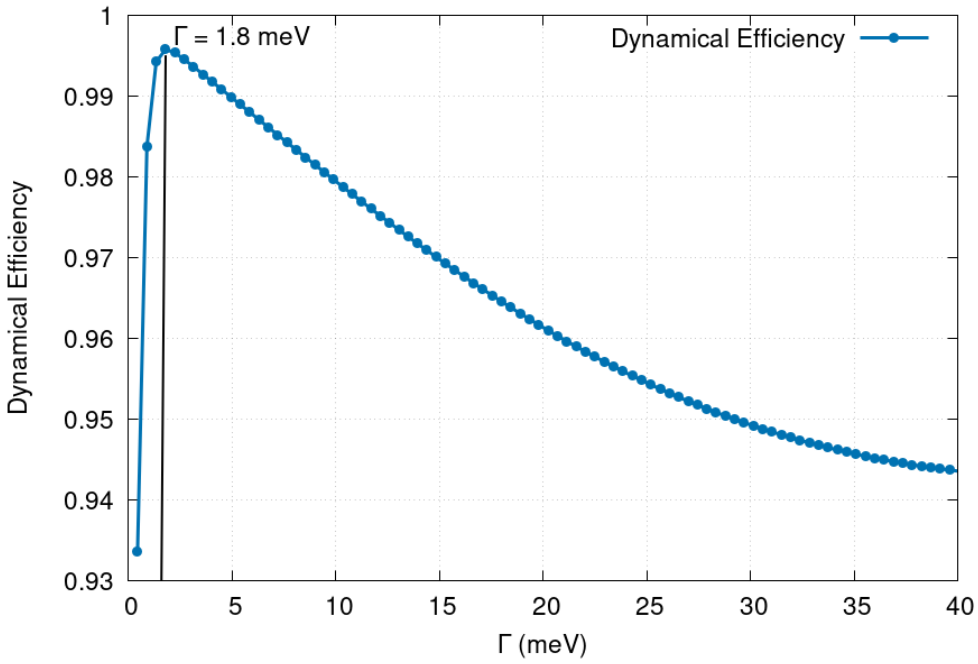

Figure 3.2: Dynamical Efficiency for reduced FMO-123 system regarding the coupling Γ.

On the other hand, what can be said is that the value of the coupling Γ for which there is maximum efficiency, 1.8 meV, has a magnitude comparable to the rest of the system parameters, that is, they do not differ by more than an order of magnitude, as can be seen from section 3.5. It is worth mentioning that, taking Ref.[16] as a starting point, we sought to establish an interval for Γ around 1.45 meV. Subsequently, this is extended to 60 meV to capture the drop in Dynamic Efficiency adequately.

The Dynamical Efficiency in the FMO-123 analyzed using Green's functions provides information about the probability of energy transfer between the levels of the system. As it is shown in Figure 3.2, we have measured a Dynamical Efficiency that is closer to the unity in their maximum peak. Some possible explanations for this phenomenon can be related to quantum effects because, in quantum systems, quantum coherence and interference can lead to unexpected behaviors and higher energy transfer efficiencies than might be classically expected. However, it is also important to highlight that this efficiency is an average since it does not consider quantum fluctuations directly. Aside from that, it is related to one of the many complex processes that take place during the macroprocess of photosynthesis in green sulfur bacteria. Then, we are not talking about the total efficiency of photosynthesis.

Continuing with other possible explanations for our high value of the Dynamical Efficiency, our FMO-123 system can be configured optimally for power transfer under specific conditions. Optimizing system parameters, such as interlevel coupling and level energies, which can lead to improved efficiency. Besides, the environment in which the system is located, that can have a significant impact on its behavior, as we explored in chapter 2. Interaction with the environment can favor certain processes and contribute to improved efficiency.

It is essential to analyze these results in detail and compare them with experimental results to

validate them. Ultimately, achieving an efficiency close to the unity in a quantum system may have important implications for understanding energy transfer in photosynthetic systems and could have applications in the design of quantum technologies. We can also understand this high efficiency from the density of states. To do so, we plot the density of states function of the equation 3.53 using the normalized form 3.55 for the level-width equals 1.8 meV, value at which we obtain maximum efficiency. This can be seen in figure 3.3.

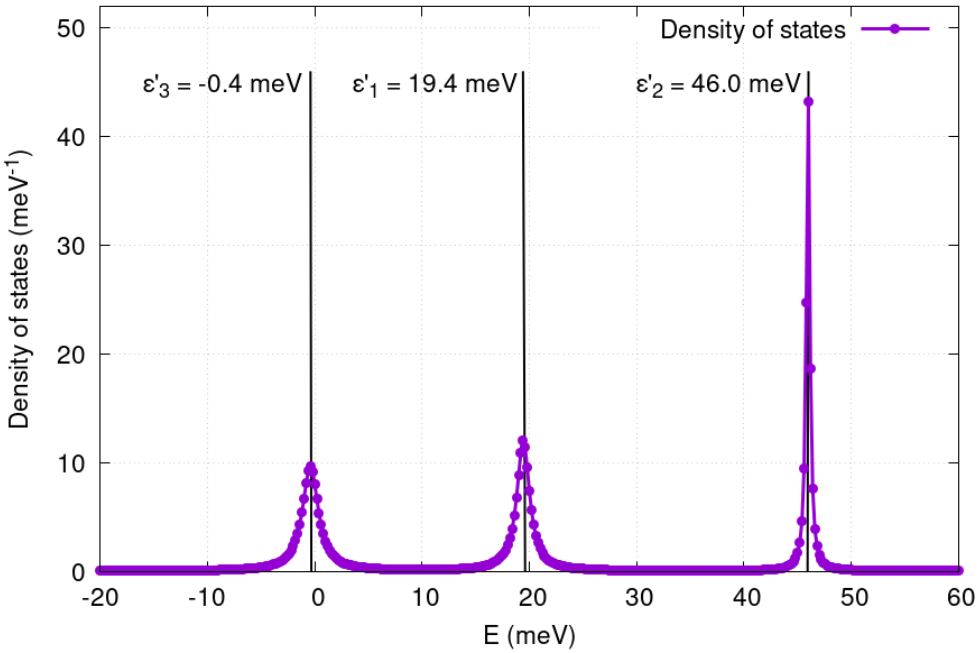

Figure 3.3: Density of states for reduced FMO-123 system for the coupling $\Gamma = 1.8\ meV$.

The density of states function has three peaks with the Lorentzian form with the maxima corresponding to the eigenenergies of the central system and broadening being dependent on the coupling to the electrodes and with the other levels, this result is exactly what was expected taking into account the shape of the system's retarded Green's function [51]. As the couplings are finite interactions between the states and the reservoirs, we observe the shift of the level positions, they reflect now the positions of the eigenenergies $\varepsilon_1' = 19.4\ meV$, $\varepsilon_2' = 46.0\ meV$, and $\varepsilon_3' = -0.4\ meV$; and also some change of width. Besides, the third peak, related to the second eigenenergy ε_2', is much thinner because the second level is not directly coupled to the electrodes and broadening is possible only indirectly through the first and the third level; thus, the level broadening is smaller than the others [51]. In addition to this function, which is the trace of the density of states matrix, we can plot each of the elements of the diagonal. The three graphs are represented in figure 3.4.

In these three graphs, it can be seen how the density of states 3 presents only a strong peak in the third eigenenergy, as expected. However, both the density of states 1 and 2 show two peaks in the first and second eigenenergies, highlighting the fact that their coupling is high, this could also be a trace of the quantum beating that we reviewed in the previous chapters when the population from site 1 and 2 had a related oscillatory behavior. Furthermore, we can notice the similarity between the area under the curve of the density of states 3 and 1, which is what ultimately leads to the ratio between them being so close to unity. According to that point, it is the convention

of an identical sequential coupling (see equation 3.52) that would have a greater impact on the Dynamical Efficiency result.

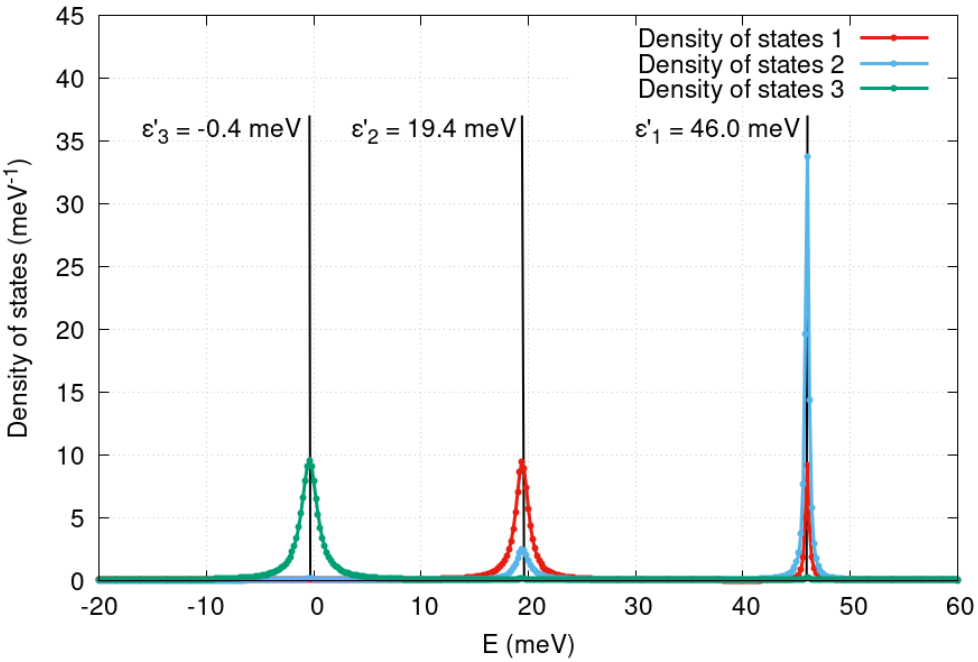

Figure 3.4: Density of states 1, 2, and 3 for reduced FMO-123 system for the coupling $\Gamma = 1.8\ meV$.

Chapter 4

Conclusions

This study analyzed the average efficiency of the reduced photosynthetic complex FMO-123 using both, the master Lindblad equation and Green's function formalisms. From the two results obtained, it is highlighted how the calculation of the Dynamic Efficiency takes into account the dynamics reflected in the input power at site 1, thus considering both the input and output of the system for both formalisms. This provides a more complete understanding of the system behavior, allowing us to achieve a higher maximum efficiency value while maintaining the same functional behavior observed in Static Efficiency through the Lindblad equation.

On the other hand, by finding the maximum value of the Dynamic Efficiency in the transition regime, with the Lindblad equation, it is evident how an adequate calibration of the effects of the environment on the system, quantified by the dephasing rate, allows achieving a high average efficiency. This is why this regime is defined as the environment-assisted quantum transport mechanism (ENAQT) since it is in this regime where the effects of the environment substantially influence the high value of the Dynamic Efficiency, something that later it is extended to the analysis with Green functions.

Besides, as previously stated, the Dynamic Efficiency also shows a maximum peak in the green's functions formalism. In the past case, it occurs at a value of 50 ps^{-1} of the phase shift rate reaching almost 70%, while in the last one, it occurs at a value of 1.8 meV of the coupling Γ between the system and the inlet and outlet reservoirs, reaching a value of 99%. The fact that the efficiency peak is present in both cases suggests that the FMO-123 system does present a favorable value in which the influence of the environment allows achieving a high average efficiency.

Although in the case of Green functions, it is not possible to clarify an association between the regimes of the system and the heat of the coupling, as if established with Lindblad, the value at which the maximum is found is comparable to the parameters selected to evolve the system, so we cannot associate it to the quantum regime directly. Furthermore, it is important to highlight the need to analyze this last result in more depth, since although the efficiency of photosynthesis carried out by sulfur-green bacteria is high, a value close to unity is not following what was expected.

Additionally, when reviewing the spectral function of each site, states 1 and 2 reflect their high coupling, being a possible trace of the quantum beat that was observed when plotting the population of sites 1 and 2 with the Lindblad equation. This allows us to establish another pattern of behavior between both tools, reflecting that surely the value at which the efficiency peak occurs with green functions is closer to the quantum regime than to the classical one. Well, the action of the entanglement discussed in section 1.3 is palpable in both results. However, because the result obtained through Lindblad fits more with what was expected given the previous references [46, 62], the ENAQT regime continues to be the one that has the characteristics that allow high efficiency to be achieved.

It is worth mentioning that, although the objective of this study was to investigate whether the FMO complex uses quantum coherence to improve its transport processes, the use of the Lindblad formalism revealed that the high efficiency of this complex is not achieved in the regime quantum, where quantum beating is present, but rather in the ENAQT regime, where quantum beating is absent. This could reveal that the efficiency can be maximum for a specific value of the dephasing rate, that is, of the assistance from the environment, regardless of whether this assistance leads to the presence of long-lived coherences in the system.

4.1 Perspective: Excitonic Current

The next step in this work is to consolidate the information obtained through the study of the average efficiencies through the analysis of the excitonic current. As explored in the section 2.4 through the Lindblad equation, knowing the current's functional form can reveal much about what transport is like within the reduced complex FMO-123. In this section we sought to establish a starting point for the subsequent analysis of the current, the preliminary results showed a behavior similar to that evidenced by the average efficiency and populations calculated previously in chapter 2. However, it would be worth comparing what was obtained with a more elaborate development that does not start from the same premises and limitations that are considered when using the Lindblad equation.

Moreover, we wanted to use the nonequilibrium Green's functions to review the Dynamic Efficiency of the reduced FMO-123 system, however, these functions have remained in equilibrium. As is known, non-equilibrium Green's functions are defined as the two-time functions $G(t_1, t_2)$. This complication is the price to pay for the possibility of considering time-dependent phenomena, delayed interactions, memory, etc [51]. In our stationary case, we do not have time-dependent external fields and Green's functions depend only on time differences $G(t_1 - t_2) = G(\tau)$. Furthermore, the properties that we have used to define the results are applicable in the equilibrium case of the Fourie-transformed retarded and advanced Green's functions.

This is a very well-achieved approach, which allows us to have the simplicity of a stationary problem while exploring a perspective that contrasts with Lindblad's formalism, with this we can enrich the discussion around both formalisms, contributing to the study of the efficiency of the FMO photosynthetic complex in general. Nevertheless, it remains a fundamental step to use the excitonic current calculated through the non-equilibrium Green's functions to expand the comparison of the formalisms.

4.1.1 The Quantum Transport of Excitons Across the FMO Complex

Excitons are quasiparticles formed when an electron is excited leaving a hole behind, known as an electronic excitation's bound state. In our previous chapters, we considered a bath of vibrations coupled to the FMO complex. Here, we formulate a novel idea to include fermionic reservoirs in the quantum transport problem of excitons across the FMO. Consider a junction system made of two leads and the FMO monomer, one of the leads is the antenna (chlorosome) and the other one is the reaction center.

Conventionally, bosonic baths are used to model the effect of the environment on quantum coherence in the FMO monomer's efficiency, however, fermionic baths allow for particle exchange, therefore this adds a degree of freedom absent in the case of Bosonic baths. In the process of transferring an excitation from the antenna to the reaction center a photon is absorbed by the antenna excites an electron and this excitation is transferred to the reaction center with an efficiency close to unity. The injected exciton created by the photon is modeled as a fermion coupled time-dependently to the FMO, which couples to the reaction center. This process may be modeled as follows. The Hamiltonian that will be considered for the system studied is:

$$\hat{H} = \underbrace{\sum_{\vec{k}\sigma} \varepsilon_{\vec{k}\sigma} \hat{C}^{\dagger}_{\vec{k}\sigma} \hat{C}_{\vec{k}\sigma}}_{\hat{H}_L} + \underbrace{\sum_{m\sigma} \varepsilon_{m\sigma} \hat{d}^{\dagger}_{m\sigma} \hat{d}_{m\sigma}}_{\hat{H}_c} + \underbrace{\sum_{\vec{q}\sigma} \varepsilon_{\vec{q}\sigma} \hat{C}^{\dagger}_{\vec{q}\sigma} \hat{C}_{\vec{q}\sigma}}_{\hat{H}_R} + \underbrace{\sum_{\vec{k}\sigma m} V_{\vec{k}\sigma m} \hat{C}^{\dagger}_{\vec{k}\sigma} \hat{d}_{m\sigma} + \sum_{\vec{k}\sigma m} V^{*}_{\vec{k}\sigma m} \hat{d}^{\dagger}_{m\sigma} \hat{C}_{\vec{k}\sigma} + \sum_{\vec{q}\sigma m} V_{\vec{q}\sigma m} \hat{C}^{\dagger}_{\vec{q}\sigma} \hat{d}_{m\sigma} + \sum_{\vec{q}\sigma m} V^{*}_{\vec{q}\sigma m} \hat{d}^{\dagger}_{m\sigma} \hat{C}_{\vec{q}\sigma}}_{\hat{H}_T} . \tag{4.1}$$

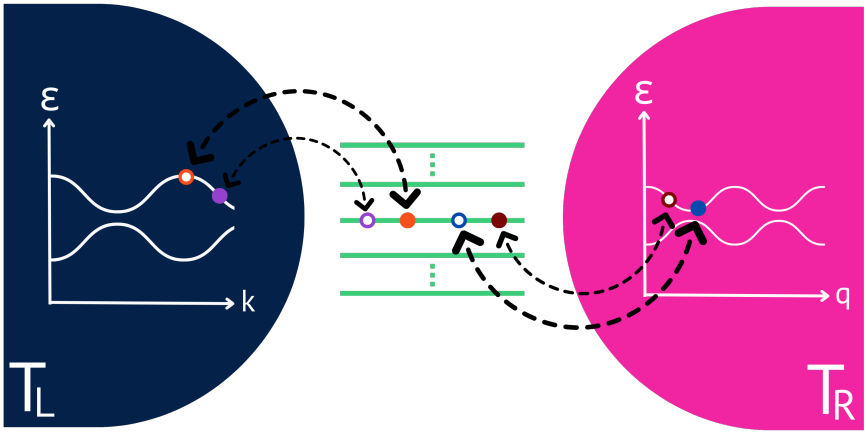

Figure 4.1: Diagram of the system, consisting of two contacts and a central zone. Note that the colors used in the scheme coincide with those presented in the equation 4.1.

The energy dispersion of the antenna and the reaction center is respectively $\varepsilon_{\vec{k}\sigma}$ and $\varepsilon_{\vec{q}\sigma}$ where $\varepsilon_{\vec{k}\sigma}$ carries extreme time dependence coming from the absorption of a photon. Operators $\hat{C}^{\dagger}_{\vec{k}\sigma}$ and $\hat{C}_{\vec{k}\sigma}$

represent the creation and annihilation of excitons injected from the antenna onto the FMO, and the operators $\varepsilon_{\vec{q}\sigma}\ \hat{C}^{\dagger}_{\vec{q}\sigma}\hat{C}_{\vec{q}\sigma}$ represent creation and annihilation of excitons in the reaction center. Operators $\hat{d}^{\dagger}_{m\sigma}$ and $\hat{d}_{m\sigma}$ create and annihilate excitons on the FMO.

Importantly, for the asymmetry required by this problem, the parameter $V_{\vec{k}\sigma m}$ represents the hybridization between the antenna and the FMO which is different than the hybridization parameter between the FMO and the antenna namely $V^{*}_{\vec{k}\sigma m}$, which in practice should carry extreme time dependence. Similarly, $V_{\vec{q}\sigma m}$ represents the hybridization between the reaction center and the FMO which is also different from the hybridization parameter between the FMO and the reaction center namely $V^{*}_{\vec{q}\sigma m}$.

Now, we will consider the flow of charge in the excitation process by defining the following current operator:

$$\hat{J}^{(Q)}_{L}(t) = -\frac{ie}{\hbar}\sum_{\vec{k}\sigma}\left[\hat{C}^{\dagger}_{\vec{k}\sigma}(t)\hat{C}_{\vec{k}\sigma}(t), \hat{H}\right], \tag{4.2}$$

where its expectation value in the linear response regime is given by,

$$\hat{J}^{(Q)}_{L}(t) = J^{(Q)}_{L}(t) \approx \frac{2e}{\hbar}\sum_{\vec{k}\vec{k}'\sigma\sigma'}\sum_{mn}\mathrm{IM}\, V_{\vec{k}\sigma m}V^{*}_{\vec{k}'\sigma' n}\left(-\frac{i}{\hbar}\right)\int_{-\infty}^{t}\left\langle\left[\hat{C}^{\dagger}_{\vec{k}\sigma}(t)\hat{d}_{m\sigma}(t), \hat{d}^{\dagger}_{n\sigma'}(\tau)\hat{C}_{\vec{k}'\sigma'}(\tau)\right]\right\rangle d\tau. \tag{4.3}$$

After the evaluation of the expectation values in the Hartree-Fock Approximation,

$$J^{(Q)}_{L}(t) \approx 2e\sum_{\vec{k}\sigma mn}\mathrm{IM}\, V_{\vec{k}\sigma m}V^{*}_{\vec{k}\sigma n}(-i)\int_{-\infty}^{t}d\tau\left(G^{>}_{mn\sigma\sigma'}(t,\tau)g^{<}_{\vec{k}\sigma}(\tau,t) - G^{<}_{mn\sigma\sigma'}(t,\tau)g^{>}_{\vec{k}\sigma}(\tau,t)\right). \tag{4.4}$$

It is often convenient to start from the steady state regime, by considering the non-equilibrium Green's functions for the leads as follows:

$$g^{<}_{\vec{k}\sigma}(\varepsilon) = \frac{2\pi i}{\hbar}f_{L}(\varepsilon)\delta(\varepsilon - \varepsilon_{\vec{k}\sigma}), \qquad g^{>}_{\vec{k}\sigma}(\varepsilon) = -\frac{2\pi i}{\hbar}f_{L}(-\varepsilon)\delta(\varepsilon - \varepsilon_{\vec{k}\sigma}), \tag{4.5}$$

and by defining the lineshape parameter $\Gamma_{nm\sigma}(\varepsilon)$ as:

$$\Gamma_{nm\sigma}(\varepsilon) = 2\pi V^{*}_{n\sigma}\rho(\varepsilon)V_{m\sigma}(\varepsilon), \tag{4.6}$$

then, the final expression, for the current of injected excitons from the antenna in a steady state is given by,

$$J^{(Q)}_{L}(t) \approx e\int\frac{d\varepsilon}{2\pi}\ Tr\left(\boldsymbol{\Sigma}^{>}(\varepsilon)\ \boldsymbol{G}^{<}(\varepsilon) - \boldsymbol{\Sigma}^{<}(\varepsilon)\ \boldsymbol{G}^{>}(\varepsilon)\right), \tag{4.7}$$

and the total excitonic current, in a steady state, can be assumed as the superposition between the left and right lead,

$$J(t) = e\sum_{\alpha}\int\frac{d\varepsilon}{2\pi}\ \mathrm{Tr}\left(\boldsymbol{\Sigma}^{\alpha,>}(\varepsilon)\ \boldsymbol{G}^{<}(\varepsilon) - \boldsymbol{\Sigma}^{\alpha,<}(\varepsilon)\ \boldsymbol{G}^{>}(\varepsilon)\right). \tag{4.8}$$

Here, $\boldsymbol{\Sigma}^{\alpha,>}(\varepsilon)$ and $\boldsymbol{\Sigma}^{\alpha,<}(\varepsilon)$ stands for the greater and lesser self-energy, corresponding to the lead labeled as α which is given by:

$$\Sigma^{\alpha,>}_{mn} = -i\Gamma_{\alpha nm}(\varepsilon)f_{\alpha}(-\varepsilon),\ \Sigma^{\alpha,<}_{mn} = i\Gamma_{\alpha nm}(\varepsilon)f_{\alpha}(\varepsilon). \tag{4.9}$$

This excitonic current represents the total excited charge by the photons absorbed in the antenna transmitted towards the reaction center, and divided by the corresponding heat extracted from the antenna, which shall give a faithful representation of the efficiency in a certain time and energy limit. This calculation is to be further developed by another member of our research group.

Appendix A

Calculating the scale factor for the commutator $[H_{FMO-123}, \rho]$

We know that the master Lindblad equation is:

$$\frac{d\rho}{dt} = \frac{-i}{\hbar}[H_S, \rho] + L[\rho] \;\longrightarrow\; \frac{d\rho}{dt} = -i\left[\frac{H_S}{\hbar}, \rho\right] + L[\rho], \tag{A.1}$$

in the case that A_{ij} is a dimensionless element of the matrix $H_{FMO-123}$ we have:

$$\begin{aligned} H_{ij}\ cm^{-1} \times \frac{1}{\hbar} &= H_{ij}\ cm^{-1} \times \underbrace{\frac{1.986 \times 10^{-23}\ J}{1\ cm^{-1}}}_{1} \times \underbrace{\frac{1}{1.055 \times 10^{-34}\ J\ s}}_{\frac{1}{\hbar}} \times \underbrace{\frac{1\ s}{1 \times 10^{12}\ ps}}_{1} \\ &\approx H_{ij}\ cm^{-1} \times 0.188\ \frac{1}{cm^{-1}\ ps} \\ &= (0.188 \times H_{ij})\ ps^{-1}. \end{aligned} \tag{A.2}$$

Obtaining that, the scale factor in the master Lindblad equation is 0.188 $(cm^{-1})^{-1}\ ps^{-1}$.

$$\frac{d\rho}{dt} = -i[\underbrace{0.188\ \frac{1}{cm^{-1}\ ps}\ H_S}_{H_{FMO-123}}, \rho] + L[\rho]. \tag{A.3}$$

Appendix B

Obtaining the Matrix Form of the Lindblad Quantum Master Equation for FMO-123

$$\hat{H}_{FMO-123} = \sum_{i=0}^{3} \varepsilon_i \hat{c}_i^\dagger \hat{c}_i + \sum_{i,j=0}^{3} t_{i,j} \hat{c}_i^\dagger \hat{c}_j,\ \varepsilon_0 = 0,\ t_{0,j} = t_{i,0} = 0 \rightarrow \hat{H}_{FMO-123} = \sum_{i=1}^{3} \varepsilon_i \hat{c}_i^\dagger \hat{c}_i + \sum_{i,j=1}^{3} t_{i,j} \hat{c}_i^\dagger \hat{c}_j,$$

the Lindblad quantum master equation is given by $\dot{\rho} = -i[H, \rho] + \mathcal{L}[\rho]$, such that:

$$\mathcal{L}[\rho] = -\frac{1}{2}\left\{\hat{V}^\dagger \hat{V}, \rho\right\} + \hat{V}\rho\hat{V}^\dagger.$$

1. Source (Site 1): $\hat{V}_{\text{source}} = (\gamma_{\text{inj}})^{1/2}\, \hat{c}_1^\dagger$
2. Sink (Site 3): $\hat{V}_{\text{sink}} = (\gamma_{\text{ext}})^{1/2}\, \hat{c}_3$.
3. Dephasing: $\hat{V}_{\text{deph},i} = (\gamma_{\text{deph}})^{1/2}\, \hat{c}_i^\dagger \hat{c}_i \rightarrow \hat{V}_{\text{deph}} = (\gamma_{\text{deph}})^{1/2} \sum_i \hat{c}_i^\dagger \hat{c}_i$.

The steady form of the Lindblad equation is:

$$\underbrace{-\frac{i}{\hbar}[\hat{H}_{FMO-123}, \rho]}_{1} + \underbrace{\mathcal{L}_{\text{inj}}[\rho]}_{2} + \underbrace{\mathcal{L}_{\text{ext}}[\rho]}_{3} + \underbrace{\mathcal{L}_{\text{deph}}[\rho]}_{4} = \frac{d\hat{\rho}}{dt},$$

If our basis is $\{|i\rangle\}_{i=1}^{3}$ of the Hilbert Space, the density matrix in this basis is written as $\rho = \sum_{m,l=0} \rho_{m,l} |m\rangle\langle l|$:

$$\begin{aligned} 1) \quad -\frac{i}{\hbar}\left[\hat{H}_{FMO-123}, \rho\right] &= -\frac{i}{\hbar}\left[\sum_{i=1}^{3} \varepsilon_i |i\rangle\langle i| + \sum_{i,j=1}^{3} t_{i,j} |i\rangle\langle j|, \sum_{m,l=0} \rho_{m,l} |m\rangle\langle l|\right] \\ &= -\frac{i}{\hbar}\left[\sum_{i=1}^{3} \varepsilon_i |i\rangle\langle i|, \sum_{m,l=0} \rho_{m,l} |m\rangle\langle l|\right] - \frac{i}{\hbar}\left[\sum_{i,j=1}^{3} t_{i,j} |i\rangle\langle j|, \sum_{m,l=0} \rho_{m,l} |m\rangle\langle l|\right]. \end{aligned}$$

$$\longrightarrow \sum_{m,l=0} \rho_{m,l}|m\rangle\langle l| = \rho_{0,0}|0\rangle\langle 0| + \sum_{m=1} \rho_{m,0}|m\rangle\langle 0| + \sum_{l=1} \rho_{0,l}|0\rangle\langle l| + \sum_{m,l=1} \rho_{m,l}|m\rangle\langle l|.$$

$$\begin{aligned}
= & -\frac{i}{\hbar}\left[\sum_{i=1}^{3}\varepsilon_i|i\rangle\langle i|, \rho_{0,0}|0\rangle\langle 0| + \sum_{m=1}\rho_{m,0}|m\rangle\langle 0| + \sum_{l=1}\rho_{0,l}|0\rangle\langle l| + \sum_{m,l=1}\rho_{m,l}|m\rangle\langle l|\right] \\
& -\frac{i}{\hbar}\left[\sum_{i,j=1}^{3} t_{i,j}|i\rangle\langle j|, \rho_{0,0}|0\rangle\langle 0| + \sum_{m=1}\rho_{m,0}|m\rangle\langle 0| + \sum_{l=1}\rho_{0,l}|0\rangle\langle l| + \sum_{m,l=1}\rho_{m,l}|m\rangle\langle l|\right] \\
= & -\frac{i}{\hbar}\left(\sum_{i=1}^{3}\varepsilon_i|i\rangle\langle i| \cdot \left(\rho_{0,0}|0\rangle\langle 0| + \sum_{m=1}\rho_{m,0}|m\rangle\langle 0| + \sum_{l=1}\rho_{0,l}|0\rangle\langle l| + \sum_{m,l=1}\rho_{m,l}|m\rangle\langle l|\right)\right) \\
& +\frac{i}{\hbar}\left(\left(\rho_{0,0}|0\rangle\langle 0| + \sum_{m=1}\rho_{m,0}|m\rangle\langle 0| + \sum_{l=1}\rho_{0,l}|0\rangle\langle l| + \sum_{m,l=1}\rho_{m,l}|m\rangle\langle l|\right) \cdot \sum_{i=1}^{3}\varepsilon_i|i\rangle\langle i|\right) \\
& -\frac{i}{\hbar}\left(\sum_{i,j=1}^{3} t_{i,j}|i\rangle\langle j| \cdot \left(\rho_{0,0}|0\rangle\langle 0| + \sum_{m=1}\rho_{m,0}|m\rangle\langle 0| + \sum_{l=1}\rho_{0,l}|0\rangle\langle l| + \sum_{m,l=1}\rho_{m,l}|m\rangle\langle l|\right)\right) \\
& +\frac{i}{\hbar}\left(\left(\rho_{0,0}|0\rangle\langle 0| + \sum_{m=1}\rho_{m,0}|m\rangle\langle 0| + \sum_{l=1}\rho_{0,l}|0\rangle\langle l| + \sum_{m,l=1}\rho_{m,l}|m\rangle\langle l|\right) \cdot \sum_{i,j=1}^{3} t_{i,j}|i\rangle\langle j|\right) \\
= & -\frac{i}{\hbar}\left(\sum_{i=1}^{3}\varepsilon_i\rho_{0,0}|i\rangle\langle i|0\rangle\langle 0| + \sum_{i,m=1}^{3}\varepsilon_i\rho_{m,0}|i\rangle\langle i|m\rangle\langle 0| + \sum_{i,l=1}^{3}\varepsilon_i\rho_{0,l}|i\rangle\langle i|0\rangle\langle l| + \sum_{i,l,m=1}^{3}\varepsilon_i\rho_{m,l}|i\rangle\langle i|m\rangle\langle l|\right) \\
& +\frac{i}{\hbar}\left(\sum_{i=1}^{3}\varepsilon_i\rho_{0,0}|0\rangle\langle 0|i\rangle\langle i| + \sum_{i,m=1}^{3}\varepsilon_i\rho_{m,0}|m\rangle\langle 0|i\rangle\langle i| + \sum_{i,l=1}^{3}\varepsilon_i\rho_{0,l}|0\rangle\langle l|i\rangle\langle i| + \sum_{i,l,m=1}^{3}\varepsilon_i\rho_{m,l}|m\rangle\langle l|i\rangle\langle i|\right) \\
& -\frac{i}{\hbar}\left(\sum_{i,j=1}^{3} t_{i,j}\rho_{0,0}|i\rangle\langle j|0\rangle\langle 0| + \sum_{i,j,m=1}^{3} t_{i,j}\rho_{m,0}|i\rangle\langle j|m\rangle\langle 0| + \sum_{i,j,l=1}^{3} t_{i,j}\rho_{0,l}|i\rangle\langle j|0\rangle\langle l| + \sum_{i,j,m,l=1}^{3} t_{i,j}\rho_{m,l}|i\rangle\langle j|m\rangle\langle l|\right) \\
& +\frac{i}{\hbar}\left(\sum_{i,j=1}^{3} t_{i,j}\rho_{0,0}|0\rangle\langle 0|i\rangle\langle j| + \sum_{i,j,m=1}^{3} t_{i,j}\rho_{m,0}|m\rangle\langle 0|i\rangle\langle j| + \sum_{i,j,l=1}^{3} t_{i,j}\rho_{0,l}|0\rangle\langle l|i\rangle\langle j| + \sum_{i,j,m,l=1}^{3} t_{i,j}\rho_{m,l}|m\rangle\langle l|i\rangle\langle j|\right) \\
= & -\frac{i}{\hbar}\left(\sum_{i,m=1}^{3}\varepsilon_i\rho_{m,0}\delta_{im}|i\rangle\langle 0| + \sum_{i,l,m=1}^{3}\varepsilon_i\rho_{m,l}\delta_{im}|i\rangle\langle l| - \sum_{i,l=1}^{3}\varepsilon_i\rho_{0,l}\delta_{li}|0\rangle\langle i| - \sum_{i,l,m=1}^{3}\varepsilon_i\rho_{m,l}\delta_{li}|m\rangle\langle i|\right) \\
& -\frac{i}{\hbar}\left(\sum_{i,j,m=1}^{3} t_{i,j}\rho_{m,0}\delta_{jm}|i\rangle\langle 0| + \sum_{i,j,m,l=1}^{3} t_{i,j}\rho_{m,l}\delta_{jm}|i\rangle\langle l| - \sum_{i,j,l=1}^{3} t_{i,j}\rho_{0,l}\delta_{li}|0\rangle\langle j| - \sum_{i,j,m,l=1}^{3} t_{i,j}\rho_{m,l}\delta_{li}|m\rangle\langle j|\right) \\
= & -\frac{i}{\hbar}\left(\sum_{i=1}^{3}\varepsilon_i\rho_{i,0}|i\rangle\langle 0| + \sum_{l,m=1}^{3}\varepsilon_m\rho_{m,l}|m\rangle\langle l| - \sum_{i=1}^{3}\varepsilon_i\rho_{0,i}|0\rangle\langle i| - \sum_{l,m=1}^{3}\varepsilon_l\rho_{m,l}|m\rangle\langle l|\right)
\end{aligned}$$

$$-\frac{i}{\hbar}\left(\sum_{i,m=1}^{3} t_{i,m}\rho_{m,0}|i\rangle\langle 0| + \sum_{i,m,l=1}^{3} t_{i,m}\rho_{m,l}|i\rangle\langle l| - \sum_{j,l=1}^{3} t_{l,j}\rho_{0,l}|0\rangle\langle j| - \sum_{j,m,l=1}^{3} t_{l,j}\rho_{m,l}|m\rangle\langle j|\right).$$

$$\begin{aligned}-\frac{i}{\hbar}\left[\hat{H}_{FMO-123},\rho\right] &= -\frac{i}{\hbar}\left(\sum_{i=1}^{3}\varepsilon_i\left(\rho_{i,0}|i\rangle\langle 0| - \rho_{0,i}|0\rangle\langle i|\right) + \sum_{l,m=1}^{3}\left(\varepsilon_m-\varepsilon_l\right)\rho_{m,l}|m\rangle\langle l| + \sum_{i,m,l=1}^{3} t_{i,m}\rho_{m,l}|i\rangle\langle l|\right.\\ &\quad \left. - \sum_{j,m,l=1}^{3} t_{l,j}\rho_{m,l}|m\rangle\langle j|\right). \end{aligned} \tag{B.1}$$

$$\begin{aligned}2)\ \mathcal{L}_{\text{inj}}[\rho] &= \frac{-1}{2}\left\{\hat{V}^{\dagger}_{\text{source}}\hat{V}_{\text{source}},\rho\right\} + \hat{V}_{\text{source}}\rho\hat{V}^{\dagger}_{\text{source}}\\ &= \frac{-1}{2}\left(\hat{V}^{\dagger}_{\text{source}}\hat{V}_{\text{source}}\rho + \rho\hat{V}^{\dagger}_{\text{source}}\hat{V}_{\text{source}}\right) + \hat{V}_{\text{source}}\rho\hat{V}^{\dagger}_{\text{source}}\\ &= \frac{-1}{2}\left(\left(\gamma_{\text{inj}}\right)^{1/2}\hat{c}_1\left(\gamma_{\text{inj}}\right)^{1/2}\hat{c}_1^{\dagger}\sum_{m,l=0}\rho_{m,l}|m\rangle\langle l| + \sum_{m,l=0}\rho_{m,l}|m\rangle\langle l|\left(\gamma_{\text{inj}}\right)^{1/2}\hat{c}_1\left(\gamma_{\text{inj}}\right)^{1/2}\hat{c}_1^{\dagger}\right)\\ &+ \left(\gamma_{\text{inj}}\right)^{1/2}\hat{c}_1^{\dagger}\sum_{m,l=0}\rho_{m,l}|m\rangle\langle l|\left(\gamma_{\text{inj}}\right)^{1/2}\hat{c}_1.\end{aligned}$$

$$\rightarrow \sum_{m,l=0}\rho_{m,l}|m\rangle\langle l| = \rho_{0,0}|0\rangle\langle 0| + \sum_{m=1}\rho_{m,0}|m\rangle\langle 0| + \sum_{l=1}\rho_{0,l}|0\rangle\langle l| + \sum_{m,l=1}\rho_{m,l}|m\rangle\langle l|.$$

- First term:

$$\begin{aligned}&= \gamma_{\text{inj}}\left[\rho_{0,0}\hat{c}_1\hat{c}_1^{\dagger}|0\rangle\langle 0| + \sum_{m=1}\rho_{m,0}\hat{c}_1\hat{c}_1^{\dagger}|m\rangle\langle 0| + \sum_{l=1}\rho_{0,l}\hat{c}_1\hat{c}_1^{\dagger}|0\rangle\langle l| + \sum_{m,l=1}\rho_{m,l}\hat{c}_1\hat{c}_1^{\dagger}|m\rangle\langle l|\right]\\ &= \gamma_{\text{inj}}\left[\rho_{0,0}|0\rangle\langle 0| + \sum_{l=1}\rho_{0,l}|0\rangle\langle l|\right]\\ &= \gamma_{\text{inj}}\left[\sum_{l=0}\rho_{0,l}|0\rangle\langle l|\right].\end{aligned}$$

- Second term:

$$\begin{aligned}&= \gamma_{\text{inj}}\left[\rho_{0,0}|0\rangle\langle 0|\hat{c}_1\hat{c}_1^{\dagger} + \sum_{m=1}\rho_{m,0}|m\rangle\langle 0|\hat{c}_1\hat{c}_1^{\dagger} + \sum_{l=1}\rho_{0,l}|0\rangle\langle l|\hat{c}_1\hat{c}_1^{\dagger} + \sum_{m,l=1}\rho_{m,l}|m\rangle\langle l|\hat{c}_1\hat{c}_1^{\dagger}\right]\\ &= \gamma_{\text{inj}}\left[\rho_{0,0}|0\rangle\langle 0| + \sum_{m=1}\rho_{m,0}|m\rangle\langle 0|\right]\\ &= \gamma_{\text{inj}}\left[\sum_{m=0}\rho_{m,0}|m\rangle\langle 0|\right].\end{aligned}$$

- Third term:

$$
\begin{aligned}
&= \gamma_{\text{inj}} \left[\rho_{0,0} \hat{c}_1^\dagger |0\rangle\langle 0| \hat{c}_1 + \sum_{m=1} \rho_{m,0} \hat{c}_1^\dagger |m\rangle\langle 0| \hat{c}_1 + \sum_{l=1} \rho_{0,l} \hat{c}_1^\dagger |0\rangle\langle l| \hat{c}_1 + \sum_{m,l=1} \rho_{m,l} \hat{c}_1^\dagger |m\rangle\langle l| \hat{c}_1 \right] \\
&= \gamma_{\text{inj}} \left[\rho_{0,0} |1\rangle\langle 1| \right].
\end{aligned}
$$

$$
\mathcal{L}_{\text{inj}}[\rho] = \gamma_{\text{inj}} \left[\rho_{0,0} |1\rangle\langle 1| - \frac{1}{2} \left(\sum_{m=0} \rho_{0,m} |0\rangle\langle m| + \sum_{m=0} \rho_{m,0} |m\rangle\langle 0| \right) \right]. \tag{B.2}
$$

3) $\mathcal{L}_{\text{ext}}[\rho]$

$$
\begin{aligned}
&= \frac{-1}{2} \left\{ \hat{V}_{\text{sink}}^\dagger \hat{V}_{\text{sink}}, \rho \right\} + \hat{V}_{\text{sink}} \rho \hat{V}_{\text{sink}}^\dagger \\
&= \frac{-1}{2} \left(\hat{V}_{\text{sink}}^\dagger \hat{V}_{\text{sink}} \rho + \rho \hat{V}_{\text{sink}}^\dagger \hat{V}_{\text{sink}} \right) + \hat{V}_{\text{sink}} \rho \hat{V}_{\text{sink}}^\dagger \\
&= \frac{-1}{2} \left((\gamma_{\text{ext}})^{1/2} \hat{c}_3^\dagger (\gamma_{\text{ext}})^{1/2} \hat{c}_3 \sum_{m,l=0} \rho_{m,l} |m\rangle\langle l| + \sum_{m,l=0} \rho_{m,l} |m\rangle\langle l| (\gamma_{\text{ext}})^{1/2} \hat{c}_3^\dagger (\gamma_{\text{ext}})^{1/2} \hat{c}_3 \right) \\
&+ (\gamma_{\text{ext}})^{1/2} \hat{c}_3 \sum_{m,l=0} \rho_{m,l} |m\rangle\langle l| (\gamma_{\text{ext}})^{1/2} \hat{c}_3^\dagger.
\end{aligned}
$$

$$
\rightarrow \sum_{m,l=0} \rho_{m,l} |m\rangle\langle l| = \rho_{0,0} |0\rangle\langle 0| + \sum_{m=1} \rho_{m,0} |m\rangle\langle 0| + \sum_{l=1} \rho_{0,l} |0\rangle\langle l| + \sum_{m,l=1} \rho_{m,l} |m\rangle\langle l|.
$$

- First term:

$$
\begin{aligned}
&= \gamma_{\text{ext}} \left[\rho_{0,0} \hat{c}_3^\dagger \hat{c}_3 |0\rangle\langle 0| + \sum_{m=1} \rho_{m,0} \hat{c}_3^\dagger \hat{c}_3 |m\rangle\langle 0| + \sum_{l=1} \rho_{0,l} \hat{c}_3^\dagger \hat{c}_3 |0\rangle\langle l| + \sum_{m,l=1} \rho_{m,l} \hat{c}_3^\dagger \hat{c}_3 |m\rangle\langle l| \right] \\
&= \gamma_{\text{ext}} \left[\rho_{3,0} |3\rangle\langle 0| + \sum_{l=1} \rho_{3,l} |3\rangle\langle l| \right] \\
&= \gamma_{\text{ext}} \left[\sum_{l=0} \rho_{3,l} |3\rangle\langle l| \right].
\end{aligned}
$$

- Second term:

$$
\begin{aligned}
&= \gamma_{\text{ext}} \left[\rho_{0,0} |0\rangle\langle 0| \hat{c}_3^\dagger \hat{c}_3 + \sum_{m=1} \rho_{m,0} |m\rangle\langle 0| \hat{c}_3^\dagger \hat{c}_3 + \sum_{l=1} \rho_{0,l} |0\rangle\langle l| \hat{c}_3^\dagger \hat{c}_3 + \sum_{m,l=1} \rho_{m,l} |m\rangle\langle l| \hat{c}_3^\dagger \hat{c}_3 \right] \\
&= \gamma_{\text{ext}} \left[\rho_{0,3} |0\rangle\langle 3| + \sum_{m=1} \rho_{m,3} |m\rangle\langle 3| \right] \\
&= \gamma_{\text{ext}} \left[\sum_{m=0} \rho_{m,3} |m\rangle\langle 3| \right].
\end{aligned}
$$

- Third term:

$$
\begin{aligned}
&= \gamma_{\text{ext}} \left[\rho_{0,0} \hat{c}_3 |0\rangle\langle 0| \hat{c}_3^\dagger + \sum_{m=1} \rho_{m,0} \hat{c}_3 |m\rangle\langle 0| \hat{c}_3^\dagger + \sum_{l=1} \rho_{0,l} \hat{c}_3 |0\rangle\langle l| \hat{c}_3^\dagger + \sum_{m,l=1} \rho_{m,l} \hat{c}_3 |m\rangle\langle l| \hat{c}_3^\dagger \right] \\
&= \gamma_{\text{ext}} \left[\rho_{3,3} |0\rangle\langle 0| \right].
\end{aligned}
$$

$$
\mathcal{L}_{\text{ext}}[\rho] = \gamma_{\text{ext}} \left[\rho_{3,3} |0\rangle\langle 0| - \frac{1}{2} \left(\sum_{m=0} \rho_{3,m} |3\rangle\langle m| + \sum_{m=0} \rho_{m,3} |m\rangle\langle 3| \right) \right]. \tag{B.3}
$$

$$
\begin{aligned}
4)\ \mathcal{L}_{\text{deph}}[\rho] &= \frac{-1}{2} \left\{ \hat{V}_{\text{deph}}^\dagger \hat{V}_{\text{deph}}, \rho \right\} + \hat{V}_{\text{deph}} \rho \hat{V}_{\text{deph}}^\dagger \\
&= \frac{-1}{2} \left(\hat{V}_{\text{deph}}^\dagger \hat{V}_{\text{deph}} \rho + \rho \hat{V}_{\text{deph}}^\dagger \hat{V}_{\text{deph}} \right) + \hat{V}_{\text{deph}} \rho \hat{V}_{\text{deph}}^\dagger \\
&= \sum_{i=0} \left[\frac{-1}{2} \left(\hat{V}_{\text{deph},i}^\dagger \hat{V}_{\text{deph},i} \rho + \rho \hat{V}_{\text{deph},i}^\dagger \hat{V}_{\text{deph},i} \right) + \hat{V}_{\text{deph},i} \rho \hat{V}_{\text{deph},i}^\dagger \right] \\
&= \sum_{i=0} \left[\frac{-1}{2} \left((\gamma_{\text{deph}})^{1/2} \hat{c}_i^\dagger \hat{c}_i (\gamma_{\text{deph}})^{1/2} \hat{c}_i^\dagger \hat{c}_i \sum_{m,l=0} \rho_{m,l} |m\rangle\langle l| + \sum_{m,l=0} \rho_{m,l} |m\rangle\langle l| (\gamma_{\text{deph}})^{1/2} \hat{c}_i^\dagger \hat{c}_i \right. \right. \\
&\times \left. \left. (\gamma_{\text{deph}})^{1/2} \hat{c}_i^\dagger \hat{c}_i \right) + (\gamma_{\text{deph}})^{1/2} \hat{c}_i^\dagger \hat{c}_i \sum_{m,l=0} \rho_{m,l} |m\rangle\langle l| (\gamma_{\text{deph}})^{1/2} \hat{c}_i^\dagger \hat{c}_i \right] \\
&= \sum_{i=0} \left[\frac{-1}{2} \left(\gamma_{\text{deph}} \hat{c}_i^\dagger \hat{c}_i \hat{c}_i^\dagger \hat{c}_i \sum_{m,l=0} \rho_{m,l} |m\rangle\langle l| + \sum_{m,l=0} \rho_{m,l} |m\rangle\langle l| \gamma_{\text{deph}} \hat{c}_i^\dagger \hat{c}_i \hat{c}_i^\dagger \hat{c}_i \right) \right. \\
&+ \left. \gamma_{\text{deph}} \hat{c}_i^\dagger \hat{c}_i \sum_{m,l=0} \rho_{m,l} |m\rangle\langle l| \ \hat{c}_i^\dagger \hat{c}_i \right].
\end{aligned}
$$

$$
\rightarrow \sum_{m,l=0} \rho_{m,l} |m\rangle\langle l| = \rho_{0,0} |0\rangle\langle 0| + \sum_{m=1} \rho_{m,0} |m\rangle\langle 0| + \sum_{l=1} \rho_{0,l} |0\rangle\langle l| + \sum_{m,l=1} \rho_{m,l} |m\rangle\langle l|.
$$

- First term:

$$
\begin{aligned}
&= \gamma_{\text{deph}} \left[\rho_{0,0} \hat{c}_i^\dagger \hat{c}_i \hat{c}_i^\dagger \hat{c}_i |0\rangle\langle 0| + \sum_{m=1} \rho_{m,0} \hat{c}_i^\dagger \hat{c}_i \hat{c}_i^\dagger \hat{c}_i |m\rangle\langle 0| + \sum_{l=1} \rho_{0,l} \hat{c}_i^\dagger \hat{c}_i \hat{c}_i^\dagger \hat{c}_i |0\rangle\langle l| + \sum_{m,l=1} \rho_{m,l} \hat{c}_i^\dagger \hat{c}_i \hat{c}_i^\dagger \hat{c}_i |m\rangle\langle l| \right] \\
&= \gamma_{\text{deph}} \left[\rho_{i,0} |i\rangle\langle 0| + \sum_{l=1} \rho_{i,l} |i\rangle\langle l| \right] \\
&= \gamma_{\text{deph}} \left[\sum_{l=0} \rho_{i,l} |i\rangle\langle l| \right].
\end{aligned}
$$

- Second term:

$$\begin{aligned}
&= \gamma_{\text{deph}} \left[\rho_{0,0}|0\rangle\langle 0|\hat{c}_i^\dagger \hat{c}_i \hat{c}_i^\dagger \hat{c}_i + \sum_{m=1} \rho_{m,0}|m\rangle\langle 0|\hat{c}_i^\dagger \hat{c}_i \hat{c}_i^\dagger \hat{c}_i + \sum_{l=1} \rho_{0,l}|0\rangle\langle l|\hat{c}_i^\dagger \hat{c}_i \hat{c}_i^\dagger \hat{c}_i + \sum_{m,l=1} \rho_{m,l}|m\rangle\langle l|\hat{c}_i^\dagger \hat{c}_i \hat{c}_i^\dagger \hat{c}_i \right] \\
&= \gamma_{\text{deph}} \left[\rho_{0,i}|0\rangle\langle i| + \sum_{m=1} \rho_{m,i}|m\rangle\langle i| \right] \\
&= \gamma_{\text{deph}} \left[\sum_{m=0} \rho_{m,i}|m\rangle\langle i| \right].
\end{aligned}$$

- Third term:

$$\begin{aligned}
&= \gamma_{\text{deph}} \left[\rho_{0,0}\hat{c}_i^\dagger \hat{c}_i|0\rangle\langle 0|\hat{c}_i^\dagger \hat{c}_i + \sum_{m=1} \rho_{m,0}\hat{c}_i^\dagger \hat{c}_i|m\rangle\langle 0|\hat{c}_i^\dagger \hat{c}_i + \sum_{l=1} \rho_{0,l}\hat{c}_i^\dagger \hat{c}_i|0\rangle\langle l|\hat{c}_i^\dagger \hat{c}_i + \sum_{m,l=1} \rho_{m,l}\hat{c}_i^\dagger \hat{c}_i|m\rangle\langle l|\hat{c}_i^\dagger \hat{c}_i \right] \\
&= \gamma_{\text{deph}} \left[\rho_{i,i}|i\rangle\langle i| \right].
\end{aligned}$$

$$\mathcal{L}_{\text{deph}}[\rho] = \gamma_{\text{deph}} \sum_{i=0} \left[\rho_{i,i}|i\rangle\langle i| - \frac{1}{2} \left(\sum_{l=0} \rho_{i,l}|i\rangle\langle l| + \sum_{m=0} \rho_{m,i}|m\rangle\langle i| \right) \right]. \tag{B.4}$$

Matrices:

$$1)\ \mathbb{M}_1 = -\frac{i}{\hbar}\left[\hat{H}_{FMO-123}, \rho\right] = -\frac{i}{\hbar}\left(\hat{H}_{FMO-123}\rho - \rho\hat{H}_{FMO-123}\right). \tag{B.5}$$

$$\begin{pmatrix} 0 & 0 & 0 & 0 \\ 0 & \varepsilon_1 & t_{1,2} & 0 \\ 0 & t_{1,2} & \varepsilon_2 & t_{2,3} \\ 0 & 0 & t_{2,3} & \varepsilon_3 \end{pmatrix} \cdot \begin{pmatrix} \rho_{0,0} & \rho_{0,1} & \rho_{0,2} & \rho_{0,3} \\ \rho_{1,0} & \rho_{1,1} & \rho_{1,2} & \rho_{1,3} \\ \rho_{2,0} & \rho_{2,1} & \rho_{2,2} & \rho_{2,3} \\ \rho_{3,0} & \rho_{3,1} & \rho_{3,2} & \rho_{3,3} \end{pmatrix} - \begin{pmatrix} \rho_{0,0} & \rho_{0,1} & \rho_{0,2} & \rho_{0,3} \\ \rho_{1,0} & \rho_{1,1} & \rho_{1,2} & \rho_{1,3} \\ \rho_{2,0} & \rho_{2,1} & \rho_{2,2} & \rho_{2,3} \\ \rho_{3,0} & \rho_{3,1} & \rho_{3,2} & \rho_{3,3} \end{pmatrix} \cdot \begin{pmatrix} 0 & 0 & 0 & 0 \\ 0 & \varepsilon_1 & t_{1,2} & 0 \\ 0 & t_{1,2} & \varepsilon_2 & t_{2,3} \\ 0 & 0 & t_{2,3} & \varepsilon_3 \end{pmatrix}$$

$$= \begin{pmatrix} 0 & 0 & 0 \\ \varepsilon_1\rho_{1,0} + t_{1,2}\rho_{2,0} & \varepsilon_1\rho_{1,1} + t_{1,2}\rho_{2,1} & \varepsilon_1\rho_{1,2} + t_{1,2}\rho_{2,2} \\ \varepsilon_2\rho_{2,0} + t_{1,2}\rho_{1,0} + t_{2,3}\rho_{3,0} & \varepsilon_2\rho_{2,1} + t_{1,2}\rho_{1,1} + t_{2,3}\rho_{3,1} & \varepsilon_2\rho_{2,2} + t_{1,2}\rho_{1,2} + t_{2,3}\rho_{3,2} \\ \varepsilon_3\rho_{3,0} + t_{2,3}\rho_{2,0} & \varepsilon_3\rho_{3,1} + t_{2,3}\rho_{2,1} & \varepsilon_3\rho_{3,2} + t_{2,3}\rho_{2,2} \end{pmatrix}$$

$$\begin{pmatrix} 0 \\ \varepsilon_1\rho_{1,3} + t_{1,2}\rho_{2,3} \\ \varepsilon_2\rho_{2,3} + t_{1,2}\rho_{1,3} + t_{2,3}\rho_{3,3} \\ \varepsilon_3\rho_{3,3} + t_{2,3}\rho_{2,3} \end{pmatrix} - \begin{pmatrix} 0 & \varepsilon_1\rho_{0,1} + t_{1,2}\rho 0,2 & \varepsilon_2\rho_{0,2} + t_{1,2}\rho_{0,1} + t_{2,3}\rho_{0,3} & \varepsilon_3\rho_{0,3} + t_{2,3}\rho_{0,2} \\ 0 & \varepsilon_1\rho_{1,1} + t_{1,2}\rho 1,2 & \varepsilon_2\rho_{1,2} + t_{1,2}\rho_{1,1} + t_{2,3}\rho_{1,3} & \varepsilon_3\rho_{1,3} + t_{2,3}\rho_{1,2} \\ 0 & \varepsilon_1\rho_{2,1} + t_{1,2}\rho 2,2 & \varepsilon_2\rho_{2,2} + t_{1,2}\rho_{2,1} + t_{2,3}\rho_{2,3} & \varepsilon_3\rho_{2,3} + t_{2,3}\rho_{2,2} \\ 0 & \varepsilon_1\rho_{3,1} + t_{1,2}\rho 3,2 & \varepsilon_2\rho_{3,2} + t_{1,2}\rho_{3,1} + t_{2,3}\rho_{3,3} & \varepsilon_3\rho_{3,3} + t_{2,3}\rho_{3,2} \end{pmatrix}.$$

$$\mathbb{M}_1 = \frac{-i}{\hbar} \cdot \begin{bmatrix} 0 & -\varepsilon_1 \cdot \rho_{0,1} - t_{1,2} \cdot \rho_{0,2} \\ \varepsilon_1 \cdot \rho_{1,0} + t_{1,2} \cdot \rho_{2,0} & t_{1,2} \cdot (\rho_{2,1} - \rho_{1,2}) \\ \varepsilon_2 \cdot \rho_{2,0} + t_{1,2} \cdot \rho_{1,0} + t_{2,3} \cdot \rho_{3,0} & (\varepsilon_2 - \varepsilon_1) \cdot \rho_{2,1} + t_{1,2} \cdot (\rho_{1,1} - \rho_{2,2}) + t_{2,3} \cdot \rho_{3,1} \\ \varepsilon_3 \cdot \rho_{3,0} + t_{2,3} \cdot \rho_{2,0} & (\varepsilon_3 - \varepsilon_1) \cdot \rho_{3,1} - t_{1,2} \cdot \rho_{3,2} + t_{2,3} \cdot \rho_{2,1} \end{bmatrix} \tag{B.6}$$

$$\begin{bmatrix} -\varepsilon_2 \cdot \rho_{0,2} - t_{1,2} \cdot \rho_{0,1} - t_{2,3} \cdot \rho_{0,3} & -\varepsilon_3 \cdot \rho_{0,3} - t_{2,3} \cdot \rho_{0,2} \\ (\varepsilon_1 - \varepsilon_2) \cdot \rho_{1,2} + t_{1,2} \cdot (\rho_{2,2} - \rho_{1,1}) - t_{2,3} \cdot \rho_{1,3} & (\varepsilon_1 - \varepsilon_3) \cdot \rho_{1,3} + t_{1,2} \cdot \rho_{2,3} - t_{2,3} \cdot \rho_{1,2} \\ t_{1,2} \cdot (\rho_{1,2} - \rho_{2,1}) + t_{2,3} \cdot (\rho_{3,2} - \rho_{2,3}) & (\varepsilon_2 - \varepsilon_3) \cdot \rho_{2,3} + t_{1,2} \cdot \rho_{1,3} + t_{2,3} \cdot (\rho_{3,3} - \rho_{2,2}) \\ (\varepsilon_3 - \varepsilon_2) \cdot \rho_{3,2} - t_{1,2} \cdot \rho_{3,1} + t_{2,3} \cdot (\rho_{2,2} - \rho_{3,3}) & t_{2,3} \cdot (\rho_{2,3} - \rho_{3,2}) \end{bmatrix}.$$

$$2)\ (\mathbb{M}_2)\ \mathcal{L}_{\text{inj}}[\rho] = \gamma_{\text{inj}}\left[\rho_{0,0}|1\rangle\langle 1| - \frac{1}{2}\left(\sum_{m=0}\rho_{0,m}|0\rangle\langle m| + \sum_{m=0}\rho_{m,0}|m\rangle\langle 0|\right)\right]. \tag{B.7}$$

$$\begin{aligned}
\mathbb{L}_{\text{inj}}[\rho]_{0,0} &= -\frac{1}{2}\gamma_{\text{inj}}\langle 0|\left(\sum_{m=0}\rho_{0,m}|0\rangle\langle m| + \sum_{m=0}\rho_{m,0}|m\rangle\langle 0|\right)|0\rangle, \quad m \neq m \\
&= -\frac{1}{2}\gamma_{\text{inj}}\langle 0|\left(\sum_{m=0}\delta_{m0}\rho_{0,m}|0\rangle + \sum_{m=0}\rho_{m,0}|m\rangle\right) \\
&= -\frac{1}{2}\gamma_{\text{inj}}\left(\sum_{m=0}\delta_{m0}\rho_{0,m} + \sum_{m=0}\delta_{m0}\rho_{m,0}\right) \\
&= -\frac{1}{2}\gamma_{\text{inj}}\left(2\rho_{0,0}\right).
\end{aligned}$$

$$\begin{aligned}
\mathbb{L}_{\text{inj}}[\rho]_{0,1} &= -\frac{1}{2}\gamma_{\text{inj}}\langle 0|\left(-2\rho_{0,0}|1\rangle\langle 1| + \sum_{m=0}\rho_{0,m}|0\rangle\langle m| + \sum_{m=0}\rho_{m,0}|m\rangle\langle 0|\right)|1\rangle, \quad m \neq m \\
&= -\frac{1}{2}\gamma_{\text{inj}}\langle 0|\left(-2\rho_{0,0}|1\rangle + \sum_{m=0}\delta_{m1}\rho_{0,m}|0\rangle\right) \\
&= -\frac{1}{2}\gamma_{\text{inj}}\left(\sum_{m=0}\delta_{m1}\rho_{0,m}\right) \\
&= -\frac{1}{2}\gamma_{\text{inj}}\ \rho_{0,1}.
\end{aligned}$$

$$\mathbb{L}_{\text{inj}}[\rho]_{0,2} = -\frac{1}{2}\gamma_{\text{inj}}\ \rho_{0,2}, \quad \mathbb{L}_{\text{inj}}[\rho]_{0,3} = -\frac{1}{2}\gamma_{\text{inj}}\ \rho_{0,3}.$$

$$\begin{aligned}
\mathbb{L}_{\text{inj}}[\rho]_{1,0} &= -\frac{1}{2}\gamma_{\text{inj}}\langle 1|\left(-2\rho_{0,0}|1\rangle\langle 1| + \sum_{m=0}\rho_{0,m}|0\rangle\langle m| + \sum_{m=0}\rho_{m,0}|m\rangle\langle 0|\right)|0\rangle, \quad m \neq m \\
&= -\frac{1}{2}\gamma_{\text{inj}}\langle 1|\left(\sum_{m=0}\delta_{m0}\rho_{0,m}|0\rangle + \sum_{m=0}\rho_{m,0}|m\rangle\right) \\
&= -\frac{1}{2}\gamma_{\text{inj}}\left(\sum_{m=0}\delta_{m1}\rho_{m,0}\right) \\
&= -\frac{1}{2}\gamma_{\text{inj}}\ \rho_{1,0}.
\end{aligned}$$

$$\begin{aligned}
\mathbb{L}_{\text{inj}}[\rho]_{1,1} &= -\frac{1}{2}\gamma_{\text{inj}}\langle 1|\left(-2\rho_{0,0}|1\rangle\langle 1| + \sum_{m=0}\rho_{0,m}|0\rangle\langle m| + \sum_{m=0}\rho_{m,0}|m\rangle\langle 0|\right)|1\rangle, \quad m \neq m \\
&= -\frac{1}{2}\gamma_{\text{inj}}\langle 1|\left(-2\rho_{0,0}|1\rangle + \sum_{m=0}\delta_{m1}\rho_{0,m}|0\rangle\right) \\
&= -\frac{1}{2}\gamma_{\text{inj}}\left(-2\rho_{0,0}\right).
\end{aligned}$$

$$\mathbb{L}_{\text{inj}}[\rho]_{1,2} = 0, \quad \mathbb{L}_{\text{inj}}[\rho]_{1,3} = 0.$$

$$\begin{aligned}
\mathbb{L}_{\text{inj}}[\rho]_{2,0} &= -\frac{1}{2}\gamma_{\text{inj}}\langle 2|\left(-2\rho_{0,0}|1\rangle\langle 1| + \sum_{m=0}\rho_{0,m}|0\rangle\langle m| + \sum_{m=0}\rho_{m,0}|m\rangle\langle 0|\right)|0\rangle, \quad m \neq m \\
&= -\frac{1}{2}\gamma_{\text{inj}}\langle 2|\left(\sum_{m=0}\delta_{m0}\rho_{0,m}|0\rangle + \sum_{m=0}\rho_{m,0}|m\rangle\right) \\
&= -\frac{1}{2}\gamma_{\text{inj}}\left(\sum_{m=0}\delta_{m2}\rho_{m,0}\right) \\
&= -\frac{1}{2}\gamma_{\text{inj}}\ \rho_{2,0}.
\end{aligned}$$

$$\begin{aligned}
\mathbb{L}_{\text{inj}}[\rho]_{2,1} &= -\frac{1}{2}\gamma_{\text{inj}}\langle 2|\left(-2\rho_{0,0}|1\rangle\langle 1| + \sum_{m=0}\rho_{0,m}|0\rangle\langle m| + \sum_{m=0}\rho_{m,0}|m\rangle\langle 0|\right)|1\rangle, \quad m \neq m \\
&= -\frac{1}{2}\gamma_{\text{inj}}\langle 2|\left(-2\rho_{0,0}|1\rangle + \sum_{m=0}\delta_{m1}\rho_{0,m}|0\rangle\right) \\
&= 0.
\end{aligned}$$

$$\mathbb{L}_{\text{inj}}[\rho]_{2,2} = 0, \quad \mathbb{L}_{\text{inj}}[\rho]_{2,3} = 0.$$

$$\begin{aligned}
\mathbb{L}_{\text{inj}}[\rho]_{3,0} &= -\frac{1}{2}\gamma_{\text{inj}}\langle 3|\left(-2\rho_{0,0}|1\rangle\langle 1| + \sum_{m=0}\rho_{0,m}|0\rangle\langle m| + \sum_{m=0}\rho_{m,0}|m\rangle\langle 0|\right)|0\rangle, \quad m \neq m \\
&= -\frac{1}{2}\gamma_{\text{inj}}\langle 3|\left(\sum_{m=0}\delta_{m0}\rho_{0,m}|0\rangle + \sum_{m=0}\rho_{m,0}|m\rangle\right) \\
&= -\frac{1}{2}\gamma_{\text{inj}}\left(\sum_{m=0}\delta_{m3}\rho_{m,0}\right) \\
&= -\frac{1}{2}\gamma_{\text{inj}}\ \rho_{3,0}.
\end{aligned}$$

$$\begin{aligned}
\mathbb{L}_{\text{inj}}[\rho]_{3,1} &= -\frac{1}{2}\gamma_{\text{inj}}\langle 3|\left(-2\rho_{0,0}|1\rangle\langle 1| + \sum_{m=0}\rho_{0,m}|0\rangle\langle m| + \sum_{m=0}\rho_{m,0}|m\rangle\langle 0|\right)|1\rangle, \quad m \neq m \\
&= -\frac{1}{2}\gamma_{\text{inj}}\langle 3|\left(-2\rho_{0,0}|1\rangle + \sum_{m=0}\delta_{m1}\rho_{0,m}|0\rangle\right) \\
&= 0.
\end{aligned}$$

$$\mathbb{L}_{\text{inj}}[\rho]_{3,2} = 0, \quad \mathbb{L}_{\text{inj}}[\rho]_{3,3} = 0.$$

$$\mathbb{M}_2 = -\frac{1}{2}\gamma_{\text{inj}}\begin{bmatrix} 2\rho_{0,0} & \rho_{0,1} & \rho_{0,2} & \rho_{0,3} \\ \rho_{1,0} & -2\rho_{0,0} & 0 & 0 \\ \rho_{2,0} & 0 & 0 & 0 \\ \rho_{3,0} & 0 & 0 & 0 \end{bmatrix}. \tag{B.8}$$

$$3)\ (\mathbb{M}_3)\ \mathcal{L}_{\text{ext}}[\rho] = \gamma_{\text{ext}} \left[\underbrace{\rho_{3,3}|0\rangle\langle 0|}_{1\to 0} - \underbrace{\frac{1}{2}\left(\sum_{m=0} \rho_{3,m}|3\rangle\langle m| + \sum_{m=0} \rho_{m,3}|m\rangle\langle 3| \right)}_{0\to 3} \right]. \tag{B.9}$$

$$\mathbb{M}_3 = -\frac{1}{2}\gamma_{\text{ext}} \begin{bmatrix} -2\rho_{3,3} & 0 & 0 & \rho_{0,3} \\ 0 & 0 & 0 & \rho_{1,3} \\ 0 & 0 & 0 & \rho_{2,3} \\ \rho_{3,0} & \rho_{3,1} & \rho_{3,2} & 2\rho_{3,3} \end{bmatrix}. \tag{B.10}$$

$$4)\ (\mathbb{M}_4)\ \mathcal{L}_{\text{deph}}[\rho] = \gamma_{\text{deph}} \sum_{i=0} \left[\rho_{i,i}|i\rangle\langle i| - \frac{1}{2}\left(\sum_{l=0} \rho_{i,l}|i\rangle\langle l| + \sum_{m=0} \rho_{m,i}|m\rangle\langle i| \right) \right]. \tag{B.11}$$

$$\begin{aligned}
\mathbb{L}_{\text{deph}}[\rho]_{0,0} &= \gamma_{\text{deph}} \sum_{i=0} \langle 0| \left[\rho_{i,i}|i\rangle\langle i| - \frac{1}{2}\left(\sum_{l=0} \rho_{i,l}|i\rangle\langle l| + \sum_{m=0} \rho_{m,i}|m\rangle\langle i| \right) \right] |0\rangle \\
&= \gamma_{\text{deph}} \sum_{i=0} \left[\rho_{i,i}\langle 0|i\rangle\langle i|0\rangle - \frac{1}{2}\left(\sum_{l=0} \rho_{i,l}\langle 0|i\rangle\langle l|0\rangle + \sum_{m=0} \rho_{m,i}\langle 0|m\rangle\langle i|0\rangle \right) \right] \\
&= \gamma_{\text{deph}} \sum_{i=0} \left[\rho_{i,i}\delta_{i0} - \frac{1}{2}\left(\sum_{l=0} \rho_{i,l}\delta_{i0}\delta_{l0} + \sum_{m=0} \rho_{m,i}\delta_{i0}\delta_{m0} \right) \right] \\
&= \gamma_{\text{deph}} \left[\rho_{0,0} - \frac{1}{2}\left(\sum_{l=0} \rho_{0,l}\delta_{l0} + \sum_{m=0} \rho_{m,0}\delta_{m0} \right) \right] \\
&= \gamma_{\text{deph}} \left[\rho_{0,0} - \frac{1}{2}\left(2\rho_{0,0} \right) \right] \\
&= 0.
\end{aligned}$$

$$\begin{aligned}
\mathbb{L}_{\text{deph}}[\rho]_{0,1} &= \gamma_{\text{deph}} \sum_{i=0} \langle 0| \left[\rho_{i,i}|i\rangle\langle i| - \frac{1}{2}\left(\sum_{l=0} \rho_{i,l}|i\rangle\langle l| + \sum_{m=0} \rho_{m,i}|m\rangle\langle i| \right) \right] |1\rangle \\
&= \gamma_{\text{deph}} \sum_{i=0} \left[\rho_{i,i}\langle 0|i\rangle\langle i|1\rangle - \frac{1}{2}\left(\sum_{l=0} \rho_{i,l}\langle 0|i\rangle\langle l|1\rangle + \sum_{m=0} \rho_{m,i}\langle 0|m\rangle\langle i|1\rangle \right) \right] \\
&= \gamma_{\text{deph}} \sum_{i=0} \left[\rho_{i,i}\delta_{i0}\delta_{i1} - \frac{1}{2}\left(\sum_{l=0} \rho_{i,l}\delta_{i0}\delta_{l1} + \sum_{m=0} \rho_{m,i}\delta_{m0}\delta_{i1} \right) \right] \\
&= \gamma_{\text{deph}} \left[-\frac{1}{2}\left(\sum_{l=0} \rho_{0,l}\delta_{l1} + \sum_{m=0} \rho_{m,1}\delta_{m0} \right) \right] \\
&= \frac{-1}{2}\gamma_{\text{deph}} \left(2\rho_{0,1} \right).
\end{aligned}$$

$$
\begin{aligned}
\mathbb{L}_{\text{deph}}[\rho]_{0,2} &= \gamma_{\text{deph}} \sum_{i=0} \langle 0| \left[\rho_{i,i} |i\rangle\langle i| - \frac{1}{2} \left(\sum_{l=0} \rho_{i,l} |i\rangle\langle l| + \sum_{m=0} \rho_{m,i} |m\rangle\langle i| \right) \right] |2\rangle \\
&= \gamma_{\text{deph}} \sum_{i=0} \left[\rho_{i,i} \langle 0|i\rangle\langle i|2\rangle - \frac{1}{2} \left(\sum_{l=0} \rho_{i,l} \langle 0|i\rangle\langle l|2\rangle + \sum_{m=0} \rho_{m,i} \langle 0|m\rangle\langle i|2\rangle \right) \right] \\
&= \gamma_{\text{deph}} \sum_{i=0} \left[\rho_{i,i} \delta_{i0}\delta_{i2} - \frac{1}{2} \left(\sum_{l=0} \rho_{i,l} \delta_{i0}\delta_{l2} + \sum_{m=0} \rho_{m,i} \delta_{m0}\delta_{i2} \right) \right] \\
&= \gamma_{\text{deph}} \left[-\frac{1}{2} \left(\sum_{l=0} \rho_{0,l} \delta_{l2} + \sum_{m=0} \rho_{m,2} \delta_{m0} \right) \right] \\
&= \frac{-1}{2} \gamma_{\text{deph}} \left(2\rho_{0,2} \right).
\end{aligned}
$$

$$
\begin{aligned}
\mathbb{L}_{\text{deph}}[\rho]_{0,3} &= \gamma_{\text{deph}} \sum_{i=0} \langle 0| \left[\rho_{i,i} |i\rangle\langle i| - \frac{1}{2} \left(\sum_{l=0} \rho_{i,l} |i\rangle\langle l| + \sum_{m=0} \rho_{m,i} |m\rangle\langle i| \right) \right] |3\rangle \\
&= \gamma_{\text{deph}} \sum_{i=0} \left[\rho_{i,i} \langle 0|i\rangle\langle i|3\rangle - \frac{1}{2} \left(\sum_{l=0} \rho_{i,l} \langle 0|i\rangle\langle l|3\rangle + \sum_{m=0} \rho_{m,i} \langle 0|m\rangle\langle i|3\rangle \right) \right] \\
&= \gamma_{\text{deph}} \sum_{i=0} \left[\rho_{i,i} \delta_{i0}\delta_{i3} - \frac{1}{2} \left(\sum_{l=0} \rho_{i,l} \delta_{i0}\delta_{l3} + \sum_{m=0} \rho_{m,i} \delta_{m0}\delta_{i3} \right) \right] \\
&= \gamma_{\text{deph}} \left[-\frac{1}{2} \left(\sum_{l=0} \rho_{0,l} \delta_{l3} + \sum_{m=0} \rho_{m,3} \delta_{m0} \right) \right] \\
&= \frac{-1}{2} \gamma_{\text{deph}} \left(2\rho_{0,3} \right).
\end{aligned}
$$

$$
\begin{aligned}
\mathbb{L}_{\text{deph}}[\rho]_{1,0} &= \gamma_{\text{deph}} \sum_{i=0} \langle 1| \left[\rho_{i,i} |i\rangle\langle i| - \frac{1}{2} \left(\sum_{l=0} \rho_{i,l} |i\rangle\langle l| + \sum_{m=0} \rho_{m,i} |m\rangle\langle i| \right) \right] |0\rangle \\
&= \gamma_{\text{deph}} \sum_{i=0} \left[\rho_{i,i} \langle 1|i\rangle\langle i|0\rangle - \frac{1}{2} \left(\sum_{l=0} \rho_{i,l} \langle 1|i\rangle\langle l|0\rangle + \sum_{m=0} \rho_{m,i} \langle 1|m\rangle\langle i|0\rangle \right) \right] \\
&= \gamma_{\text{deph}} \sum_{i=0} \left[\rho_{i,i} \delta_{i1}\delta_{i0} - \frac{1}{2} \left(\sum_{l=0} \rho_{i,l} \delta_{i1}\delta_{l0} + \sum_{m=0} \rho_{m,i} \delta_{i0}\delta_{m1} \right) \right] \\
&= \gamma_{\text{deph}} \left[-\frac{1}{2} \left(\sum_{l=0} \rho_{1,l} \delta_{l0} + \sum_{m=0} \rho_{m,0} \delta_{m1} \right) \right] \\
&= \gamma_{\text{deph}} \left[\rho_{0,0} - \frac{1}{2} \left(2\rho_{0,0} \right) \right] \\
&= \frac{-1}{2} \gamma_{\text{deph}} \left(2\rho_{1,0} \right).
\end{aligned}
$$

$$
\begin{aligned}
\mathbb{L}_{\text{deph}}[\rho]_{1,1} &= \gamma_{\text{deph}} \sum_{i=0} \langle 1| \left[\rho_{i,i} |i\rangle\langle i| - \frac{1}{2} \left(\sum_{l=0} \rho_{i,l} |i\rangle\langle l| + \sum_{m=0} \rho_{m,i} |m\rangle\langle i| \right) \right] |1\rangle \\
&= \gamma_{\text{deph}} \sum_{i=0} \left[\rho_{i,i} \langle 1|i\rangle\langle i|1\rangle - \frac{1}{2} \left(\sum_{l=0} \rho_{i,l} \langle 1|i\rangle\langle l|1\rangle + \sum_{m=0} \rho_{m,i} \langle 1|m\rangle\langle i|1\rangle \right) \right] \\
&= \gamma_{\text{deph}} \sum_{i=0} \left[\rho_{i,i} \delta_{i1} - \frac{1}{2} \left(\sum_{l=0} \rho_{i,l} \delta_{i1} \delta_{l1} + \sum_{m=0} \rho_{m,i} \delta_{m1} \delta_{i1} \right) \right] \\
&= \gamma_{\text{deph}} \left[\rho_{1,1} - \frac{1}{2} \left(\sum_{l=0} \rho_{1,l} \delta_{l1} + \sum_{m=0} \rho_{m,1} \delta_{m1} \right) \right] \\
&= \gamma_{\text{deph}} \left[\rho_{1,1} - \frac{1}{2} \left(2\rho_{1,1} \right) \right] \\
&= 0.
\end{aligned}
$$

$$
\mathbb{L}_{\text{deph}}[\rho]_{1,2} = \frac{-1}{2} \gamma_{\text{deph}} \left(2\rho_{1,2} \right), \quad \mathbb{L}_{\text{deph}}[\rho]_{1,3} = \frac{-1}{2} \gamma_{\text{deph}} \left(2\rho_{1,3} \right).
$$

$$
\mathbb{L}_{\text{deph}}[\rho]_{2,0} = \frac{-1}{2} \gamma_{\text{deph}} \left(2\rho_{2,0} \right), \quad \mathbb{L}_{\text{deph}}[\rho]_{2,1} = \frac{-1}{2} \gamma_{\text{deph}} \left(2\rho_{2,1} \right), \quad \mathbb{L}_{\text{deph}}[\rho]_{2,2} = 0.
$$

$$
\mathbb{L}_{\text{deph}}[\rho]_{2,3} = \frac{-1}{2} \gamma_{\text{deph}} \left(2\rho_{2,3} \right), \quad \mathbb{L}_{\text{deph}}[\rho]_{3,0} = \frac{-1}{2} \gamma_{\text{deph}} \left(2\rho_{3,0} \right), \quad \mathbb{L}_{\text{deph}}[\rho]_{3,1} = \frac{-1}{2} \gamma_{\text{deph}} \left(2\rho_{3,1} \right).
$$

$$
\mathbb{L}_{\text{deph}}[\rho]_{3,2} = \frac{-1}{2} \gamma_{\text{deph}} \left(2\rho_{3,2} \right), \quad \mathbb{L}_{\text{deph}}[\rho]_{3,3} = 0.
$$

$$
\mathbb{M}_4 = -\gamma_{\text{deph}} \begin{bmatrix} 0 & \rho_{0,1} & \rho_{0,2} & \rho_{0,3} \\ \rho_{1,0} & 0 & \rho_{1,2} & \rho_{1,3} \\ \rho_{2,0} & \rho_{2,1} & 0 & \rho_{2,3} \\ \rho_{3,0} & \rho_{3,1} & \rho_{3,2} & 0 \end{bmatrix}. \tag{B.12}
$$

Appendix C

Runge Kutta 4 in C++ to Solve Lindblad Quantum Master Equation for FMO-123

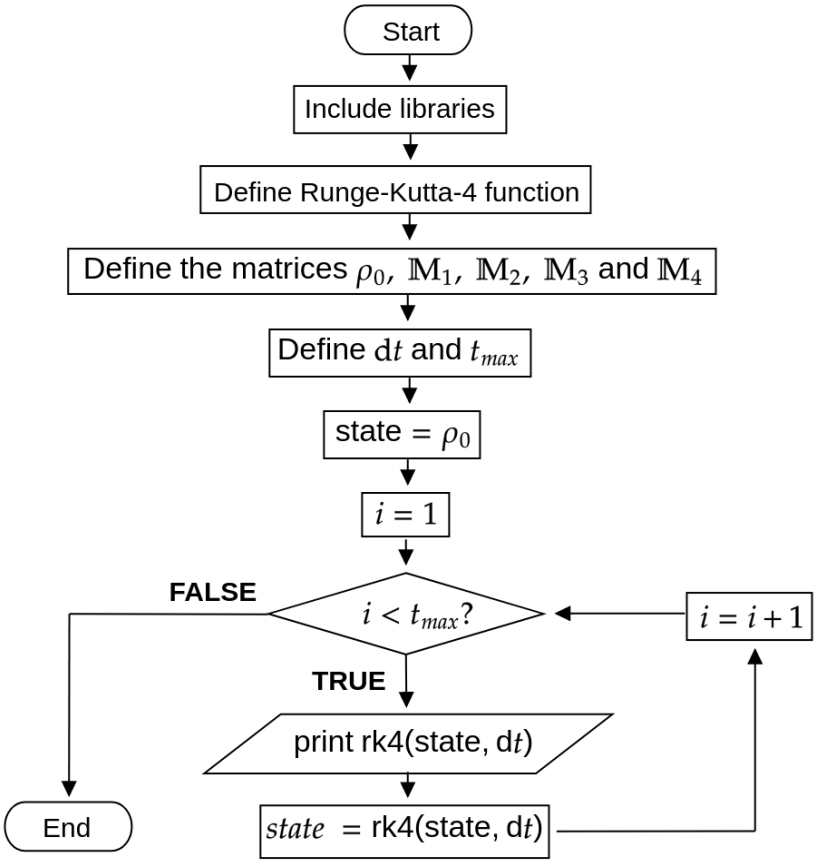

Figure C.1: Flowchart of the Runge-Kutta 4 numerical method implemented in C++ to solve the Lindblad quantum master equation for the reduced FMO complex *123*.

Appendix D

Graphs of the Populations of the Sites for FMO-123

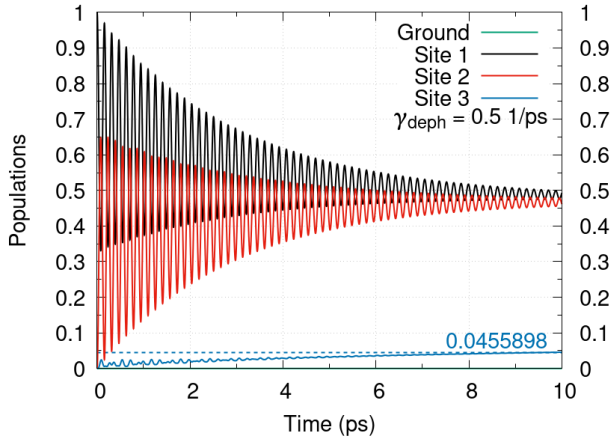

(a) The dephasing rate is $\gamma_{\text{deph}} = 0.5\ ps^{-1}$.

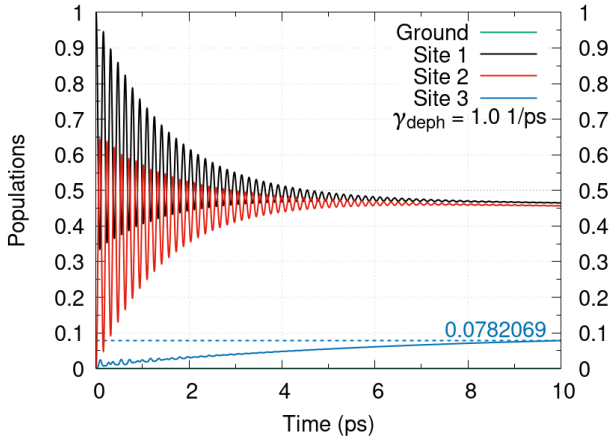

(b) The dephasing rate is $\gamma_{\text{deph}} = 1.0\ ps^{-1}$.

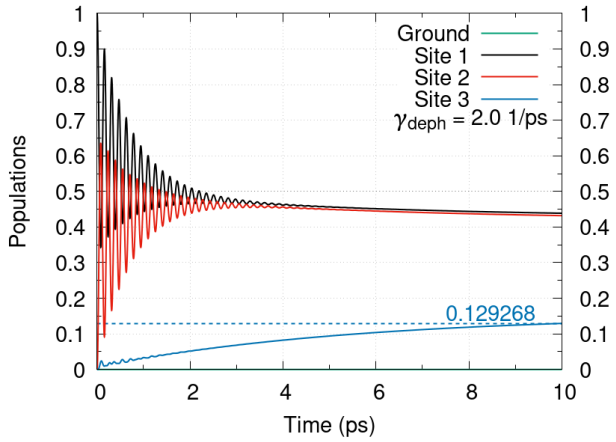

(c) The dephasing rate is $\gamma_{\text{deph}} = 2.0\ ps^{-1}$.

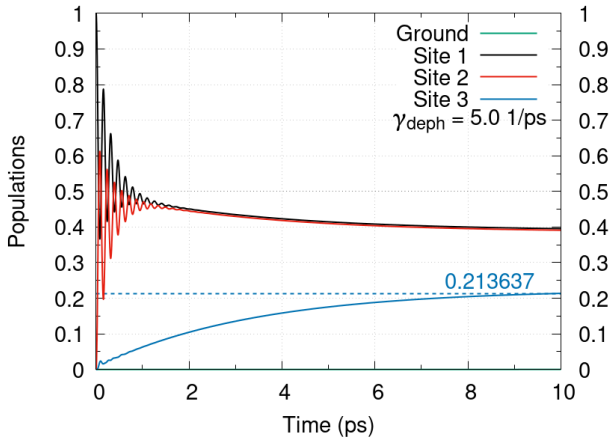

(d) The dephasing rate is $\gamma_{\text{deph}} = 5.0\ ps^{-1}$.

Figure D.1: Population in the reduced FMO complex *123* with (a) $\gamma_{\text{deph}} = 0.5\ ps^{-1}$, (b) $\gamma_{\text{deph}} = 1.0\ ps^{-1}$, (c) $\gamma_{\text{deph}} = 2.0\ ps^{-1}$, and (d) $\gamma_{\text{deph}} = 5.0\ ps^{-1}$. We set the parameters $\gamma_{\text{inj}} = 400\ \text{ps}^{-1}$ and $\gamma_{\text{ext}} = 0.1\ \text{ps}^{-1}$.

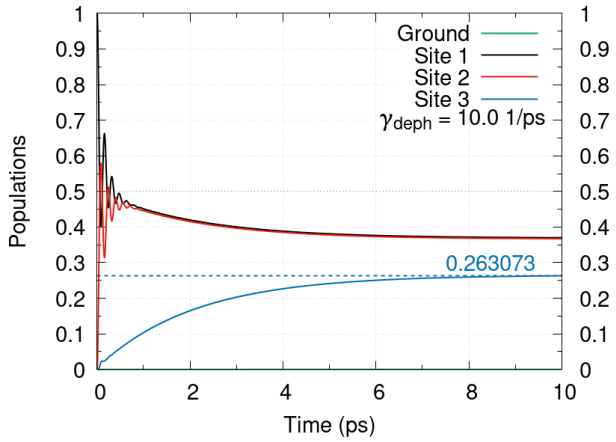

(a) The dephasing rate is $\gamma_{\text{deph}} = 10.0\ ps^{-1}$.

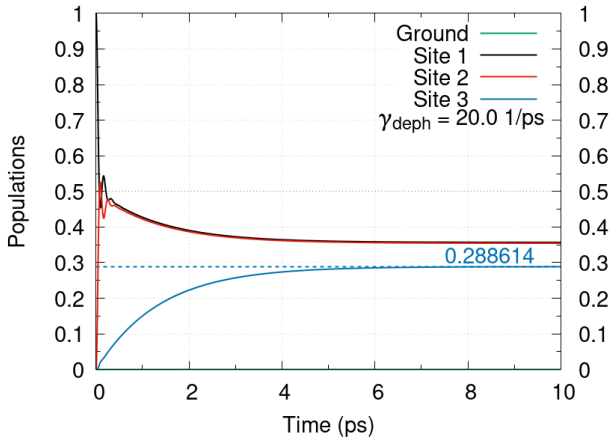

(b) The dephasing rate is $\gamma_{\text{deph}} = 20.0\ ps^{-1}$.

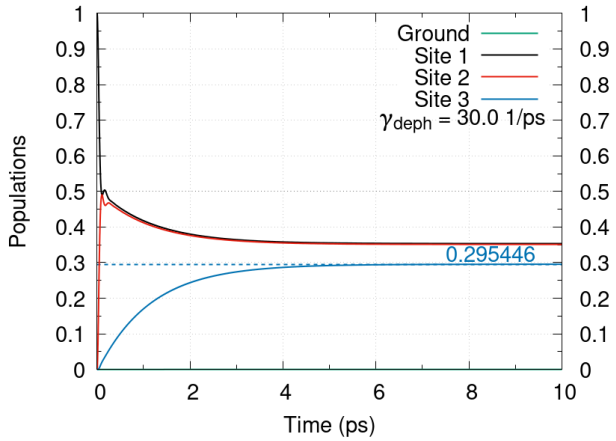

(c) The dephasing rate is $\gamma_{\text{deph}} = 30.0\ ps^{-1}$.

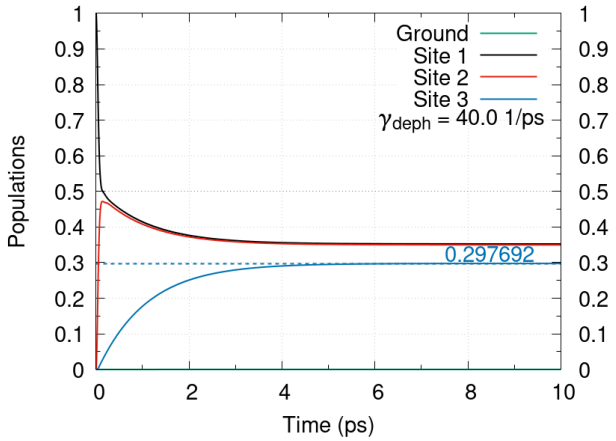

(d) The dephasing rate is $\gamma_{\text{deph}} = 40.0\ ps^{-1}$.

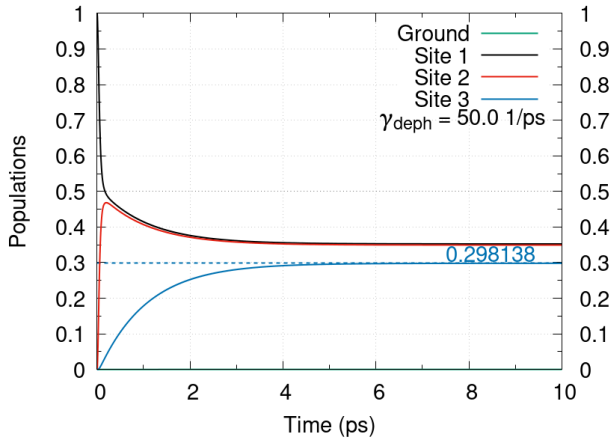

(e) The dephasing rate is $\gamma_{\text{deph}} = 50.0\ ps^{-1}$.

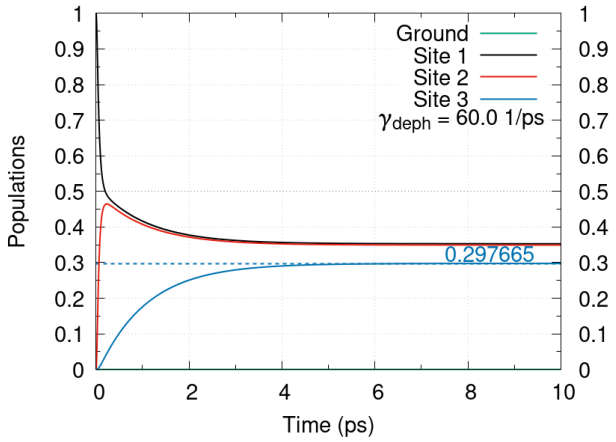

(f) The dephasing rate is $\gamma_{\text{deph}} = 60.0\ ps^{-1}$.

Figure D.2: Population in the reduced FMO complex *123* with (a) $\gamma_{\text{deph}} = 10.0\ ps^{-1}$, (b) $\gamma_{\text{deph}} = 20.0\ ps^{-1}$, (c) $\gamma_{\text{deph}} = 30.0\ ps^{-1}$, (d) $\gamma_{\text{deph}} = 40.0\ ps^{-1}$, (e) $\gamma_{\text{deph}} = 50.0\ ps^{-1}$, and (f) $\gamma_{\text{deph}} = 60.0\ ps^{-1}$. We set the parameters $\gamma_{\text{inj}} = 400\ \text{ps}^{-1}$ and $\gamma_{\text{ext}} = 0.1\ \text{ps}^{-1}$.

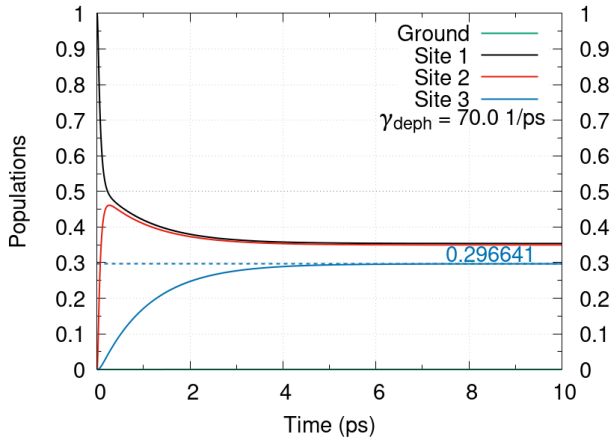

(a) The dephasing rate is $\gamma_{\text{deph}} = 70.0\ ps^{-1}$.

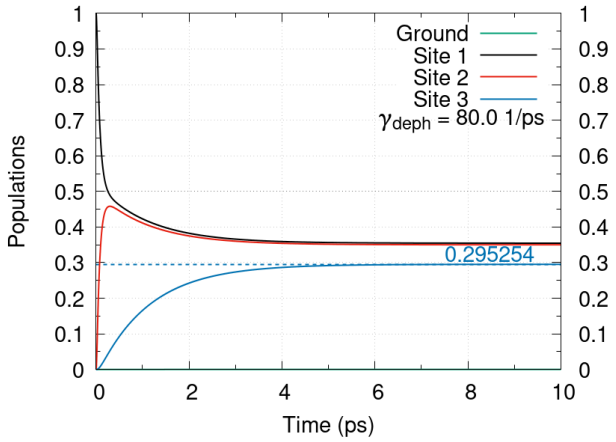

(b) The dephasing rate is $\gamma_{\text{deph}} = 80.0\ ps^{-1}$.

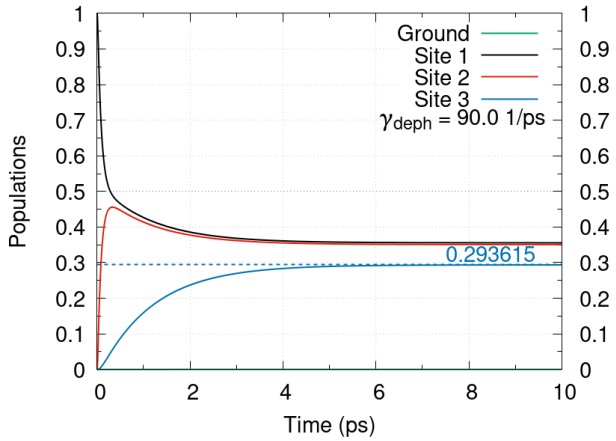

(c) The dephasing rate is $\gamma_{\text{deph}} = 90.0\ ps^{-1}$.

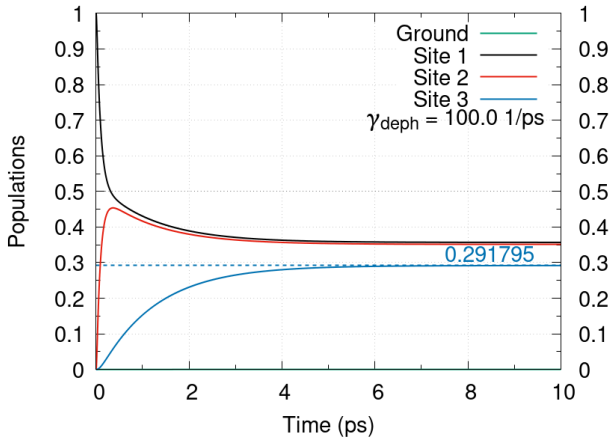

(d) The dephasing rate is $\gamma_{\text{deph}} = 100.0\ ps^{-1}$.

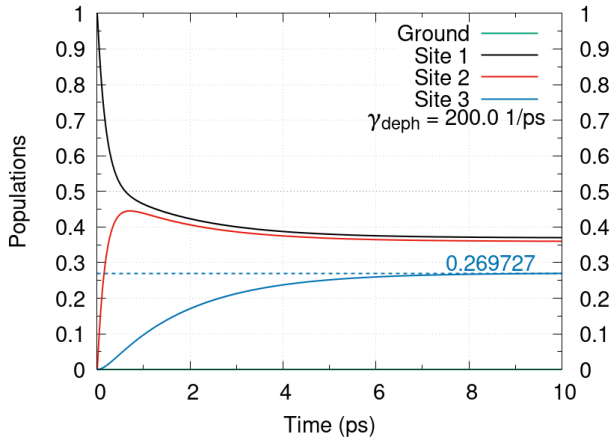

(e) The dephasing rate is $\gamma_{\text{deph}} = 200.0\ ps^{-1}$.

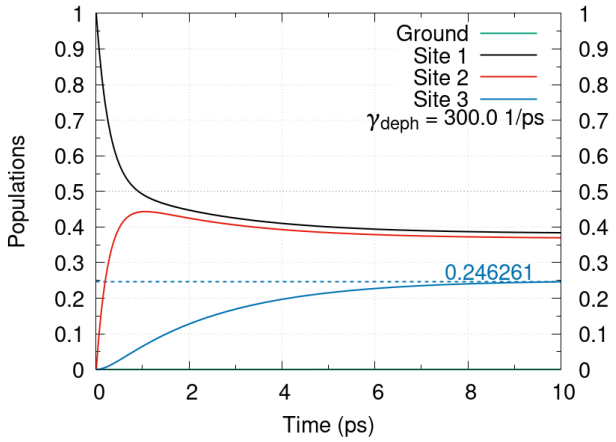

(f) The dephasing rate is $\gamma_{\text{deph}} = 300.0\ ps^{-1}$.

Figure D.3: Population in the reduced FMO complex *123* with (a) $\gamma_{\text{deph}} = 70.0\ ps^{-1}$, (b) $\gamma_{\text{deph}} = 80.0\ ps^{-1}$, (c) $\gamma_{\text{deph}} = 90.0\ ps^{-1}$, (d) $\gamma_{\text{deph}} = 100.0\ ps^{-1}$, (e) $\gamma_{\text{deph}} = 200.0\ ps^{-1}$, and (f) $\gamma_{\text{deph}} = 300.0\ ps^{-1}$. We set the parameters $\gamma_{\text{inj}} = 400\ \text{ps}^{-1}$ and $\gamma_{\text{ext}} = 0.1\ \text{ps}^{-1}$.

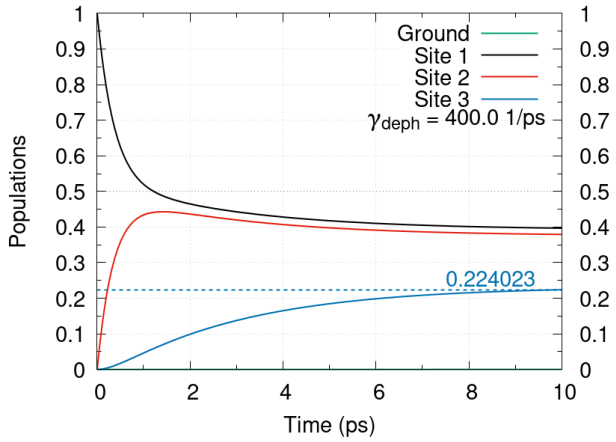

(a) The dephasing rate is $\gamma_{\text{deph}} = 400.0\ ps^{-1}$.

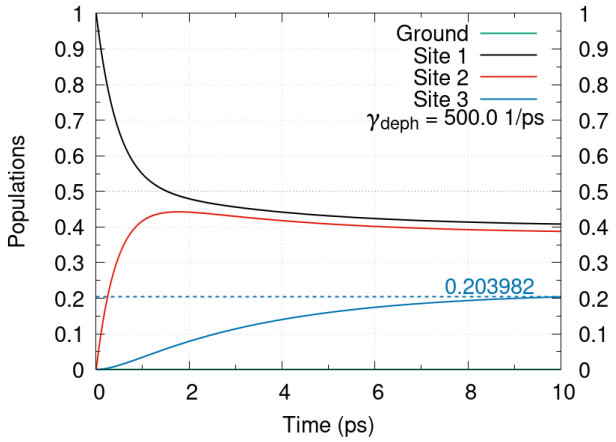

(b) The dephasing rate is $\gamma_{\text{deph}} = 500.0\ ps^{-1}$.

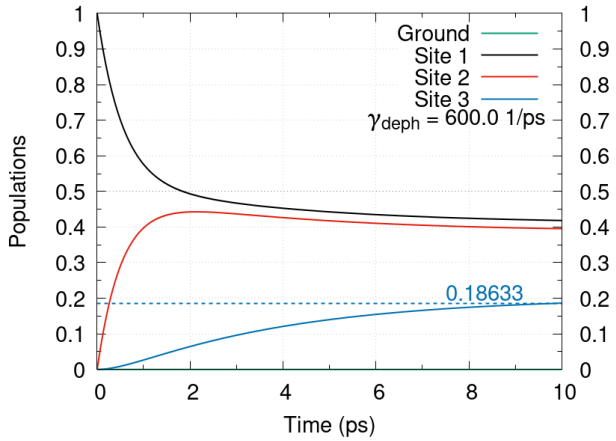

(c) The dephasing rate is $\gamma_{\text{deph}} = 600.0\ ps^{-1}$.

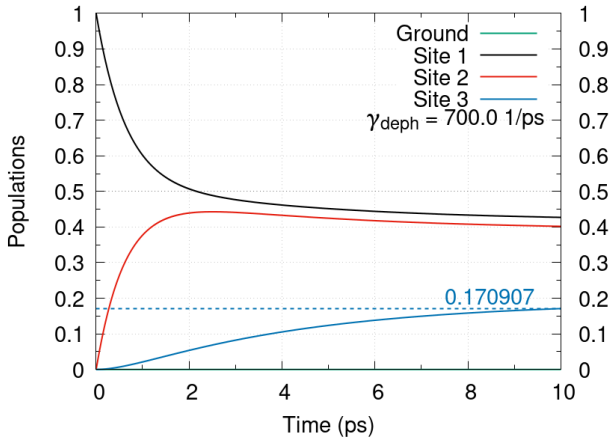

(d) The dephasing rate is $\gamma_{\text{deph}} = 700.0\ ps^{-1}$.

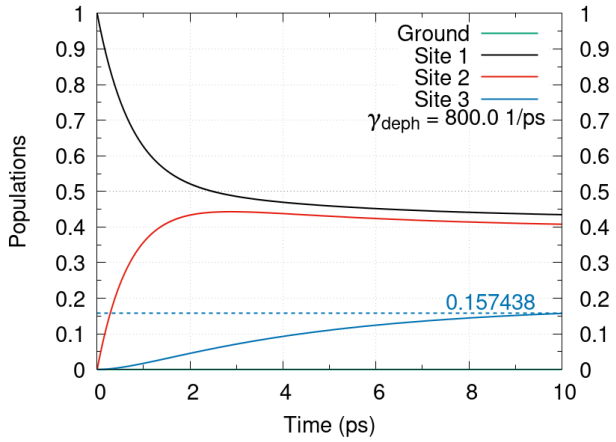

(e) The dephasing rate is $\gamma_{\text{deph}} = 800.0\ ps^{-1}$.

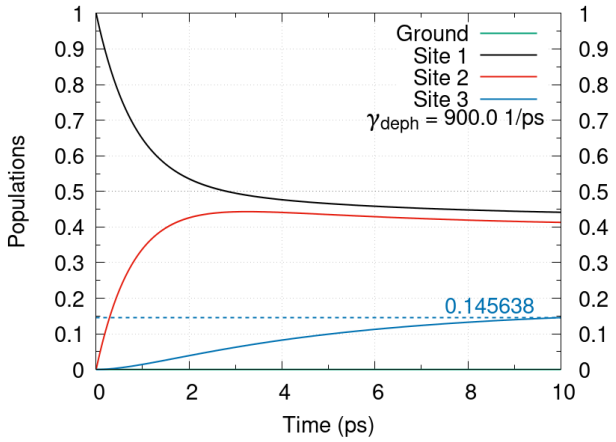

(f) The dephasing rate is $\gamma_{\text{deph}} = 900.0\ ps^{-1}$.

Figure D.4: Population in the reduced FMO complex *123* with (a) $\gamma_{\text{deph}} = 400.0\ ps^{-1}$, (b) $\gamma_{\text{deph}} = 500.0\ ps^{-1}$, (c) $\gamma_{\text{deph}} = 600.0\ ps^{-1}$, (d) $\gamma_{\text{deph}} = 700.0\ ps^{-1}$, (e) $\gamma_{\text{deph}} = 800.0\ ps^{-1}$, (f) $\gamma_{\text{deph}} = 900.0\ ps^{-1}$. We set the parameters $\gamma_{\text{inj}} = 400\ \text{ps}^{-1}$ and $\gamma_{\text{ext}} = 0.1\ \text{ps}^{-1}$.

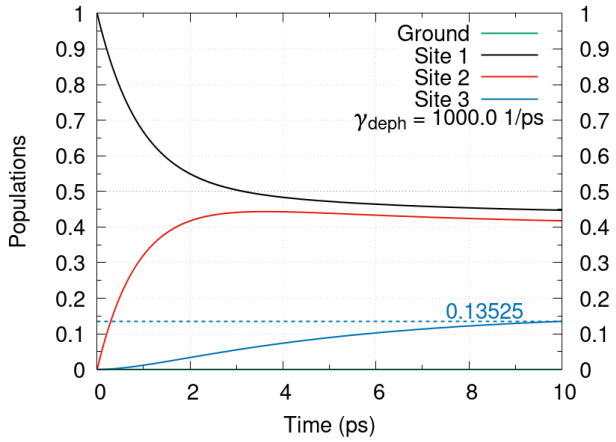

(a) The dephasing rate is $\gamma_{\text{deph}} = 1000.0\ ps^{-1}$.

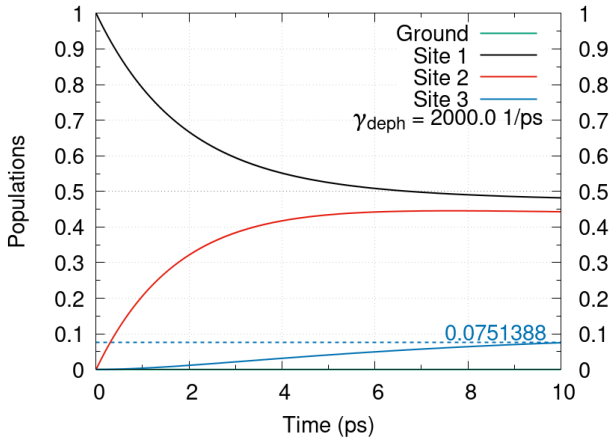

(b) The dephasing rate is $\gamma_{\text{deph}} = 2000.0\ ps^{-1}$.

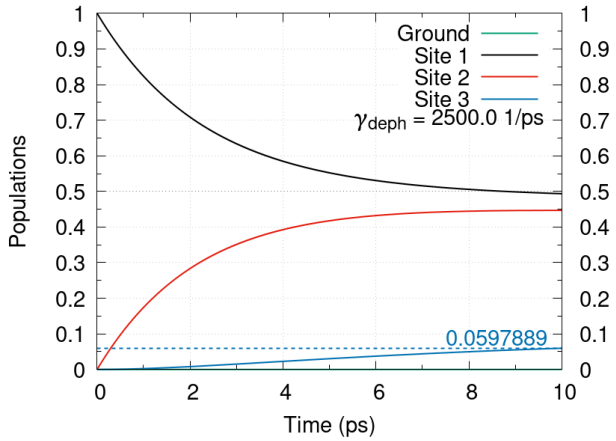

(c) The dephasing rate is $\gamma_{\text{deph}} = 2500.0\ ps^{-1}$.

Figure D.5: Population in the reduced FMO complex *123* with (a) $\gamma_{\text{deph}} = 1000.0\ ps^{-1}$, (b) $\gamma_{\text{deph}} = 2000.0\ ps^{-1}$, and (c) $\gamma_{\text{deph}} = 2500.0\ ps^{-1}$. We set the parameters $\gamma_{\text{inj}} = 400\ \text{ps}^{-1}$ and $\gamma_{\text{ext}} = 0.1\ \text{ps}^{-1}$.

Appendix E

Table Presenting Data of the Maximum Population in Site 3 for Every Dephasing Rate in FMO-123 with Lindblad Formalism.

$\gamma_{\mathbf{deph}}$ $(1/ps)$	**Maximum population in Site 3**
0.5	0.0455898
1.0	0.0782069
2.0	0.1292680
5.0	0.2136370
10.0	0.2630730
20.0	0.2886140
30.0	0.2954460
40.0	0.2976920
50.0	0.2981380
60.0	0.2976650
70.0	0.2966410
80.0	0.2952540
90.0	0.2936150
100.0	0.2917950
200.0	0.2697270
300.0	0.2462610
400.0	0.2240230
500.0	0.2039820
600.0	0.1863300
700.0	0.1709070
800.0	0.1574380
900.0	0.1456380
1000.0	0.1352500
2000.0	0.0751388
2500.0	0.0597889

Table E.1: Dephasing rate and the maximum population in site 3 in reduced FMO complex *123* with Lindblad formalism.

Appendix F

Implementation in Python to Solve the Retarded Green's Function for FMO-123

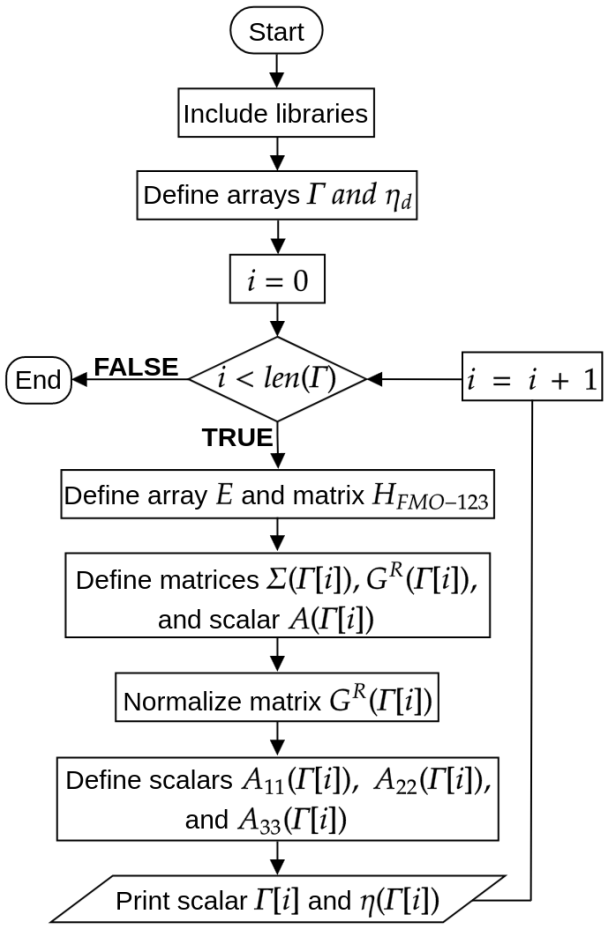

Figure F.1: Flowchart of the code implemented in Python to solve the Retarded Green's Function for the reduced FMO complex *123*.

Acronyms

ATP adenosine triphosphate. 1, 4, 81

BChl-a Bacteriochlorophyll a. 4, 14, 19, 81

DOS density of states. 42, 81

EET excitation energy transfer. 2, 6–8, 11–13, 81, 85

ENAQT environment-assisted quantum transport. ix, xi, 12–15, 29, 32, 34–36, 53, 54, 81

ETC exciton transfer complex. 4, 20, 81

FMO Fenna-Matthews Olso. ix, xi, xiii, 1–17, 19–28, 30, 32–34, 36–38, 40, 42, 44, 46, 48, 50, 54–56, 71, 73–77, 79, 81, 85–87

FMO-123 reduced FMO system. ix, xi, xiii, xiv, 10, 23, 25–33, 35, 36, 46, 47, 49–51, 53, 54, 59, 60, 62, 64, 66, 68, 71, 73, 74, 76, 79, 81, 85, 86

HEOM hierarchical equations of motion. 12, 81

LH2 light-harvesting 2. 2, 81

NEGF non-equilibrium Green's functions. 2, 37, 81

PC-645 cryptophyte protein phycocyanin 645. 2, 81

PPC pigment-protein complex. 4, 81

WBL wide-band limit. 45, 81

List of Figures

List of Tables

Bibliography

[1] J. W. Abbott. Quantum Dynamics of Bath Influenced Excitonic Energy Transfer in Photosynthetic Pigment-Protein Complexes. 2020.

[2] J. Adolphs and T. Renger. How proteins trigger excitation energy transfer in the FMO complex of green sulfur bacteria. *Biophysical Journal*, 91(8):2778–2797, oct 2006.

[3] M. Allegra, P. Giorda, and S. Lloyd. Global coherence of quantum evolutions based on decoherent histories: Theory and application to photosynthetic quantum energy transport. *Physical Review A*, 93:042312, 4 2016.

[4] L. A. Baker and S. Habershon. Robustness, efficiency, and optimality in the Fenna-Matthews-Olson photosynthetic pigment-protein complex. *The Journal of Chemical Physics*, 143(10):105101, sep 2015.

[5] K. Balzer and M. Bonitz. *Nonequilibrium Green's functions approach to inhomogeneous systems*. Springer, 2013.

[6] C. Bengtson. *Quantum Resources for Efficient Excitation Energy Transfer in Natural and Artificial Pigment-Protein Molecular Aggregates*. PhD thesis, Acta Universitatis Upsaliensis, 2018.

[7] R. E. Blankenship. *Molecular mechanisms of photosynthesis*. John Wiley & Sons, 2021.

[8] H. P. Breuer and F. Petruccione. The Theory of Open Quantum Systems. *The Theory of Open Quantum Systems*, 9780199213900:1–656, nov 2007.

[9] M. Cho, H. M. Vaswani, T. Brixner, J. Stenger, and G. R. Fleming. Exciton analysis in 2D electronic spectroscopy. *Journal of Physical Chemistry B*, 109(21):10542–10556, jun 2005.

[10] A. L. da Roz, M. Ferreira, F. de Lima Leite, and O. N. Oliveira. *Nanostructures*. 2017.

[11] Y. Dubi. Interplay between Dephasing and Geometry and Directed Heat Flow in Exciton Transfer Complexes. *Journal of Physical Chemistry C*, 119(45):25252–25259, oct 2015.

[12] G. S. Engel. Quantum coherence in photosynthesis. In *Procedia Chemistry*, volume 3, pages 222–231. Elsevier B.V., jan 2011.

[13] M. Esposito, M. A. Ochoa, and M. Galperin. Efficiency fluctuations in quantum thermoelectric devices. *Physical Review B - Condensed Matter and Materials Physics*, 91(11), mar 2015.

[14] M. Esposito, M. A. Ochoa, and M. Galperin. Quantum thermodynamics: A nonequilibrium green's function approach. *Physical Review Letters*, 114(8):080602, feb 2015.

[15] R. E. Fenna and B. W. Matthews. Chlorophyll arrangement in a bacteriochlorophyll protein from chlorobium limicola. *Nature*, 258(5536):573–577, dec 1975.

[16] O. Goldberg, Y. Meir, and Y. Dubi. Vibration-assisted and vibration-hampered excitonic quantum transport. *Journal of Physical Chemistry Letters*, 9:3143–3148, 6 2018. Number 38.

[17] B. González-Soria, F. Delgado, and A. Anaya-Morales. Parametric mapping of quantum regime in Fenna-Matthews-Olson light-harvesting complexes: A synthetic review of models, methods and approaches. *Applied Sciences (Switzerland)*, 10(18):6474, sep 2020.

[18] V. Gorini, A. Kossakowski, and E. C. Sudarshan. Completely positive dynamical semigroups of N-level systems. *Journal of Mathematical Physics*, 17(5):821–825, aug 1975.

[19] P. Gupta and C. M. Chandrashekar. Digital quantum simulation framework for energy transport in an open quantum system. jun 2020.

[20] E. Z. Harush and Y. Dubi. Do photosynthetic complexes use quantum coherence to increase their efficiency? Probably not. *Science Advances*, 7(8), feb 2021.

[21] H. Haug and A.-P. Jauho. *Quantum kinetics in transport and optics of semiconductors*. Springer, 2008.

[22] D. Hayes and G. S. Engel. Extracting the excitonic Hamiltonian of the Fenna-Matthews-Olson complex using three-dimensional third-order electronic spectroscopy. *Biophysical Journal*, 100(8):2043–2052, apr 2011.

[23] A. V. Herzog, T. E. Lipman, D. M. Kammen, and Others. Renewable energy sources. *Encyclopedia of life support systems (EOLSS). Forerunner Volume-'Perspectives and overview of life support systems and sustainable development*, 76, 2001.

[24] Z. Hu, K. Head-Marsden, D. A. Mazziotti, P. Narang, and S. Kais. A general quantum algorithm for open quantum dynamics demonstrated with the fenna-matthews-olson complex. *Quantum*, 6:726, 5 2022. Number 22.

[25] H. K. Hughes. The physical meaning of parseval's theorem. *American Journal of Physics*, 33:99–101, 2 1965.

[26] A. Ishizaki and G. R. Fleming. Quantum Coherence in Photosynthetic Light Harvesting. *Annual Review of Condensed Matter Physics*, 3(1):333–361, mar 2012.

[27] A. P. Jauho, N. S. Wingreen, and Y. Meir. Time-dependent transport in interacting and noninteracting resonant-tunneling systems. *Physical Review B*, 50:5528, 8 1994.

[28] B. Johansson. Security aspects of future renewable energy systems-A short overview. *Energy*, 61:598–605, nov 2013.

[29] L. P. Kadanoff and G. Baym. *Quantum statistical mechanics: Green's function methods in equilibrium and nonequilibrium problems*. CRC Press, 1 2018.

[30] I. G. Karafyllidis. Quantum transport in the FMO photosynthetic light-harvesting complex. *Journal of Biological Physics*, 43(2):239–245, jun 2017.

[31] L. Keldysh. Diagram technique for nonequilibrium processes. *Zh.Eksp.Teor.Fiz.*, 47:1515–1527, 1964.

[32] L. Ko, R. L. Cook, and K. B. Whaley. Dynamics of photosynthetic light harvesting systems interacting with N-photon Fock states. *The Journal of Chemical Physics*, 156(24):244108, jun 2022.

[33] R. Kubo, M. Toda, and N. Hashitsume. *Statistical Physics II Nonequilibrium Statistical Mechanics*. 1991.

[34] M. Kundu and C. M. Chandrashekar. Non-Markovianity between Site Pairs in FMO Complex Using Discrete-Time Quantum Jump Model. *ACS Omega*, 7(51):48067–48074, dec 2022.

[35] W. Y. Liang. Excitons. *Physics Education*, 5(4):226, jul 1970.

[36] G. Lindblad. On the generators of quantum dynamical semigroups. *Communications in Mathematical Physics*, 48(2):119–130, jun 1976.

[37] K. M. Harmatys, J. Chen, D. M. Charron, C. M. MacLaughlin, and G. Zheng. Deep-sea bacteria inspire researchers to develop new ways to see, treat tumours, 2018.

[38] G. D. Mahan. *Many-particle physics*. Plenum Press, 1990.

[39] D. Manzano. A short introduction to the Lindblad master equation. *AIP Advances*, 10(2):025106, feb 2020.

[40] T. E. Matsubara. A new approach to quantum-statistical mechanics. *Progress of Theoretical Physics*, 14:351–378, 10 1955.

[41] J. M. Olson, B. Ke, B. Matthews, A. Melkozernov, M. Miller, R. Pearlstein, J. Raymond, C. Romano, F. Roskosky, K. Sauer, B. Schoenborn, C. Sybesma, P. Thornber, W. Whitten, and G. Zubay. The FMO Protein. *Photosynthesis Research 2004 80:1*, 80(1):181–187, 2004.

[42] K. M. Pelzer, T. Can, S. K. Gray, D. K. Morr, and G. S. Engel. Coherent transport and energy flow patterns in photosynthesis under incoherent excitation. *Journal of Physical Chemistry B*, 118(10):2693–2702, mar 2014.

[43] P. Phillips. Advanced solid state physics. *Advanced Solid State Physics*, 3 2012.

[44] M. Qin, H. Z. Shen, X. L. Zhao, and X. X. Yi. Dynamics and quantumness of excitation energy transfer through a complex quantum network. *Physical Review E - Statistical, Nonlinear, and Soft Matter Physics*, 90:042140, 10 2014.

[45] P. Rebentrost and A. Aspuru-Guzik. Communication: Exciton-phonon information flow in the energy transfer process of photosynthetic complexes. *Journal of Chemical Physics*, 134:101103, 3 2011.

[46] P. Rebentrost, M. Mohseni, I. Kassal, S. Lloyd, and A. Aspuru-Guzik. Environment-assisted quantum transport. *New Journal of Physics*, 11(3):033003, mar 2009.

[47] P. Rebentrost, M. Mohseni, I. Kassal, S. Lloyd, and A. Aspuru-Guzik. Environment-assisted quantum transport. *New Journal of Physics*, 11(3):033003, mar 2009.

[48] N. Renaud, M. A. Ratner, and V. Mujica. A stochastic surrogate Hamiltonian approach of coherent and incoherent exciton transport in the Fenna-Matthews-Olson complex. *Journal of Chemical Physics*, 135(7):075102, aug 2011.

[49] A. Rivas and S. F. Huelga. *Open quantum systems*, volume 10. Springer, 2012.

[50] R. Rosenbach. *Numerical methods for complex quantum dynamics with applications to quantum biology and quantum many-body dynamics*. PhD thesis, Universität Ulm, 2016.

[51] D. Ryndyk. *Theory of Quantum Transport at Nanoscale*, volume 184. Springer International Publishing, 2016.

[52] S. Savikhin, D. R. Buck, W. S. Struve, S. Savikhin, D. R. Buck, and W. S. Struve. Oscillating anisotropies in a bacteriochlorophyll protein: Evidence for quantum beating between exciton levels. *CP*, 223:303–312, 11 1997.

[53] E. Schrödinger. What is life? Cambridge University Press, 1944.

[54] N. Skochdopole and D. A. Mazziotti. Functional subsystems and quantum redundancy in photosynthetic light harvesting. *Journal of Physical Chemistry Letters*, 2(23):2989–2993, dec 2011.

[55] G. Stefanucci and R. V. Leeuwen. *Nonequilibrium many-body theory of quantum systems: A modern introduction*, volume 9780521766173. Cambridge University Press, 1 2010.

[56] J. D. Vasquez Jaramillo, J. Fransson, and R. Lopez. Probing Magnetism at the Atomic Scale: Non-Equilibrium Statistical Mechanics Theoretical Treatise. 2018.

[57] C. J. Verzijl, J. S. Seldenthuis, and J. M. Thijssen. Applicability of the wide-band limit in dft-based molecular transport calculations. *Journal of Chemical Physics*, 138, 3 2013.

[58] S. I. Vulto, M. A. De Baat, R. J. Louwe, H. P. Permentier, T. Neef, M. Miller, H. Van Amerongen, and T. J. Aartsma. Exciton simulations of optical spectra of the FMO complex from the green sulfur bacterium Chlorobium tepidum at 6 K. *Journal of Physical Chemistry B*, 102(47):9577–9582, nov 1998.

[59] U. Weiss. Quantum dissipative systems, fourth edition. *Quantum Dissipative Systems, Fourth Edition*, pages 1–566, 1 2012.

[60] B. Witt and F. Mintert. Stationary quantum coherence and transport in disordered networks. *New Journal of Physics*, 15:093020, 9 2013.

[61] Yatendra S. Chaudhary. Photosynthesis to Solar Fuels: An Introduction. In *Solar Fuel Generation*, chapter 1, pages 1–18. CRC Press, 1 edition, 2017.

[62] E. Zerah-Harush and Y. Dubi. Universal Origin for Environment-Assisted Quantum Transport in Exciton Transfer Networks. *Journal of Physical Chemistry Letters*, 9(7):1689–1695, apr 2018.

[63] N. N. Zhang, M. J. Tao, W. T. He, X. Y. Chen, X. Y. Kong, F. G. Deng, N. Lambert, and Q. Ai. Efficient quantum simulation of open quantum dynamics at various Hamiltonians and spectral densities. *Frontiers of Physics*, 16(5):1–14, oct 2021.

[64] Z. Zhang and J. Wang. Origin of long-lived quantum coherence and excitation dynamics in pigment-protein complexes. *Scientific Reports 2016 6:1*, 6:1–9, 11 2016.